

CHIRPED REFRACTIVE MICROLENS ARRAYS

DISSERTATION

ZUR ERLANGUNG DES AKADEMISCHEN GRADES
DOKTORINGENIEUR (DR.-ING.)

vorgelegt der Fakultät für Maschinenbau
der Technischen Universität Ilmenau

von Dipl.-Ing. (FH) Frank Wippermann,
geboren am 27. August 1974 in Heilbad Heiligenstadt

1. Gutachter: Univ.-Prof. Dr. rer. nat. habil. Stefan Sinzinger
2. Gutachter: Prof. Dr. rer. nat. habil. Andreas Tünnermann
3. Gutachter: Priv. Doz. Dr. rer. nat. habil. Norbert Lindlein

Tag der Einreichung: 23.08.2007

Tag des Rigorosums: 21.11.2007

Tag der Verteidigung: 19.12.2007

Kurzfassung

Die vorliegende Arbeit befasst sich mit Aspekten des Designs, der Herstellung und der Charakterisierung nichtregulärer Mikrolinsenarrays, für die in Anlehnung an weitere nichtperiodische Strukturen der englischsprachige Begriff "chirped microlens array" (cMLA) eingeführt wurde. Im Gegensatz zu klassischen - regulären - Mikrolinsenarrays, die aus identischen Linsen mit konstantem Abstand zueinander gebildet werden, bestehen cMLAs aus ähnlichen, jedoch nicht identischen Linsen, die mittels parametrischer Beschreibung definiert sind. Die Zelldefinition kann durch analytische Funktionen, numerische Optimierungsverfahren oder eine Kombination aus beiden gewonnen werden. Bei allen gechirpten Arrays hängen die Funktionen von der Position der jeweiligen Zelle im Array ab.

Die Loslösung von der starren Geometrie regulärer Arrays führt zu einer Erweiterung des klassischen Arraybegriffes und ermöglicht neue Freiheitsgrade im Design mikrooptischer Systeme. Der Schwerpunkt der Arbeit ist auf das Aufzeigen der neuen Designmöglichkeiten gerichtet, welche anhand von prototypenhaft umgesetzten Beispielsystemen erläutert werden. Anwendungsgebiete sind hierbei unter anderem die Verbesserung der Integrationsmöglichkeiten und die Optimierung der Funktionsparameter optischer Systeme. Exemplarisch werden hierzu optische Designs und Prototypen diskutiert, die unter anderem Anwendungen in der Strahlformung und der miniaturisierten Abbildungsoptik besitzen. Letzteres betrifft ein ultra-dünnes Kamerasystem, welches auf einem Sehprinzip von Insekten basiert und Baulängen kleiner als $250\mu\text{m}$ ermöglicht. Hierbei findet ein cMLA Einsatz, welches die Korrektur außeraxialer Bildfehler und damit die Vergrößerung des Gesichtsfeldes der Kamera ermöglicht. Die das Array beschreibenden Funktionen können hierbei vollständig analytisch abgeleitet werden. Die Nutzung eines cMLA aus individuell angepassten Linsen ermöglicht damit erstmals, das bekannte Abbildungsprinzip von akademischen Prinzipprototypen zu Systemen mit optischen Parametern zu erweitern, die den Einsatzbedingungen industrieller Anwendungen genügen. Weiterhin wird ein Wabenkondensoraufbau auf Basis von cMLAs zur Strahlhomogenisierung behandelt. Im Gegensatz zu den zuvor aufgeführten Anwendungsbereichen von cMLAs steht hierbei die Interaktion der Gesamtheit aller Linsen des Arrays im Mittelpunkt, was im Besonderen zu neuartigen kohärenten Effekten führt. Die Nutzung nichtregulärer Arrays ermöglicht die Vermeidung der ansonsten auftretenden periodischen Intensitätsmaxima und -minima in der Homogenisierungsebene, was mit einer Verbesserung der Homogenität einhergeht. Wabenkondensoren auf Basis von cMLAs sind im Speziellen für Kurzpulsanwendungen in der Sensorik und Materialbearbeitung von Interesse, da andere homogenitätsverbessernde Maßnahmen nicht angewendet werden können.

Für die Herstellung der Arraystrukturen werden das Reflow von Fotolack und die Laserlithographie genutzt, die an die Besonderheiten der cMLAs anzupassen waren. Dies betrifft im Speziellen Softwaretools zur Erstellung von Maskendaten für den Reflowprozess und von profilbeschreibenden Daten für die Laserlithographie, die im Vorfeld der Prototypenfertigung entwickelt wurden und als universelle Werkzeuge zur Verfügung stehen.

Abstract

The presented thesis deals with the design, the fabrication, and the characterization of non-regular microlens arrays that are referred to as “chirped microlens array” (cMLA) in accordance to other non-periodical structures. In contrast to conventional, regular microlens arrays that consist of a repetitive arrangement of a unit cell on a fixed, equidistantly sectioned grid, a cMLA contains similar but not identical lenses that are defined by a parametric description. The parameters of each cell can be defined by analytical functions, by using numerical optimization techniques, or by a combination of the both. Dependency on the position of the cell within the array is the most characteristic property of these functions.

Overcoming the inflexibility of a regular arrangement leads to the enhancement of the classical array concept and enables new degrees of freedom in the design of micro-optical systems. The focus of this thesis is to point out the potentials of these new design possibilities which are explained by example systems built as prototypes. Fields of application are amongst others the improvement of the system’s integration and the optimization of the optical performance of a system. Applications in the field of beam shaping and miniaturized imaging optics are discussed in detail as example systems. The latter enables extremely thin imaging objectives with a track length shorter than $250\mu\text{m}$ that have their natural antetype in the compound eyes of insects. The use of a cMLA allows the correction of off-axis aberrations and consequently the extension of the field of view of the objective, whereas the array describing function can be derived analytically. For the first time, the use of a cMLA with individually adapted lenses allows the fabrication of objectives based on the well-known imaging principle that are compliant to the demands of industrial applications rather than just being proof-of-principle demonstrators.

Furthermore, a fly’s eye condenser setup based on cMLAs is discussed. In contrast to the application examples mentioned before, here the focus is on the collective interaction of all lenses of the array that leads to novel coherent effects. The periodic intensity peaks appearing in the plane of homogenization which are typical when using regular arrays can be avoided by employing non-periodic arrays. This leads to an improved homogeneity of the radiation. Fly’s eye condensers based on cMLAs are especially advantageous when dealing with short pulse applications such as in sensing or material processing since otherwise applicable homogeneity improving measures are not suitable.

The microlens arrays are fabricated using reflow of photoresist or laser lithography which had to be adapted to the specifics of cMLAs. This concerns especially software tools for the generation of mask layouts for the reflow of photoresist as well as profile data for laser lithography which had to be developed beforehand the prototyping and are now available as universal tools.

Contents

1	Introduction	1
2	Motivation	4
2.1	Applications of microlens arrays	4
2.2	Artificial apposition compound eye camera	5
2.3	Hybrid imaging	8
2.4	Fly’s eye condenser systems	11
3	Fundamentals of chirped microlens arrays	16
3.1	Definition	16
3.2	Classification	17
3.3	Derivation of cell parameters	19
3.4	Fabrication methods	20
3.4.1	Reflow of photoresist specific to cMLA	20
3.4.2	Direct writing techniques specific to cMLA	25
4	Individual channel design	30
4.1	cMLA for improved system integration	30
4.1.1	Selection of best suited channel	30
4.1.2	Reduction of number of components	33
4.2	cMLA for optimization of optical performance	40
4.2.1	cMLA of ellipsoidal microlenses	40
4.2.2	cMLA of off-axis lens segments	56
5	Collective channel design	67
5.1	Design considerations	67
5.2	Evaluation of homogenization	69
5.3	Numerical simulation	71
5.4	Fly’s eye condenser with planar substrates	72
5.4.1	Simulation results	73
5.4.2	Practical considerations	78
5.4.3	Experimental results	80
5.5	Fly’s eye condensers with non-planar substrates	81
6	Conclusions and outlook	86
	References	89

A Symbols and abbreviations	100
B Acknowledgements	104
C Erklärung	105
D Thesen	106
E Lebenslauf	108
F Wissenschaftliche Veröffentlichungen	109

1 Introduction

Micro-lens arrays are one of the most prominent categories of elements in today's micro-optical systems. The fields of application of micro-lens arrays (MLAs) are widespread and it is almost impossible to provide a comprehensive listing. They can be found in imaging, beam shaping and coupling applications with uncounted diversity.¹ Starting from scientific applications they made their way to consumer products with millions of them produced every day especially in the fields of imaging and illumination.

According to the definition of the International Standards Organization (ISO) the term "micro-lens array" describes a "regular arrangement of micro-lenses on a single substrate" whereas a micro-lens is a "lens with an aperture of less than a few millimeters".² When talking about micro-lens arrays so far, a repetitive arrangement of a unit cell on a fixed, equidistantly sectioned grid was meant. This static arrangement is disadvantageous for many applications because the cells cannot be optimized individually for their specific optical function but instead the design is a compromise which enables a sufficient overall performance. By using a MLA where each lens is individually adapted to its optical task, a new degree of freedom in the system's design can be achieved that leads to micro-optical systems with improved optical performance or further upgrades compared to regular arrays. The phrase "chirped micro-lens array" (cMLA) was introduced for this kind of arrays with channel-wise designed cells and was inspired by other non-periodical optical terms like chirped gratings or pulses.³ It is the ambition of this thesis to give a first insight into the possibilities this type of optical elements offers and into the existing limits.

Therefore, in Chap. 2 a more detailed listing of state-of-the-art regular micro-lens array (rMLA) applications is given. Further on, examples of micro-optical systems using MLAs are explained in-depth, the basics of their optical design are presented and the limitations caused by the use of rMLAs are pointed out. Adapted cMLAs will be implemented in these example systems in the following sections and it will be explained how the limitation can be overcome and the system performance and integration can be improved.

Besides the conventional, regular micro-lens arrays, stochastic arrays are well known for a long time which are predominantly used in illumination applications.⁴ These consist of lenses with randomly chosen parameters like focal length or position in the array. In contrast, cMLAs consist of lenses with parameters which can be described by functions depending on the position of the individual lens within the array. For a better distinction of the concept of cMLAs with respect to other array setups, a precise definition is given in Chap. 3 which deals with fundamental aspects of cMLAs. A classification scheme is proposed which accounts for the design of the arrays. Two main categories can be distinguished which differ in their design approaches and in the optical effects taken into account. In the first type, each channel can be designed individually without influencing the performance or the layout of the other lenses of the array except for geometrical reasons. Special fields of application can be assigned to this category that deal with the improvement of the system's integration and the optimization of

the optical performance. The second class is dedicated to the collective channel design where the interaction of all channels of the array has to be considered in the layout. Coherent effects are especially important in this type of array applications.

A parametric description of the shape of the individual lenses and finally of the entire array is the ultimate goal of the design process independent of the specific approach used. Three different ways can be distinguished in the effort necessary to derive the describing functions and the calculation time needed for each single lenslet. Advantages and disadvantages of the different approaches are discussed. One of the most crucial aspects in the application of MLAs are the limitations of the fabrication technologies that have to be considered during the entire design process. A variety of different techniques have been developed over the last decades. In this thesis the considerations are limited to refractive microlenses where reflow of photoresist and laser lithography have gained most scientific and industrial relevance as fabrication technique besides single point diamond turning.⁵ The reflow technology is based on a lithographic mask process. In order to generate the individual shape of the lenses of the cMLA, a mask with channel-wise adapted structures has to be produced. State-of-the-art software tools for the mask generation are optimized for the generation of periodically repeating structures only. Therefore, software tools were developed to transfer the lens data of the cMLA to the commercial mask generation tools in an universal and user-friendly manner. Further on, a two-step lithographic process was used in order to enhance the possibilities of the array design. A film of photoresist is exposed through a lithographic mask in the standard reflow process. The base area of the lens and the thickness of the photoresist define the volume to be melted which finally determines the shape of the lens. The constant thickness of the resist over the entire array is disadvantageous since it limits the design possibilities. In the two-step process, the bases of the lenses are defined using a first lithographic mask. Then the photoresist is spin-coated and subsequently patterned through a second mask which defines the volume to be melted. Consequently, the footprint and the volume of the lens can be controlled independently and the design possibilities of cMLAs fabricated by the reflow process can be enhanced. For a further improvement of the design flexibility, laser lithography was used in order to overcome the limitations inherent to the reflow process. The possibility to generate non-spherical lens elements is a special advantage of this technology. Software tools were developed to translate the lens design values of the cMLA into the data controlling of the laser exposure machine. The two adapted fabrication methods were used for the manufacture of all cMLAs employed in the following application examples. Further on, 2-photon polymerization is introduced as another possible fabrication technique for cMLAs and first prototyped micro-optical structures are presented.

The main part of this thesis is dedicated to application examples of cMLAs confirming their advantages in the design of micro-optical systems. The proposed adapted fabrication technologies and strategies for obtaining the parametric lens definitions were used for their realization. In Chap. 4 different example systems based on the individual channel design approach are discussed in detail. First, the use of cMLAs for the improvement of the integration of micro-

optical systems is shown by the example of a laser beam shaping system. Further on, two examples of the use of a cMLA for the optimization of the optical performance are presented where the arrays are used for aberration compensation. In the first example, an adapted cMLA is used to improve the resolution of an artificial apposition compound eye objective which is inspired by the vision system of insects such as the house fly.⁶ By using an array of individually adapted lenses the field of view of the objective can be improved significantly. For the first time, prototypes of the well-known imaging principle have been fabricated which are compliant to the demands of industrial applications rather than just being proof-of-principle demonstrators. The functions defining the parameters of the array can be derived analytically and reflow of photoresist is used as fabrication technique. A prototype system of a planar integrated free-space optical interconnect is discussed as second example of the compensation of aberrations by a cMLA. Here, laser lithography is employed as fabrication technique for the array of individually adapted off-axis lens segments whose describing parameters have been calculated using the combined approach based on numerical optimization and analytical functions.

A novel design of a fly's eye condenser setup using cMLAs is discussed in Chap. 5 as an example of the category of collective channel design approaches. These systems are used to shape an almost arbitrary input intensity distribution into a top hat. Conventional systems that are based on rMLAs and a Fourier lens possess a limited homogeneity of the intensity distribution in the focal plane of the Fourier lens. Equidistant intensity peaks appear which are caused by the repeating structure of the rMLA and are due to grating interference effects. By applying the concept of chirped and therefore non-periodic arrays, the equidistant and sharp intensity peaks can be suppressed and the homogeneity of the intensity distribution can be improved. Reflow of photoresist is used as fabrication technique which constricts the possible array designs. New coherent effects can be studied at these systems and rules can be derived for the design of fly's eye condensers with improved homogeneity. The novel concept of fly's eye condensers based on cMLAs is especially advantageous when dealing with short pulse applications such as in sensing or material processing since otherwise applicable homogeneity improving measures are not suitable.

Finally, in Chap. 6 the results of the presented work are summarized and conclusions are drawn. Ideas for further activities on this research topic are itemized as an outlook.

2 Motivation

The significance of MLAs as key components in many micro-optical systems is explained in this section by a brief outline of the evolution and the current state-of-the-art of MLA applications. In addition, specific example systems based on regular arrays are discussed in detail in order to explain their optical design and to point out limitations caused by the periodical construction of the arrays. It will be shown in the upcoming sections how adapted cMLAs can be utilized to improve the performance or simplify the overall system design.

2.1 Applications of microlens arrays

The fields of application of MLAs are widespread, and it is out of the scope of this work to provide a comprehensive listing. However, a broad division to imaging, beam shaping, and coupling can be observed.¹ The first group includes e.g. integral photography as the first promoted application of arrays of lenses ever proposed by Lippmann.⁷⁻⁹ Multi aperture imaging optics like apposition compound eyes,^{6,10-12} cluster eyes,¹³⁻¹⁶ mask projection lithography,^{17,18} and copy machines¹⁹ are further prominent representatives of this field. Additionally, Gabor superlenses consisting of two MLAs of different lens pitch can be used to build objectives of low resolution but with a f-number possibly smaller than unity.^{20,21} New approaches like lightfield photography use MLAs to increase the depth of field of digital cameras.²² Another new field of application is the fabrication of miniaturized single aperture imaging optics as used in mobile phone digital cameras on wafer level.²³ Here, classical cameras are produced by stacking optical and opto-electronic wafers in order to build a huge number of systems in parallel that leads to reduced fabrication costs.

The most prominent application of MLAs in beam shaping are fly's eye condensers used for beam homogenization or the generation of arrays of equidistant intensity peaks referred to as array illuminators.²⁴⁻²⁸ These were first employed in microscopy illumination²⁹ and are now widely used for the beam shaping of almost any kind of laser radiation into a top hat intensity distribution.³⁰ In addition, array illumination generators used as fan-out elements can be ranked among this group.^{26,27}

Finally, MLAs are used for coupling or collimation of laser radiation in fiber optical and waveguide devices such as switches,^{31,32} interconnects,^{33,34} or VCSEL arrays.³⁵ Nowadays, MLAs for the enhancement of the fill factor of CCD- and CMOS-imagers are ubiquitous in digital photography and can also be related to this group.^{36,37}

However, there are numerous important collateral applications which do not fit in the proposed categorization scheme such as beam steering systems,³⁸⁻⁴⁰ Shack-Hartman-Wavefront sensors,^{41,42} or solar cells with Fresnel lenses for the enhancement of the optical effectiveness.⁴³ The growth of the fields of applications of MLA is connected to the evolution of the required fabrication techniques. In early systems, single lenses had to be processed and assembled into arrays. This additional assembly step is cost-intensive and especially challenging or

even unsuited if tight position tolerances had to be observed.^{44–46} Nowadays, most techniques use lithographic steps in order to cope with the tight tolerances.^{1,28,47,48} Additionally, single point diamond turning is widely used, especially if arrays of aspherical lenses are required as in imaging optics.^{47,49,50}

2.2 Artificial apposition compound eye camera

Artificial apposition compound eye cameras have their natural antetype in the compound eyes of many insects such as the house fly.⁶ They are an attractive approach for a vast reduction of the system length (less than $250\mu\text{m}$) of imaging optical systems with low required spatial resolution.^{51,52} They consist of an array of microlenses each having an associated photo receptor (Fig. 2.1a). In nature, the microlens layer as well as the light sensitive cells are both arranged on a curved basis. Each optical channel (known as “ommatidium”) focuses the light coming from the object points on the channel’s optical axis and its closer surrounding which is determined by the acceptance angle $\Delta\varphi$ of the channel. This angle depends on the focal length f of the microlens, the diameter d of the photo receptor, and the intensity distribution $PSF(x)$ in the focal plane of the microlens and can be calculated by

$$\Delta\varphi = \frac{FWHM [\text{rect}(\frac{x}{d}) \otimes PSF(x)]}{f}, \quad (2.1)$$

where FWHM stands for the full width at half maximum and \otimes for the mathematical operation of convolution. The minimum extension of the intensity distribution is given in the absence of any aberration and is determined by diffraction effects at the aperture of the lens. The intensity distribution in the focal plane of a lens free of aberrations equals the well-known Airy distribution.⁵³ Commonly, the diameter of the spot is defined as the distance between the first zeros of the distribution and can be calculated by

$$d_{Airy} = \frac{1.22\lambda}{n \sin \gamma}, \quad (2.2)$$

with λ as the wavelength of the radiation, n the index of refraction of the material in the image space behind the lens and γ the cone angle of the focused bundle. Each channel transmits only a small part of the complete field of view with a FWHM width of about 1° for both, natural and state-of-the-art artificial apposition compound eyes.^{6,16} Due to the bending, each ommatidium points in a different angular direction. Therefore, these compound eyes exhibit a very large field of view (FOV) while the single channels are working on-axis not suffering from off-axis aberrations. Contrary to curved bases in nature, in artificial systems the photo receptors (pixels of an imager) as well as the lenses must be arranged on flat substrates since today’s imager fabrication technologies like CCD or CMOS are based on planar lithography. In order to achieve a large FOV, the optical axes of the channels determined by the lens vertex and the center of the photo receptor must radiate outwards (Fig. 2.1b). This can

be accomplished by a small difference between the pitch of the lenses p_{lens} and the pitch of the receptors $p_{pinhole}$ (possibly covered by a pinhole to adjust the diameter of the light sensitive zone). Since each channel of the artificial compound eye objective is assigned to another angular direction in space with a difference in chief ray angle of adjacent channels of $\Delta\Phi$, the difference of the center positions of the lenses and receptors varies from cell to cell. Consequently, the microlenses are used under oblique incidence inherently connected with off-axis aberrations like astigmatism, field curvature, coma, and distortion.^{53,54} The resolution of an apposition compound eye is characterized by the number of resolvable line pairs γ_{LP} over the entire field of view ϕ_{FOV} and is given by⁵⁵

$$\gamma_{LP} = \frac{\phi_{FOV}}{\Delta\varphi}. \quad (2.3)$$

Thus, in the presence of aberrations the resolution of the apposition compound eye drops due to a widened intensity distribution $PSF(x)$ and an increased acceptance angle according to Eq. (2.3). Therefore, the FOV of the camera is limited by off-axis aberrations to about 25° when using spherical lenses with a f-number of about 2.3 that allow diffraction limited spots under perpendicular incidence. When using lenses with a small numerical aperture, astigma-

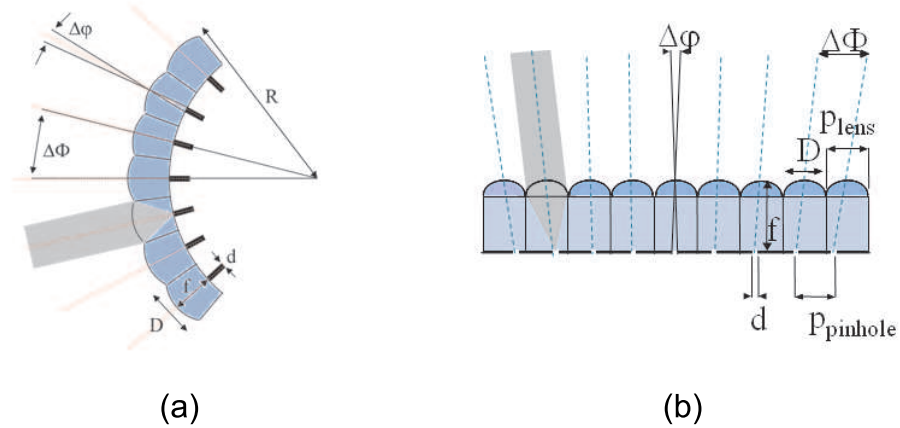


Figure 2.1: Schematic drawings of (a) a natural apposition eye with ommatidia arranged on curved surfaces and (b) an artificial apposition eye objective with photo receptors as well as microlenses arranged on a flat substrate. R - radius of curvature of natural apposition eye, D - aperture diameter of single channel, d - diameter of photo receptor, $\Delta\varphi$ - acceptance angle of single channel, $\Delta\Phi$ - angular separation of adjacent channels = interommatidial angle, f - focal length of single lens, p_{lens} - pitch of lenses, $p_{pinhole}$ - pitch of photo receptors.

tism and field curvature are by far dominant compared to coma which is of minor influence on the widening of the point spread function (Fig. 2.2). Astigmatism is a consequence of the different optical powers of a spherical lens in the tangential and the sagittal plane. It occurs for chief ray angles σ different from zero. The tangential plane is spanned by the chief ray of the considered field and the optical axis, whereas the sagittal plane contains the chief ray and is perpendicular to the tangential plane. Due to the varying optical powers, different back

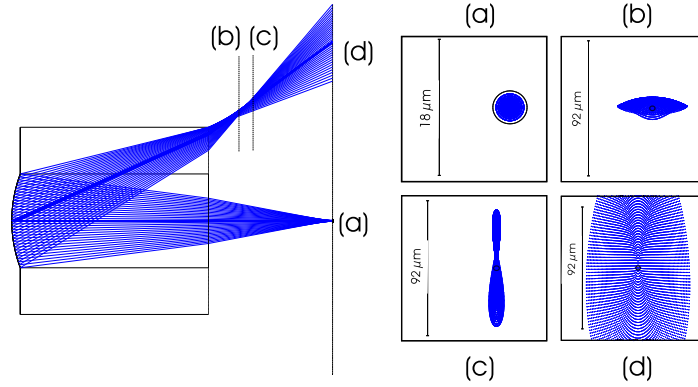


Figure 2.2: Spherical lens under perpendicular and oblique incidence and related spot diagrams with radius of curvature $R=339\mu m$ and diameter $D=242.8\mu m$ in fused silica. (a) A diffraction limited focus (geometrical spot size smaller than Airy-disk diameter indicated by black circle) is achieved under perpendicular incidence. When illuminating the lens under oblique incidence astigmatism leads to a (b) tangential and (c) sagittal line focus with perpendicular orientation. (d) Astigmatism and field curvature lead to a large spot in the Gaussian image plane. The tangential and sagittal image planes are separated from the Gaussian image plane (here $-165\mu m$ and $-262\mu m$, respectively).

focal lengths (BFL) for both perpendicular planes result which are a function of the chief ray angle. With increasing chief ray angle, the power in both sections increases leading to shorter BFLs which results in curved image planes for the two sections (Fig. 2.3). However, even if no astigmatism would be present, the image field of a singlet will still be curved due to the Petzval field curvature. The tangential and the sagittal foci coincide at the Gaussian

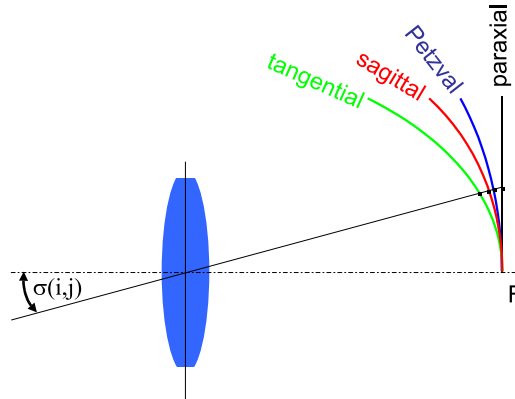


Figure 2.3: Schematic drawing of the different inward curved image planes for a spherical lens with positive power displaying the tangential, sagittal, Petzval, and Gaussian or paraxial image plane in principle.

image plane and no astigmatism occurs for the on-axis field. With increasing chief ray angles, the astigmatic difference being the difference of the tangential and sagittal BFL measured along the chief ray increases. Consequently, the spot in the Gaussian image plane blurs which is connected with a loss of resolution. The tangential and sagittal BFLs s'_t and s'_s can be calculated using the Gullstrand's equations

$$\Delta\left(\frac{n}{s_t} \cos^2 \sigma\right) = \frac{1}{R} \Delta(n \cos \sigma) \quad \text{and} \quad (2.4)$$

$$\Delta\left(\frac{n}{s_s}\right) = \frac{1}{R}\Delta(n \cos \sigma). \quad (2.5)$$

These apply to small ray bundles passing through a spherical surface with a radius of curvature R formed by two materials with refractive indices n and n' .^{54,56} Herein, Δ denotes Picht's operator as the difference between object and image space variables where the latter are marked with a stroke. In this compact notation e.g. Snell's law simplifies to

$$\Delta(n \sin \sigma) = 0, \quad (2.6)$$

with σ and σ' as the chief ray angles in the object and the image space, respectively, measured with respect to the optical axis. The influence of the object distances s_t and s_s on the tangential and sagittal BFLs is negligible for distances larger than 10 times the focal length f . In a classical camera setup the entire FOV is transmitted through a single aperture, and the only way to eliminate the field aberrations is to implement additional lenses preferably made of materials with different indices of refraction which ends up in a complex and bulky optical stack. In an artificial apposition compound eye objective, each channel is assigned to a very small FOV which makes it possible to correct off-axis aberrations by an individually adapted lens. Current prototypes based on rMLA suffer from off-axis aberrations occurring under oblique incidence at spherical microlenses. The FOV of the entire camera is limited to approximately 25° when using spherical lenses with a f-number of about 2.3 as in state-of-the-art systems. This small FOV is insufficient for many industrial applications.

2.3 Hybrid imaging

Conventional imaging setups possess constant resolution over the complete image field if aberrations can be neglected. If high resolution is required as in the case of the imaging of small optical structures, rather complex, bulky, and expensive imaging optics result. In imaging dilute arrays typically found in many telecommunication applications, most of the space-bandwidth product is wasted since the area between the small points of interest is simply black or not required for the optical function.⁵⁷ A more suitable approach is the so-called hybrid imaging as a combination of micro channel and conventional imaging (Fig. 2.4).⁵⁸⁻⁶¹ Here, a first microlens array MLA1 collimates channel-wise the radiation emanating from the input sources. In a second step, a conventional 4F-setup consisting of lenses L1 and L2 images the first array MLA1 onto the second MLA2. The latter refocuses the radiation channel-wise to the output devices. Since the microlenses provide high resolution locally at the areas of interest, the hybrid imaging scheme distributes the space-bandwidth product as needed.

An optical connection between singlemode fibers must be established in many interconnection systems for telecommunication purposes.⁶² Consequently, the radiation emanating from an input fiber must be coupled into an output fiber after propagating through the free-space optical system. The radiation emanating from a singlemode fiber is spatially coherent and

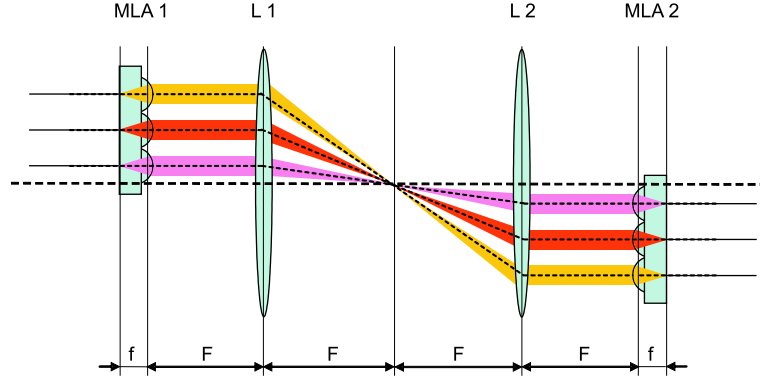


Figure 2.4: Setup of the hybrid imaging system. F - focal length of the Fourier lens, f - focal length of the microlens.

can be approximated as a Gaussian bundle.^{63–65} The amplitude distribution of the Gaussian beam is given by

$$W(x, y) = A_0 \frac{\omega_0}{\omega(z)} \exp\left(-\frac{x^2 + y^2}{\omega^2(z)}\right), \quad (2.7)$$

with $\omega(z)$ as the distance between the maximum of the distribution and the location where the intensity has dropped to $(A_0/e)^2$, and ω_0 is the minimum value of the beam radius $\omega(z=0)$ referred to as waist radius of the Gaussian beam. During the propagation in free-space not being confined by wave guiding structures, the exponential distribution retains but the beam radius changes according to

$$\omega(z) = \omega_0 \sqrt{1 + \left(\frac{\lambda z}{\pi \omega_0^2}\right)^2}, \quad (2.8)$$

where z is the distance in the propagation direction to the waist of the Gaussian beam. For large distances the beam radius is increasing linearly with z where the gradient is

$$\vartheta = \frac{\lambda}{\pi \omega_0}, \quad (2.9)$$

which is referred to as the far field divergence or numerical aperture of the Gaussian beam. A Gaussian beam is completely described by its wavelength λ and waist ω_0 . When imaged by a lens, which can be approximated as a thin lens, a transformation of the object Gaussian beam into the image beam occurs which can be derived from scalar wave theory.⁶³ The distance d_{im} between the position of the lens with focal length f and the image waist ω_{im} can be calculated by

$$d_{im} = f + \frac{(d_{ob} - f) f^2}{(d_{ob} - f)^2 + \left(\frac{\pi \omega_{ob}^2}{\lambda}\right)^2} \text{ and} \quad (2.10)$$

$$\omega_{im} = \omega_{ob} \frac{f^2}{(d_{ob} - f)^2 + \left(\frac{\pi \omega_{ob}^2}{\lambda}\right)^2}, \quad (2.11)$$

with d_{ob} and ω_{ob} as the distance of the object beam waist to the lens and the waist radius, respectively. The coupling efficiency of the mode guided by the singlemode fiber $F(x, y)$ and the incoming wave field $W(x, y)$ to be coupled is defined as⁶⁶

$$\eta_a = \frac{|\int \int F(x, y)W^*(x, y)dxdy|^2}{\int \int F(x, y)F^*(x, y)dxdy \cdot \int \int W(x, y)W^*(x, y)dxdy}. \quad (2.12)$$

The asterisk stands for the mathematical operation of the conjugated complex value. Consequently, the efficiency for coupling a Gaussian bundle with a waist ω_{01} and a singlemode fiber with the mode field radius ω_{02} yields⁶⁵

$$\eta_G = \frac{4}{\left(\frac{\omega_{01}}{\omega_{02}} + \frac{\omega_{02}}{\omega_{01}}\right)^2} \frac{1}{1 + \left[\frac{\lambda z'}{\pi(\omega_{01}^2 + \omega_{02}^2)}\right]^2}, \quad (2.13)$$

with λ as the wavelength of the radiation and z' the axial distance between the waist of the Gaussian bundle and the front surface of the fiber. Besides the defocus z' of the Gaussian bundles, lateral and angular displacements d_{fiber} and ϕ_{fiber} of the Gaussian bundle with respect to the front surface of the singlemode fiber are connected with coupling losses and can be approximated by⁶⁷

$$\eta_{d_{fiber}} = \exp\left[-\left(\frac{d_{fiber}}{d_e}\right)^2\right] \text{ and} \quad (2.14)$$

$$\eta_{\phi_{fiber}} = \exp\left[-\left(\frac{\phi_{fiber}}{\phi_e}\right)^2\right]. \quad (2.15)$$

Herein d_e and ϕ_e are normalization values given by

$$d_e = \frac{2^{1/2}}{\tau_a \cdot \left(\frac{1}{\omega_{01}^2} + \frac{1}{\omega_{02}^2}\right)^{1/2}} \text{ and} \quad (2.16)$$

$$\phi_e = \frac{2^{3/2}}{\tau_a k \cdot (\omega_1^2 + \omega_2^2)^{1/2}}. \quad (2.17)$$

Here, τ_a stands for the coupling efficiency without tilt or offset (which can be approximated as unity), $\omega_{01,2}$ the waist radius of the Gaussian bundle and the mode field radius of the singlemode fiber, k the wavenumber which equals $2\pi/\lambda$, and $\omega_{1,2}$ the field radius of the Gaussian bundle and that of the singlemode fiber which can be approximated as the waist radii $\omega_{01,2}$.

The total coupling efficiency η_{total} can be calculated by multiplying the results for η_G , $\eta_{d_{fiber}}$, and $\eta_{\phi_{fiber}}$ yielding

$$\eta_{total} = \eta_G \eta_{d_{fiber}} \eta_{\phi_{fiber}}. \quad (2.18)$$

Thus, in order to achieve maximum coupling efficiency η_{total} , the waist of the Gaussian bundle must coincide with the front face of the fiber without lateral, axial, or angular mismatch and must be of the same size as the mode field radius of the singlemode fiber. Aberrations added by the conventional part of the imaging system will lead to a decreased coupling efficiency. These can be compensated by adapting the microlenses of the considered channel of the interconnect. Since the aberrations depend on the position of the optical channel within the system, optimum performance for all channels can be achieved with a channel-wise adapted chirped MLA only.

2.4 Fly's eye condenser systems

Many applications require the transformation of the intensity distribution of a coherent laser beam into a top hat. This can be accomplished using single diffractive or refractive micro-optical beam shaping elements that are designed to direct certain fractions of the input distribution into specific angles in order to generate the desired output intensity distribution.^{30,68–71} The first suffer from their dispersive behavior and are only suited for a small spectral range. In addition, the scattered light caused by the non-continuous surface profile of the diffractive elements can be perturbing and the theoretical maximum diffraction efficiency of the diffractive elements depends on the number of height levels of the surface profile of the elements.⁷² Therefore, the fabrication of diffractive elements with high efficiency becomes especially challenging when dealing with radiation in the ultra-violet wavelength range which is of particular interest in many applications such in semiconductor industry since very small structures with high precision must be generated.⁷³ Refractive elements are suitable for a wider spectral range, and due to their continuous surface profile, they exhibit a small amount of scattered light and allow for maximum diffraction efficiency. Since they are designed for a given input intensity distribution, any changes in this distribution will lead to a distorted output distribution.^{71,74} Consequently, temporal fluctuations of the input distribution cannot be tolerated, and tight position tolerances during alignment are obstacles in their practical application. Other widely used solutions are fly's eye condenser setups known from microscope illumination systems. The setup usually consists of a Fourier lens and two identical regular microlens arrays - often referred to as tandem lens array - where the second one is placed in the focal plane of the first microlenses (Fig. 2.5).^{26–28,75} This type of beam homogenizer offers many advantages. Due to the use of refractive microlenses, the dispersion and the generation of stray light are much smaller compared to diffractive approaches. As a further advantage, the position of the MLA with respect to the radiant source can be chosen almost arbitrarily. This allows for both, easy assembly and insensitivity to temporal fluctuation of the input intensity distribution. These advantages especially contribute to the spread of this type of homogenizers in industrial applications. The effect of homogenization is achieved by overlaying the fractions of the input radiation transmitted by each channel of the tandem microlens array in the focal plane of the Fourier lens. From the point of view of geometrical optics, the

more channels are used the better the homogenization. However, these considerations neglect coherent effects. Figure 2.6 displays the qualitative intensity distribution of an input beam with Gaussian characteristics and after passing a fly's eye condenser with a different number of illuminated cylindrical lenses. As a consequence, the output intensity distribution is almost independent of the input distribution if only enough channels are used for the homogenization. In order to avoid cross talk between the single channels, the numerical aperture of the input radiation must not exceed the numerical aperture of the microlenses. However, due to the spatial coherence of the setup and the use of many optical channels in parallel, multiple-beam interference will occur even in case of temporally incoherent sources.^{76,77} A detailed treatment of the use of fly's eye condensers for incoherent sources like LEDs is given in Refs. 78, 79. Coherent effects dominate the appearance of the intensity distribution in the focal

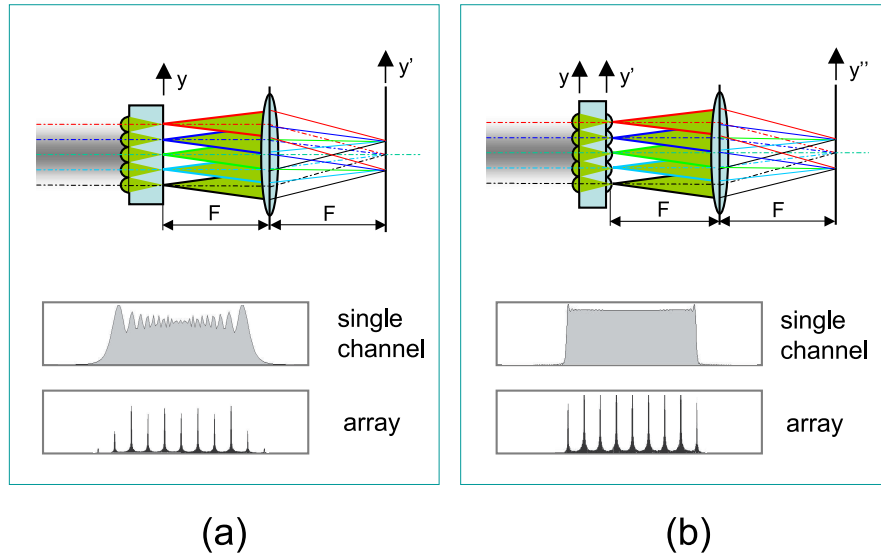


Figure 2.5: Comparison of fly's eye condenser types. *Top*: Schematic drawing of setup. *Bottom*: Far field intensity distribution of single channel and lens array. (a) using a single rMLA, (b) using a tandem rMLA. F - focal length of Fourier lens, y , y' and y'' - coordinate axes at different propagation distances.

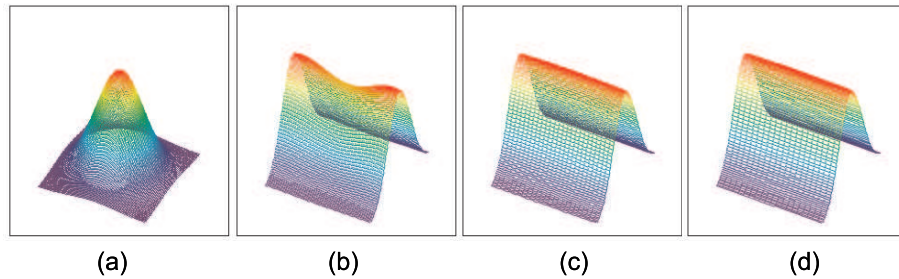


Figure 2.6: Two-dimensional intensity distributions in arbitrary units. (a) Gaussian distribution as input to a fly's eye condenser, resulting output distributions after the tandem fly's eye condenser when illuminating different numbers of cylindrical lenses N : (b) $N=2$, (c) $N=4$, (d) $N=6$. Homogeneity along beam shaped axis is about 5% for $N>5$. Due to the cylindrical lenses beam shaping is accomplished in one dimension only. Here, spatial and temporal incoherence between the single channels is assumed.

plane of the Fourier lens when considering temporally coherent radiation sources ideally with infinite coherence length. In the presented work, all wave optical considerations are based on the scalar wave theory and consider the approximations to the non-vectorial character of the radiation, optical elements being described as thin elements and the limitation to the paraxial region.^{28,80,81} Also, a one-dimensional treatment is sufficient since the considered fly's eye condensers use cylindrical lenses. The field distribution $u(y')$ is examined in the focal plane of lenses with the focal length f . Consequently, the diffraction integral can be used in the Fraunhofer approximation⁸⁰

$$u(y') = \frac{\exp(jf \cdot 2\pi/\lambda)}{j\lambda f} \exp\left(j\frac{\pi y'^2}{\lambda f}\right) \cdot \int_{-\infty}^{\infty} u(y) \exp(-j2\pi\nu y) dy, \quad (2.19)$$

with $u(y)$ as the complex amplitude in the object plane located in the front focal length of the Fourier lens and ν as the spatial frequency which holds

$$\nu = \frac{y'}{f\lambda}. \quad (2.20)$$

Here, y and y' are the coordinates measured in the object and image space, respectively (Fig. 2.5). The term in front of the integral of Eq. (2.19) describes the phase of the field which is of minor interest and consequently neglected in order to simplify the mathematical treatment. The integral itself describes a Fourier transformation and the field distribution in the focal plane of a lens can be calculated by

$$u(y') \propto F\{u(y)\}. \quad (2.21)$$

For a wave optical description of a fly's eye condenser, the field after the propagation through the MLA - which is referred to as transmission function of the array - must be known. In the case of regular arrays, the transmission function can be written as the convolution of the transmission function of one channel and a comb-function that encodes the positions of the single lenses multiplied with the transmission function of the aperture of the entire array

$$u(y'') \propto F\left\{\text{comb}\left(\frac{y'}{p}\right) \otimes T(y') \cdot \text{rect}\left(\frac{y'}{p \cdot N}\right)\right\}, \quad (2.22)$$

with p as the pitch of the lenses, N the number of lenses in the array and y' as the coordinate in the focal plane of the first microlenses. Thus, the field amplitude in the focal plane of the Fourier lens is a series of equidistant peaks each with a sinc-distribution with an envelope of the Fourier transformed transmission function of one optical channel of the MLA

$$u(y'') \propto p^2 N \cdot \text{comb}(py'') \cdot F\{T(y')\} \otimes \text{sinc}(pN \cdot y''), \quad (2.23)$$

where the sinc-function is defined as

$$\text{sinc}(x) = \frac{\sin(\pi x)}{\pi x}. \quad (2.24)$$

The modulation due to the comb clearly degrades the homogenization. According to Eq. (2.23), the envelope of the far field distribution $u(y'')$ in the focal plane of the Fourier lens is given by the Fourier transformation of the transmission function $T(y')$ of the optical channels of the MLA. This can be calculated by a step-wise propagation through the array. The field distribution in the focal plane of the first lens is given by the Fourier transformation of the aperture of the first lens with width $2a$ and focal length f

$$u(y') \propto F_f \left\{ \text{rect} \left(\frac{y}{2a} \right) \right\}, \quad (2.25)$$

which yields

$$u(y') \propto 2a \cdot \text{sinc}(2a\nu). \quad (2.26)$$

The amplitude of the field in the focal plane of the first lenses therefore is

$$u(y') \propto \text{sinc} \left(\frac{2a \cdot y'}{f\lambda} \right). \quad (2.27)$$

The ratio of the focal length of a lens over its aperture size determines the f-number η

$$\eta = \frac{f}{2a}. \quad (2.28)$$

The numerical aperture μ of the lens in a paraxial approximation is given by⁵³

$$\mu = \frac{a_i}{f_i} = \frac{1}{2\eta}. \quad (2.29)$$

When inserting Eq. (2.28) into Eq. (2.27) it becomes obvious that the field depends on the f-number and the wavelength only

$$u(y') \propto \text{sinc} \left(\frac{y'}{\eta\lambda} \right). \quad (2.30)$$

The field in the focal plane of the first lens has a spherical phase distribution. Its Fourier transformation being the envelope of the far field intensity distribution, exhibits some modulation and soft shoulders [Fig. 2.5(a)] and differs clearly from the required top hat. In a tandem setup using two MLA, the second lens of each channel flattens the phase in the focus of the first lens. Therefore, again this generates a field with an amplitude with a sinc-distribution but with a plane phase. In addition, the field is clipped due to the finite aperture size of the second microlens

$$u(y') = T(y') \propto \text{sinc} \left(\frac{y'}{\eta\lambda} \right) \cdot \text{rect} \left(\frac{y'}{2a} \right). \quad (2.31)$$

The envelope of the far field intensity distribution therefore holds

$$u(y'') \propto \text{rect}(\nu' \lambda \eta) \otimes \text{sinc}(2a\nu'). \quad (2.32)$$

Inserting Eqs. (2.29) and (2.20) finally yields

$$u(y'') \propto \text{rect}\left(\frac{y''}{2F\mu}\right) \otimes \text{sinc}\left(\frac{y''2a}{\lambda F}\right). \quad (2.33)$$

The first term of the convolution describes the top hat which has a width of $2F\mu$. The second term is due to the clipping of the angular spectrum at the aperture of the second lens. In the case of an infinite aperture, no clipping would occur and the sinc-function would converge to a δ -function leading to an envelope of a perfect top hat [Fig. 2.5(b)].

The biggest disadvantage of using regular arrays in fly's eye condenser setups is the appearance of equidistant sharp intensity peaks which is caused by the periodic structure of the regular tandem microlens array and leads to a limited homogeneity. These periodic intensity peaks can be avoided when breaking the periodicity of the regular MLAs and using adapted chirped ones instead.

3 Fundamentals of chirped microlens arrays

3.1 Definition

Conventional arrays consist of a repetitive arrangement of a unit cell on a fixed, equidistantly sectioned grid. The topology of the array is completely described by the parameters of the unit cell defining the surface profile $\Psi_0(x, y)$ of the microlens and the array parameters pitch P_x and P_y and the number of lenses N_x and N_y in the x- and the y-direction (Fig. 3.1). This static arrangement is disadvantageous for many applications because the cells cannot be

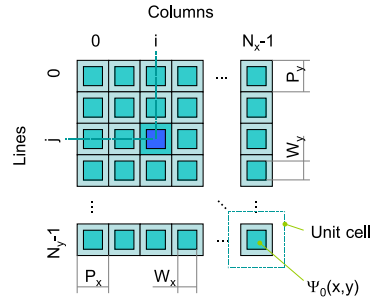


Figure 3.1: Schematic drawing of one type of a regular microlens array with orthogonal and equal pitches in x- and y-direction. $\Psi_0(x, y)$ -surface profile of the unit cell, $P_{x/y}$ -pitch in x- and y-direction, respectively, $N_{x/y}$ -number of lenses in x- and y-direction, respectively, $W_{x/y}$ -width of unit cell in x- and y-direction, respectively.

individually optimized for their specific optical function. Instead the design is a compromise which enables a sufficient overall performance. In contrast to these setups, in a chirped array the inflexibility of a regular arrangement has been overcome. Here, the array consists of individually shaped lenses of similar appearance that are defined by a parametric description of the cells optical function (Fig. 3.2).^{82,83} The surface topology of the single lenses $\Psi_{i,j}(x, y)$

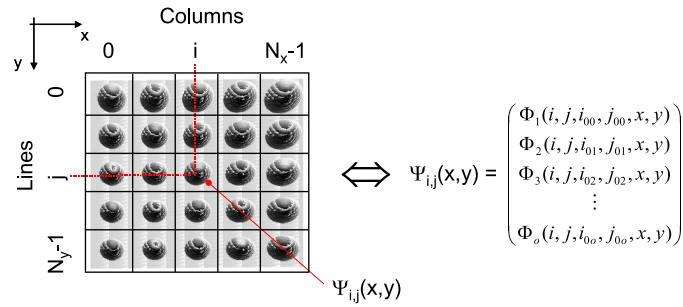


Figure 3.2: Schematic drawing of a chirped microlens array and equivalent mathematical description.

and hence of the entire array can be described in a parametric formulation whereas the number of requested parameters o depends on the geometry of the lenses. For instance, a spherical lens is completely described by the vertex position (two parameters for x and y), the radius of curvature, and the aperture diameter. Consequently, more complex structures require a larger number of parameters. Geometrical and optical aspects that depend on the

desired system performance determine the precise value of the parameters for each cell of the array. These parameters are defined by functions Φ_l that strongly depend on the geometry and optical task of the system and the position of the cell within the array indicated by its position index (i, j) . As main differences to the regular arrays, cMLAs possess neither constant pitches nor a unit cell. Instead of a unit cell, the cMLA features a reference cell indicated by the index (i_0, j_0) that defines the type of the lens and the initial values for the calculation of the other cells. The attribute “chirped” was adopted from the term “chirped Bragg gratings” which stands for a volume grating with continuously changing period as a function of the position along the direction of propagation.^{3,84–86} Therefore, the functions Φ_l that describe the cMLA are limited to continuously differentiable ones. Stochastic arrays - which are also non-regular arrays - are no chirped arrays since the array describing functions are not continuously differentiable.⁴ On the other hand, the common rMLAs are a part of the group of the cMLAs but with constant functions Φ_l that are independent of the cell index (i, j) . In conclusion, cMLAs are arrangements of microlenses whose describing parameters can be obtained from continuously differentiable functions. The parameters of the cells equal the function values sampled at the position of the cell within the array.

3.2 Classification

A variety of approaches for the classifications of cMLAs is in principle possible, e.g. according to the lens type (spherical, cylindrical, toroidal, off-axis lens segments,...), the type of chirp function (linear, polynomial,...), or the parameter that is chirped (vertex position, radius of curvature,...). However, a higher-ranking graduation rather than on a basis of the geometrical appearance of the array can be found which distinguishes between the design of the cells in an individual or a collective manner (Fig. 3.3). In the first type, the single channels do not interact or at least their interaction is not considered in the layout of the array. Here, the cells are arranged in an array due to geometrical or technological aspects such as miniaturization and cost efficient production in terms of component fabrication as well as the assembly of more complex systems. The optical design of each channel is completely isolated from that of the others. Nevertheless, the entity of the array affects the single channel design on the part of geometrical constraints such as vertex positions, high fill factor etc. only. The individual designs can be used on the one hand for the improvement of the integration, and on the other hand for the optimization of optical systems. The integration of a system can be improved by selecting the most appropriate cell of the array in order to achieve the required optical performance, while all other lenses of the array remain unused which corresponds to the most trivial field of application of cMLAs.⁸⁷ In a typical application, this can be exploited to compensate component tolerances. Further on, the utilization of a cMLA can lead to a reduced number of components necessary for achieving a special optical task.⁸⁸ It is essential in these subdivisions for improved integration that the optical performance cannot be enhanced by the cMLA. Their only - nevertheless important - benefit lies in a simplified assembly and

consequently cost reduction. In another field of application, cMLAs can be used to optimize the optical performance of a system.^{82,83} Here, usually the number of components remains constant and no advantage in terms of easier fabrication or decreased production cost can be achieved. However, the optimized performance might upgrade the systems to completely new fields of application. Examples for each field of use of cMLAs are presented in the fol-

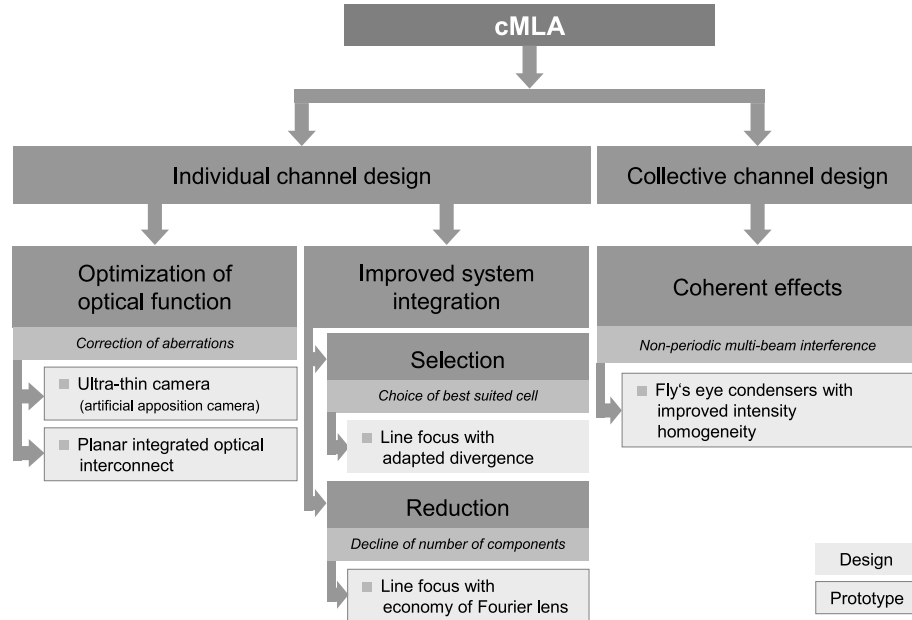


Figure 3.3: Classification of cMLAs on the basis of the channel design and listing of system designs and prototypes presented in the thesis.

lowing sections of this work reaching from designs to fabricated and characterized prototypes (Fig. 3.3). The assignment of a certain example to its category according to the proposed classification scheme is not always explicit. Application examples which are assigned to the optimization of the optical performance could also be related to the reduction of the number of components since the higher level of quality can be achieved using more elements such as sophisticated multi-element aberration corrected imaging optics instead of low cost components (Sec. 4.2.2).⁸⁹ However, the assignment was done based on state-of-the-art systems and how cMLAs could be used for an improvement with respect to the integration or the optimization of the performance.

The second group of setups deals with collective channel designs. Here, the intended optical function is a consequence of the interaction of the entirety of all channels of the array. Thus, coherent effects are of particular interest which result from both, spatial and temporal coherence of the radiation.^{90,91} Again, geometrical aspects influence the layout of the arrays but in contrast to the individual channel designs the accommodation of the channels in an arrayed structure is mandatory for obtaining the required optical function. Completely novel effects can be discovered in this field of application which are in detail described in Chap. 5 by the example of a beam homogenizing system based on a fly's eye condenser.

3.3 Derivation of cell parameters

For calculating the parameters of all cells, the functions describing the system can be acquired in three manners. These distinguish in the efforts for the derivation of the equations and the time for calculating the precise values of each lens. Usually, parameters which are influenced by geometrical conditions only can be treated in an analytical way since the functions are not very complex. In contrast to that, equations dedicated to the optical optimization (e.g. aberration polynomials) are more complex and usually cover only a section of the entire optimization problem. However, a completely analytical derivation of the functions can be accomplished if a simple formulation of the optical optimization problem is possible (Fig. 3.4). The major advantage in using analytical functions is the extremely short processing time needed for calculating the parameters of the single lenses which is especially relevant when dealing with arrays having a large number of channels. However, the efforts necessary for deriving a complete analytical description are justified only if the complexity of the underlying context is limited or a family of similar designs has to be developed.

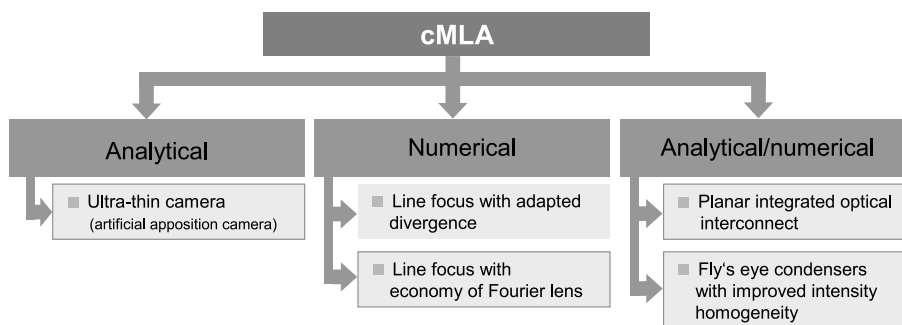


Figure 3.4: Overview of derivation methods for calculating the parameters of cMLAs and listing of related system designs and prototypes presented in the thesis.

Another possibility to determine the cell parameters is to use numerical optimization techniques which are usually implemented in optical design software tools like ray tracers or wave optical simulation solutions.^{92–95} Here, the boundary conditions and the optical performance parameters are implemented as operators in a quality function which is referred to as merit function.^{96,97} Weights can be used in order to account for different levels of importance of the various operands. The performance of the optical system is then quantitatively described by a single number whereas the larger the value the worse the performance. A value of the merit function of zero represents the optimum setup. Different types of numerical optimization techniques can be used to find a setup which fulfills the specifications by minimizing the value of the merit function. The unsurpassed flexibility is the biggest advantage of this technique. In addition, it might be the only way for a sufficiently accurate optimization if the physical background describing the optical system becomes more complex. However, due to comparatively long optimization times it is especially suited for arrays with a small number of cells.

A third approach can be understood as a combination of the numerical and analytical deriva-

tion and is based on the numerical optimization of a small number of significant cells and a subsequent interpolation for calculating the parameters of the entire array. This is a practical and time efficient way because it separates the design task in two parts and combines the advantages of both approaches. Firstly, numerical optimization techniques are employed to find the parameters of a few significant cells, avoiding the time consuming efforts to figure out an adequate analytical description. Secondly, the use of fitted functions enables the extremely fast calculation of the parameters of the entire array.⁹⁸ However, the use of interpolation functions involves always the risk of discrepancies between the really best suited and the calculated values. Consequently, this approach can be employed only if the context legitimates its acceptance. The application of the fitted functions will lead to wrong parameters in case of an unsteadily functional context or when the sampling is insufficient. A verification of the results is considered to be indispensable which is usually much less time consuming compared to the optimization of the whole microlens array cell by cell.⁸⁹

3.4 Fabrication methods

A variety of methods for the fabrication of refractive microlenses have been developed over the last decades. Refractive lenses with constant index of refraction based on curved surface profiles [no gradient-index (GRIN) lenses⁹⁹] have been used exclusively in the presented prototypes of the thesis. Their fabrication techniques can be divided into methods based on physical effects which lead to the desired surface profile such as surface tension, direct writing methods and precision micro-machining based on diamond turning or ablation.^{1,28,48,100} The first group contains reflow of photoresist,^{101–104} mass transport mechanisms in semiconductors,^{105,106} local swelling of polymers and glasses,^{107,108} and dispensed droplets.^{109,110} Popular representatives of direct writing methods are laser and electron beam lithography.^{111–114} All methods have their specific advantages and limitations whereas direct writing methods especially benefit from the enhanced freedom of the possible surface profiles such as the ability to create non-symmetric structures. Reflow of photoresist and laser lithography have achieved prominent relevance among all technological approaches in both, scientific as well as industrial applications.^{4,5} All prototypes fabricated in the scope of this thesis are based on these two methods. As a relatively novel technique for the generation of micro-optical components, 2-photon polymerization is introduced as direct writing method with the opportunity to fabricate almost arbitrary surface profiles.^{115,116} Figure 3.5 gives an overview of the fabrication methods and the example systems discussed in the thesis.

3.4.1 Reflow of photoresist specific to cMLA

Reflow of photoresist is one of the most often applied techniques for the fabrication of refractive microlenses. It is capable of producing smooth and well defined spherical surfaces^{117–120} often

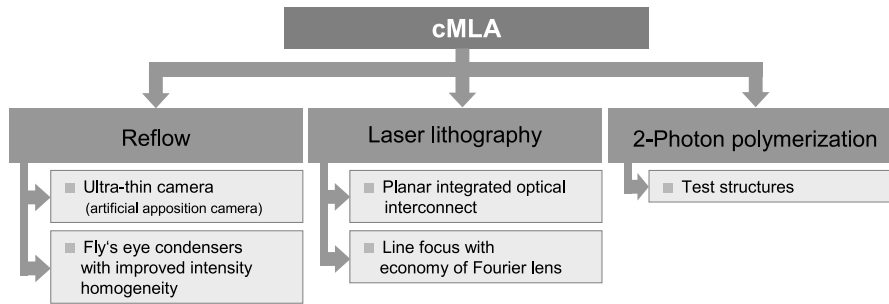


Figure 3.5: Overview of fabrication methods of cMLAs examined in the thesis and listing of related system designs and prototypes.

used for imaging applications.¹²¹ In this process, cylinders of photoresist are melted leading to a 3D-surface which is formed by surface tension effects (Fig. 3.6). Therefore, the profile of the resulting surface depends on the volume of the resist cylinder to be melted and the shape of its rim. The rim of a lens is defined by an exposure through a photo lithographic mask while the volume depends on the area bordered by the rim and the height of the photoresist which is constant over the entire array. Stringent limitations to viable rim geometries and thus to the three-dimensional surfaces apply which make rectangles (cylindrical lenses), circles (spherical lenses), and ellipses (anamorphic lenses) the most useful forms (Tab. 3.1).^{101–103, 122, 123} The mask determining the bases of the lenses must consist of individually shaped cells in order to create a cMLA. Commercially available software solutions for mask generation are capable of creating repetitive structures only which are sufficient for the fabrication of conventional regular arrays. Consequently, adapted software tools had to be developed for the generation of cMLAs. The task was split into three main steps in order to minimize the efforts in programming, to be as versatile as possible and at the same time compatible to existing standards:¹²⁴

1. Calculation of the lens parameters of each cell,
2. Generation of a text-file containing the geometrical information of the rim structures of the entire cMLA,
3. Automated generation of a drawing of the entire mask using a standard CAD software.

The task sharing enables maximized flexibility of the software since especially for the derivation of the cell parameters by numerical optimization many different software solutions with inhomogeneous scripting or programming are used such as different types of ray tracers or wave optical simulation software. In this approach, the outcome of step 1 are *Microsoft*[®] *Excel* files that consist of as many columns and rows as the later lens array. This is independent of the software being used for generating the parameters of the cells. A different number of parameters and files are necessary depending on the shape of the lenses to be described (Tab. 3.1).

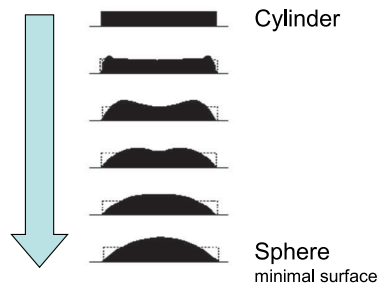


Figure 3.6: Schematic drawing for the explanation of reflow of photoresist. The process starts from a rigid cylinder of photoresist (top). During the melting process the photoresist softens until the entire volume is liquid. A spherical shape results caused by the surface tension. Finally, the photoresist hardens again and retains its shape.

Table 3.1: Lens types fabricated by reflow of photoresist and their parametric mask description.

Lens type	Shape of rim	Mask parameters
Spherical	Circle	Center x Center y Radius
Cylindrical	Rectangle	Center x Center y Width x Width y
Anamorphic	Ellipse	Center x Center y Major axis Minor axis Orientation angle

Usually, the radii of curvature, aperture sizes, and positions of the lenses are the outcome of the optics simulation which have to be transferred into a mask layout. With the presumption of volume preservation - taken into account a technology specific shrinkage factor - this is simply done by equating the volume of the resist cylinder and that of the lens. After having all cell parameters collected and transferred into the mask parameters of the cells, in the second step a text-file containing all required coordinates for drawing the mask is automatically generated which can additionally be manipulated in an ordinary text editor. In the third step, the drawing of the mask as a dxf-file is automatically generated within *Autodesk[®] Mechanical DesktopTM* using a macro written in *AutoLISPTM* which interprets the text-file containing the geometrical data of the entire array.¹²⁵ The dxf-file is then completed by alignment marks and is finally converted into a GDSII-file readable by the e-beam lithographic exposure machine.^{126, 127} A block diagram summarizing the data flow for the mask generation of the cMLA is given in Fig. 3.7.

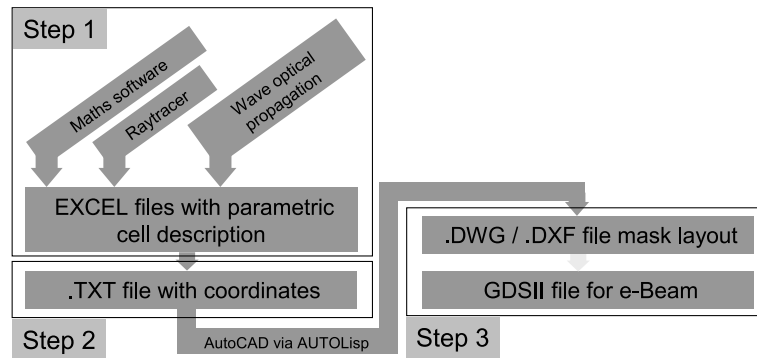


Figure 3.7: Block diagram explaining the data flow for the generation of a chirped lithographic mask required for reflow of photoresist.

In the above described classical reflow technology, the volume of the resist to be melted is determined by the area of the final lens and the resist height which is constant for all cylinders. More freedom in the design can be accomplished if a technique using two exposure steps and consequently two masks is employed.⁹⁰ In a first lithographic step, the bases of the lenses are structured on the substrate using a first mask. A subsequent etching step is carried out after the development of the resist in order to create pedestals that define the rim of the later lenses (Fig. 3.8). Then the photoresist used for the reflow is spin-coated on top of the patterned layer. The cylinders to be melted are defined in a second exposure step. They have smaller extension than the bases of the lenses and can be chosen arbitrarily for each individual cell. The resist volume defined by a second mask will form a minimum surface in the subsequent melting process which has a footprint created by the first exposure as the boundary rim. The

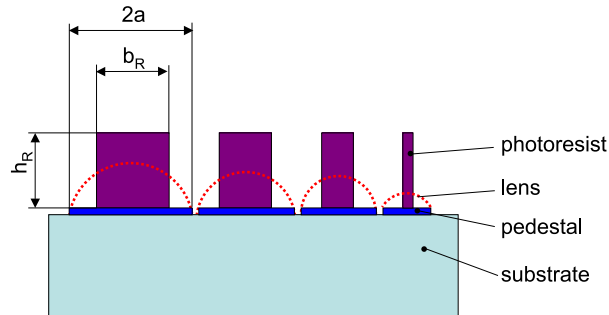


Figure 3.8: Schematic drawing of a cross section of the photoresist cuboids on a substrate before melting and of the lenses after the reflow. Pedestals are required for the definition of the bases of the lenses. $2a$ - width of the lens, b_R - width of the resist cuboid, h_R - height of the resist cuboid.

calculation of the mask design based on the two-mask-principle is explained by the example of a cMLA of cylindrical lenses. In case of such a one-dimensional lens, the condition of volume preservation can be simplified to the parity of the cross section areas of the cylindrical lens and the resist cuboid. The cross section area of the lens can be calculated by simple geometrical

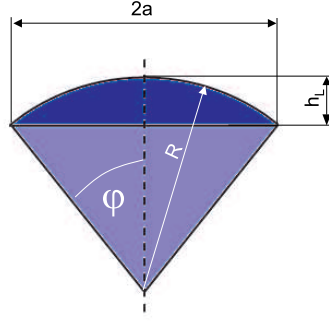


Figure 3.9: Schematic drawing of a cross section of a spherical lens. $2a$ - width of the lens, h_L - vertex height of the lens, R - radius of curvature.

considerations. According to Fig. 3.9 it is obvious that

$$\tan \varphi = \frac{a_i}{R_i - h_{L_i}}, \quad (3.1)$$

with R_i and h_{L_i} as the radius of curvature and the vertex height of the lens, respectively. The radius of curvature is given by

$$R_i = f_i (n - 1), \quad (3.2)$$

where f_i is the focal length and n is the index of refraction of the material of the lens. The area A_{S_i} of a sector of a circle with a half-angle φ is given by

$$\frac{\pi R_i^2}{2\pi} = \frac{A_{S_i}}{2\varphi}, \quad (3.3)$$

which yields

$$A_{S_i} = R_i^2 \arctan \left(\frac{a_i}{\sqrt{R_i^2 - a_i^2}} \right). \quad (3.4)$$

Consequently, the cross section area of the lens can be calculated by

$$A_{\cap_i} = R_i^2 \arctan \left(\frac{a_i}{\sqrt{R_i^2 - a_i^2}} \right) - a_i \sqrt{R_i^2 - a_i^2}. \quad (3.5)$$

On the other hand, the cross section area of the resist cuboid is given by

$$A_{R_i} = b_{R_i} \cdot h_R. \quad (3.6)$$

The volume of the resist during the reflow is not exactly preserved. A factor v_S has to be introduced which accounts for the shrinkage effects. Therefore

$$A_{R_i} = \frac{A_{\cap_i}}{v_S}, \quad (3.7)$$

must be valid. The shrinkage factor depends on the specific process conduct of the reflow. Usually a shrinkage of about 10 to 15% can be observed.⁹⁰ Finally, the width of the cuboid to be melted can be calculated by

$$b_{R_i} = \frac{R_i^2 \arctan\left(\frac{a_i}{\sqrt{R_i^2 - a_i^2}}\right) - a_i \sqrt{R_i^2 - a_i^2}}{v_S \cdot h_R}. \quad (3.8)$$

The values for the widths $2a_i$ and radii of curvature R_i result from the parametric description of the cMLA and depend on the specific optical design.

3.4.2 Direct writing techniques specific to cMLA

Direct writing techniques can be graduated into two categories. The first takes advantage of the analogue dependency of a physical property such as the solubility on the exposed radiation dose. This dependency manifests in the so-called gradation curve of a photo sensitive material like a photoresist. Almost arbitrary surface profiles can be fabricated by locally varying the exposure dose during the writing due to the locally different solubility. This leads to extended design possibilities. Continuous height profiles can be fabricated by continuously changing the exposure radiation. The mapping of the surface to be generated onto a two-dimensional grid and subdividing into pixels is a common approach being used exclusively for the origination of the prototypes of this thesis. The surface profile is approximated by a staircase structure using discrete height levels which equal discrete laser intensity levels when writing the structure. Consequently, a quasi-continuous height profile results. Laser and electron beam lithography are prominent examples for this type of direct writing techniques. In the second category, the exposed dose is constant but here finite volume pixels (voxels) are addressed in a three-dimensional manner in order to generate the surface profile which is known as rapid prototyping technology. One relatively new approach is to use 2-photon polymerization for the rapid prototyping of micro-optical components. An increased surface roughness is common to both categories which is due to the spatial and dose discretization and further on to the fluctuations of the intensity of the writing beam during the exposure. In consequence, this leads to a limited optical performance. The large amount of data necessary for representing the cells and consequently for the entire array which strongly depends on the required number of pixels is a further aspect to be considered. Since the arrays might be used in imaging optical systems, diffraction limited performance is desired. This is especially challenging when aiming for refractive micro-optical elements with sag heights of several ten microns and large discontinuities in the surface profile such as in arrays of off-axis lens segments.

Laser lithography specific to cMLA The direct writing of the optical structures by laser lithography is an evolving technology for the fabrication of asymmetrical lens profiles.¹²⁸ Here, a tightly focused beam is scanned over a photo sensitive layer while its intensity is modulated. Different height levels of the structure result after a subsequent development step according to the locally deposited dose. This technology is especially suited for the generation of diffractive elements.¹²⁹ However, the method can also be used to create refractive micro-optical elements.^{4,112} The number of different steps - often referred to as gray levels - is machine-dependent. The pixel size (usually around $0.5\mu m$) and the total extent of the array determine the size of the computer files containing the topology data of the structures to be generated and might be several gigabyte (GB) big.

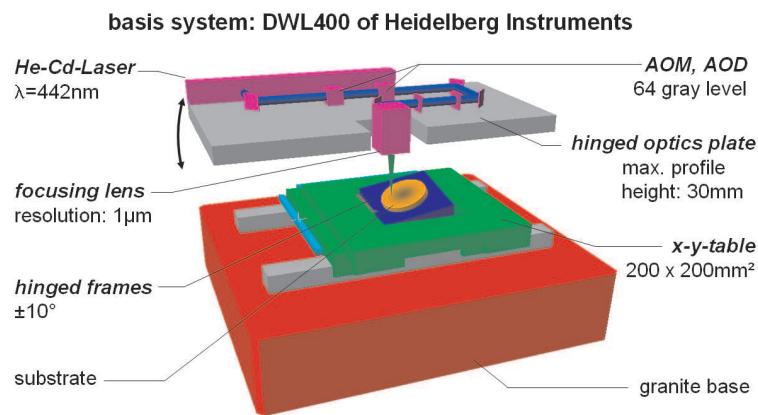


Figure 3.10: Sketch of the relevant components of a laser lithographic exposure machine with the ability to write on curved surfaces.

An obstacle one has to face in case of structures with large sag heights results from the limited number of intensity levels of the laser lithography system. The machine used to generate the prototypes demonstrated in the thesis (modified *Heidelberg Instruments DWL 400*¹³⁰) is capable of addressing 64 gray levels and corresponding height levels in one exposure step. Considering a structure height of several ten microns, a height discretization of $\lambda/2$ and larger results which can be interpreted as the peak to valley value of the profile deviation. According to the Rayleigh criterion,^{28,81} the system will inherently not be able to obtain diffraction limited performance even without the appearance of any other fabrication errors. A refinement of the minimal step height can be accomplished by using an adapted writing scheme based on the decomposition of the structure into a coarse and a fine structure (Fig. 3.11).⁸⁹ For a refinement by a factor M , the coarse structure of the entire array has to be written $(M-1)$ times. The resulting profile due to the exposure of the coarse structure would lead to something looking like a step pyramid (Fig. 3.11 bluish colored areas). In a final exposure step, the fine structure is written into the resist (Fig. 3.11 yellowish colored areas) in order to approximate the desired profile with smaller deviations. Figure 3.12 shows a grayscale drawing of the coarse [Fig. 3.12(a)] and the fine structure [Fig. 3.12(b)] for a section of a cMLA of off-axis lens segments.

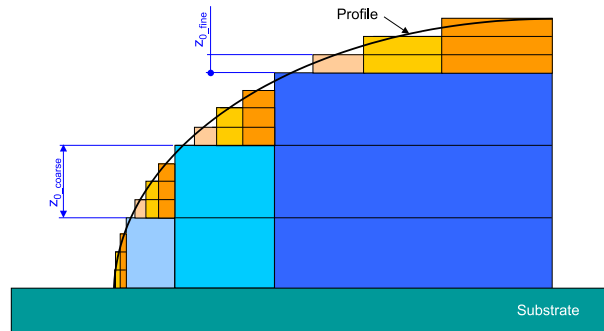


Figure 3.11: Schematic drawing for the explanation of the direct writing plotting scheme of lenses with large vertex heights by laser lithography. Bluish areas are to be exposed when writing the coarse structure, the yellowish colored areas correspond to the features generated when writing the fine structure.

Adapted software tools had to be developed in order to generate the required data for the laser writing of the arrays (Fig. 3.13). The array describing parameters obtained by using optics simulation software and a possibly subsequent fitting algorithm are organized in a text-file. The parametric description is subsequently converted into a grayscale pixel graphic where the various gray levels represent different height levels. Thereafter, the decomposition into the coarse and the fine structure is carried out. Finally, the machine readable data files are generated via an intermediate conversion step into a dxf-file. Data files with sizes of several GB have to be generated since in this approach an intermediate pixel-wise array representation is required. This is clearly disadvantageous but can be considered as the most versatile straight forward approach to solve the data processing problems in a time efficient manner. The dose deposited in the resists for creating the deepest structures has to be adapted to the sensitivity of the resist and the subsequent development process in order to achieve the desired surface profile. Figure 3.12(c) shows a microscopic image of the resulting chirped array of off-axis lens segments. The coarse structure can clearly be recognized visually but is hardly recognizable in the measurements of the surface profiles (Sec. 4.2.2).

2-Photon polymerization As a third method for the fabrication of cMLAs especially suited for the generation of non-rotation-symmetric lenses with large sag heights, 2-photon polymerization was examined. In this rapid prototyping method a small volume of an UV-curing organic-inorganic copolymer (*Ormocer*^{®131–133}) is hardened in the tight focus of the near infrared writing beam of a femtosecond titanium-sapphire oscillator.¹¹⁵ The curing process is started by 2-photon absorption of the infrared laser radiation by starter molecules and their subsequent radicalization leading to the polymerization of the copolymer. A computer controlled three-dimensional piezoelectric translation stage is used to address the volume pixel to be exposed. This technology gives the opportunity to create almost arbitrary surfaces with feature sizes in the sub- μm range since the three-dimensional structure is created layer by layer. Regarding the variety of possible surface profiles and the achievable sag

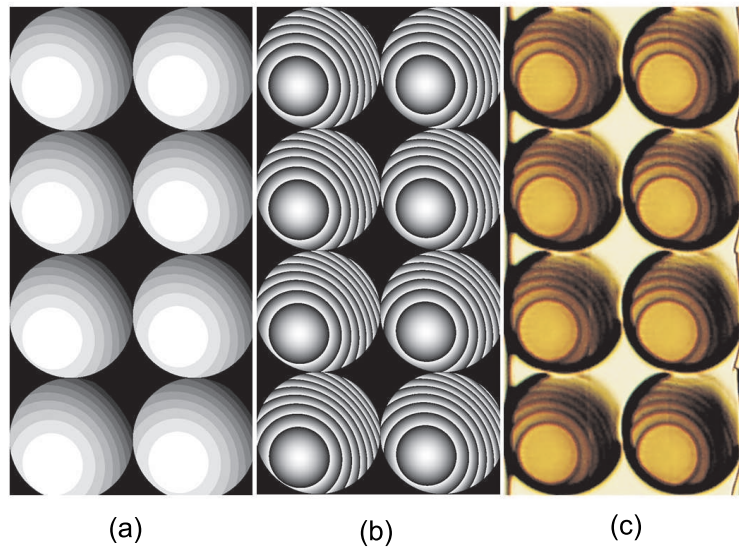


Figure 3.12: Grayscale drawing of the splitting scheme for (a) the coarse structures and (b) the fine structures for a detail of the array. (c) Light microscopic image of the corresponding laser written structure.

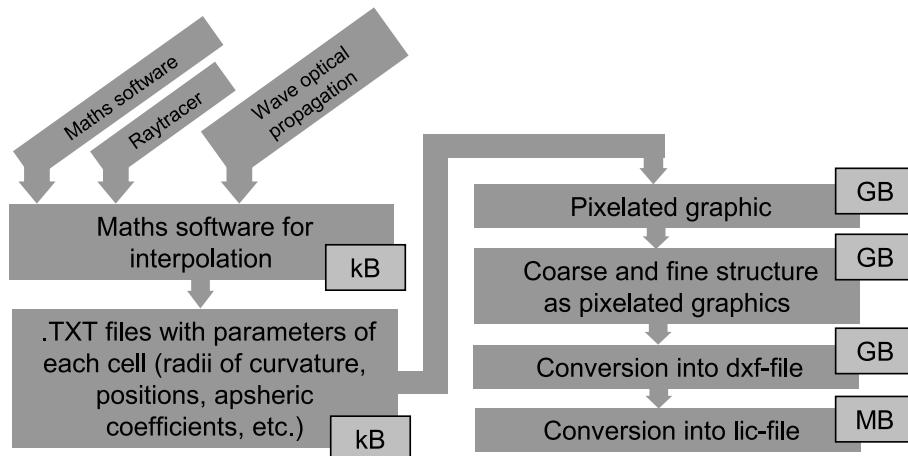


Figure 3.13: Block diagram explaining the flow for the generation of the exposure data for laser lithography and statement of the magnitude of the size of the files representing the array in the intermediate conversion steps.

heights, 2-photon polymerization is superior to laser lithography. However, key performance parameters of the micro-optical elements are the deviations of the surface profile in terms of peak to valley deviation and surface roughness. Simple test objects were fabricated at the *Laserzentrum Hannover (LZH)*¹²⁴ as a first step since this technology was not used for the fabrication of micro-optical elements so far. Measurements of the surface quality were obtained from a prototyped cube of $60 \times 60 \times 25 \mu\text{m}^3$ (length x width x height) and a prism structure of $70 \times 70 \times 103 \mu\text{m}^3$ using a white light interferometer (*MicroMap 512*¹³⁴). A peak to valley deviation of about $2 \mu\text{m}$ and a surface roughness of approximately 100nm resulted which are due to shrinkage effects and fluctuations in the laser power during the writing. Though the acceptable surface deviation values give confidence to exploit this technology for micro-optical

element fabrication, no steep edges in the surface profile could be generated which is required in many designs. Another disadvantage of the technology is caused by the long exposure time since three-dimensional voxels have to be addressed to generate the structures. Even being a promising candidate, no fabrication of a cMLA was executed by 2-photon polymerization for any prototype presented in this work. However, due to its versatility this technique seems to be worth of further research on the generation of refractive micro-optical components.

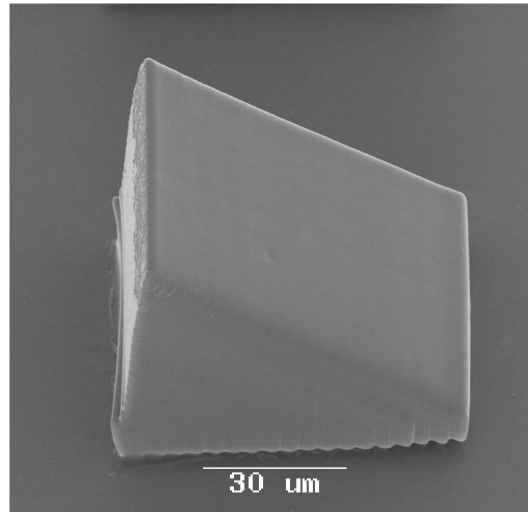


Figure 3.14: SEM picture of a microprism manufactured by 2-photon polymerization (courtesy of Laserzentrum Hannover).

4 Individual channel design

This first chapter on examples for the application of cMLAs is dedicated to systems where the design of each channel of the array is performed independently. Consequently, there is no interaction of a multitude of channels or if so, the effects are neglected in the design. However, in the majority of applications there is no interaction which originates from a spatial separation of the operation regions of the channels. Systems based on an individual channel design form arrays which result from geometrical or technological aspects like miniaturization and cost efficient production. In the following section, systems for the two fields of application for improving the degree of integration of an optical system are discussed in detail.

4.1 cMLA for improved system integration

4.1.1 Selection of best suited channel

A design of a beam shaping optical system as an example for the most trivial application of a cMLA is discussed which distributes the radiation of a singlemode semiconductor laser (laser diode *Hitachi HD 6320*¹³⁵) into a homogenized line focus. The distribution ought to have an appearance according to Fig. 2.6(d) with constant intensity along the length of the line and a Gaussian distribution in the perpendicular direction (width of the line). The distribution of the source is similar to Fig. 2.6(a) and can be described as an ellipsoidal Gaussian beam with different waist radii in perpendicular directions. The asymmetry of the beam is caused by the geometry of the laser waveguide where its width usually exceeds its thickness.²⁸ Consequently, different waists result which lead to different divergences caused by diffraction at the exit facet of the laser. According to Eq. (2.9), a small waist will lead to a large divergence. This direction is referred to as the fast axis (FA) of the laser diode. The divergence in the perpendicular direction to the FA is minimal which is referred to as the slow axis (SA). As a special peculiarity of the discussed setup, tight tolerances apply to the width of the line in a given working distance and the divergence of the beam in the non-homogenized direction (Tab. 4.1). The width and thickness of the radiation emitting waveguide varies which is inherent to the fabrication process of the laser diodes. Consequently, variations of the waists and the divergences in the SA and FA result which lead to deviations of the width and divergence of the line focus. The most perspicuous solution in order to meet the systems specifications would be the pre-selection of the laser diodes accounting for the SA divergence. However, this would increase the scrap of the laser diodes or at least would be time consuming and thus not cost effective. Another solution is to implement a customizable subsystem in order to compensate the variations in an optical manner. Therefore, an optical subsystem can be implemented with an adaptable magnification in the direction of the SA in order to generate a constant image waist whatever the size of the object waist is. This can easily be accomplished using an anamorphic telescope based on cylindrical lenses. Since the divergence of the beam is allowed to have a certain tolerance, it is possible to use discretely staged

Table 4.1: Component and system specifications of the line focus generating optical system using a cMLA for the selection of the best suited cell in order to compensate fabrication tolerances of the laser diode.

Feature	value
Laser diode	<i>Hitachi HL6320</i>
Wavelength	$(635 \pm 5)nm$
Divergence of laser diode in slow axis	$5...11^\circ @ FWHM$
Far field divergence in slow axis after line focus	$(0.3 \pm 0.01)^\circ$
Working distance measured from facet of laser diode	200mm
Width of line focus ($1/e^2$)	$(700 \pm 20)\mu m$
Homogeneity of line focus in fast axis	5%

components instead of continuously changing ones such as zoom systems. The basic idea is to use an anamorphic Galilean telescope consisting of a cylindrical lens of positive power and an array of microlenses with varying negative power which forms a cMLA. Depending on the actual waist and thus divergence of the laser diode, one of the cells of the MLA is selected to adapt the magnification of the telescope and finally meet the specifications of the system whereas the other lenses remain unused (Fig. 4.1).

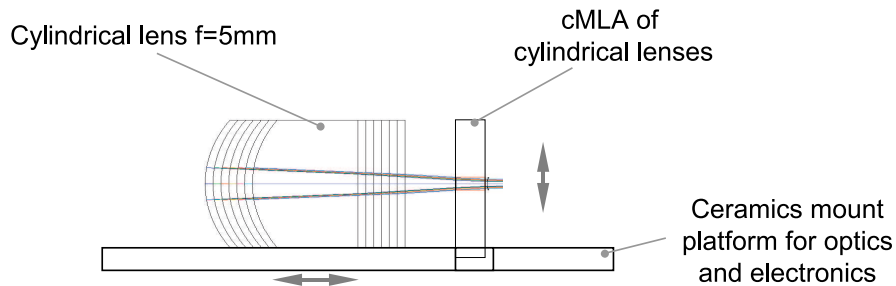


Figure 4.1: Schematic drawing of the cylindrical lens telescope for adjusting the divergence in the slow axis of a laser diode. The cMLA consists of seven cylindrical lenses of varying focal length. The position of the first lens has to be adapted depending on the selected lenslet of the array.

Optical design The setup uses a fly's eye condenser with a regular cylindrical tandem microlens array [Fig. 2.5(b)]. A commercial aspherical lens (*Lightpath[®] GeltechTM 352110*¹³⁶) is used for collimating the radiation emanating from the laser diode. The tandem cylindrical MLA is orientated in such a manner that the homogenization will be done in the FA. Thus, the telescope is active in the SA of the laser diode. The SA- and FA-direction can be treated independently of each other since the optical system uses cylindrical lenses exclusively. The optical design of the actual fly's eye condenser being active in the FA direction is not explicated

here but in other sections for similar systems (Secs. 4.1.2 and 5) because this paragraph is dedicated to the use of cMLAs for the improvement of integration. The divergence of the Gaussian beam depends on the waist and the wavelength of the beam only according to Eq. (2.9). Therefore, the optical system has to generate an image waist of $38.6\mu m$ in order to accomplish the required divergence of 0.3° . The distance of the image waist to the line focus can be calculated to be $66.4mm$ using Eq. (2.8) in order to achieve a line width of $700\mu m$. Consequently, the anamorphic telescope in collaboration with the collimation asphere has to transform the object waist of the laser diode into this image waist at this certain position. The object waists can be calculated from

$$\omega_{0SA} = \frac{\lambda}{0.8493 \cdot \pi \cdot \vartheta_{SA}}, \quad (4.1)$$

where the factor 0.8493 accounts for the declaration of the divergence in terms of the FWHM (data sheet) and $1/e^2$ -widths (Gaussian beam description)⁹⁴ and ϑ_{SA} stands for the divergence in the SA given as FWHM value. The detailed optical design was performed using the propagation tools for Gaussian bundles of the commercial Software *ZEMAX*[®] which is based on the transformation equations [Eqs. (2.8),(2.10), and (2.11)] which derive from scalar wave theory (Sec. 2.3). The layout of the channels of the cMLA has to make sure that the entire spectrum of object waist resulting from the manufacturing tolerances can be imaged within the tolerance of the divergence. Consequently, there must be an overlap of the related object waists for the different channels. Seven different channels are requested only to meet the requirements. Thus, a completely numerical optimization can be performed time efficiently. Table 4.2 shows a listing of the key values of the different channels. Each channel design was optimized for a certain object waist in order to generate the desired line geometry where adjacent channels have a difference in waist radius of $0.238\mu m$. The tolerance of the divergence can be met by a small axial translation of the positive lens of the telescope for object waists close to the design value. The range of the object waist which will meet the specifications of the system for each channel is given in the last column of Tab. 4.2. The beam width in the working distance is constantly $700\mu m$.

Figure 4.2 displays a plot of the divergence as a function of the object waist for the different channels. The horizontal bars indicate the range of object waist of each channel which will meet the systems specification. The ranges of the single channels overlap in order to avoid gaps.

Conclusions The use of a cMLA allows the selection of a best suited cell e.g. in order to compensate fabrication tolerances of optical components. However, they are applicable only if a non-continuous variation is sufficient since the lens parameters of the adjacent cells in the cMLA need to have finite differences. The use of a cMLA was possible since the divergence was allowed to have a comparably wide tolerance band. The mechanical integration of such a system can be rather simple (Fig. 4.1). Here, the cMLA is positioned vertically for the channel

Table 4.2: Design data and application range of a cMLA of concave cylindrical microlenses. The exact divergence value of 0.3° can be met by the given single object waist values. The divergence is within the tolerance of $\pm 0.01^\circ$ for the object waists within the given tolerance band. The object waist ranges of adjacent channels slightly overlap.

Configuration	Object waist in μm	Focal length in mm	Magnification	Object waist range in μm
1	1.19	-1.63	6.13	1.19...1.33
2	1.43	-1.98	5.04	1.31...1.59
3	1.67	-2.35	4.26	1.50...1.88
4	1.91	-2.72	3.67	1.73...2.14
5	2.15	-3.11	3.21	1.94...2.39
6	2.38	-3.51	2.85	2.16...2.62
7	2.62	-3.92	2.55	2.36...2.62

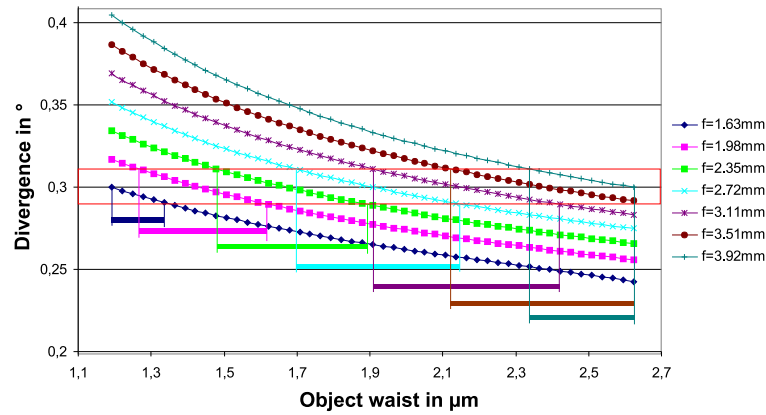


Figure 4.2: Diagram of the divergence of the Gaussian beam in the SA of the laser diode as a function of the object waist for 7 cells of the cMLA with different focal lengths. Horizontal bars indicate the range of object waists where the tolerance can be met. Adjacent ranges overlap in order to avoid gaps.

selection and the lens of positive power is translated horizontally in order to adjust the beam parameters which have to be monitored during the assembly. The easy integration along with the potential to avoid the selection of the laser diode according to the SA divergence lead to a cost efficient fabrication of the system.

4.1.2 Reduction of number of components

Another field of application of cMLAs that is associated with the improvement of integration is to reduce the number of optical components of a system. This reduction of the number of components is connected with less effort in the fabrication process and in the assembly consequently decreasing the overall fabrication costs. As an example, again a fly's eye condenser system used for beam homogenization is discussed with specification according to Tab. 4.3. As explained in Sec. 2.4, the setup usually consists of two identical rMLA where the second

one is placed in the focal plane of the first microlenses and a Fourier lens (Fig. 4.3, left). The latter is required for superimposing the radiation transmitted by the different channels in order to achieve steep edges at the margins of the intensity distribution. The Fourier lens can be eliminated in the setup, if the microlenses of the second array of each channel are used for the deflection of the beam.⁸⁸ This can easily be accomplished by a channel-wise adaptation of the center position of the microlenses (Fig. 4.3, right). The decenter depends on the focal length of the microlenses, the distance of the considered channel with respect to the optical axis of the system, and the distance between the second microlens array and the plane where the top hat distribution is supposed to be located. Hence, the cMLA effectively integrates the function of the rMLA and of the Fourier lens. As an advantage of using a cMLA compared to setups using two regular arrays whereas the pitch of the second one is smaller than that of the first, the NA of the input radiation can be as big as the NA of the lenses.

Optical design In the prototyped system the radiation of a laser diode has to be transformed into a line focus laying in the direction of the FA of the singlemode laser diode. Thus, cylindrical lenses are used since homogenization is required in one dimension only. The Gaussian intensity distribution in the SA-direction can remain unchanged. As explained in Sec. 2.4, about 5 channels are required in order to homogenize a Gaussian input beam into a line focus with a maximum deviation of the intensity of about 5% with respect to the mean value. On the other hand, the pitch p of the microlenses should be chosen as large as possible to make the distance between the intensity peaks in the far field as small as possible which is due to the coherent interaction of the single channels [Eq. (2.23)]. An array of eleven lenses with a pitch of $600\mu\text{m}$ was chosen as a trade-off. According to Eq. (2.33), half the width of the line focus equals the product of the NA of the microlenses and the focal length of the Fourier lens. Microlenses with a NA of approximately 0.03 have to be used for a given focal length of the Fourier lens of 80mm. Consequently, the first MLA being regular consists of 11 lenses with a focal length of 10mm according to Eqs. (2.28) and (2.29). The array consists of 6 differently shaped cells whereas the remaining cells are simply mirrored along the optical axis due to the symmetry of the system. The very low number of cells enables the time efficient numerical optimization of the cMLA which was done using the ray tracing software *ZEMAX*[®].

Various ways exist to model the surface of the decentered cylindrical lens. One is the so called polynomial surface where the surface profile is given by a polynomial which follows

$$z(x, y) = \sum_{o=1}^{\kappa} A_o E_o. \quad (4.2)$$

Here, A_o stands for the polynomial coefficients, E_o for a specific polynomial term, and κ for the number of requested polynomial terms.⁹⁴ Two polynomials [$E_1 = x/R_{norm}$ and $E_2 = (x/R_{norm})^2$] are necessary only for modeling the required surface profile. The position coordinates are normalized to R_{norm} which is referred to as normalization radius. As

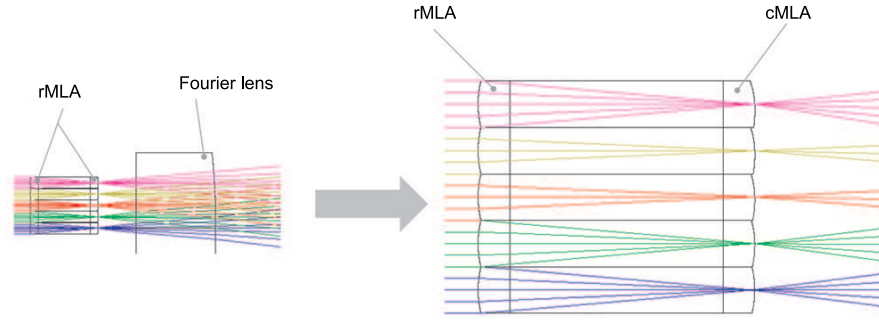


Figure 4.3: *Left:* Schematic drawing of the classical setup using a regular tandem microlens array and a Fourier lens. *Right:* Schematic drawing of the system using a tandem lens array consisting of a regular and a chirped array. Here, no Fourier lens is required.

Table 4.3: Component and system specifications of the line focus generating optical system using a cMLA for the reduction of the number of optical components.

Feature	Value
Laser diode	Hitachi HL6320
Working distance measured from facet of laser diode	103mm
Length of line focus (FA-direction)	4.8mm
Width of line focus ($1/e^2$) (SA-direction)	$70\mu m$
Homogeneity	5%

in the previous example, the direction of homogenization coincides with the FA of the laser diode and can be treated completely independent of the SA direction since cylindrical lenses are solely used except for the asphere placed in front of the laser diode used for collimation. The lenses of the second MLA have to deflect the ray bundles that way, that the chief rays of all channels coincide at the optical axis of the system. The marginal rays of all channels have to coincide at the upper and lower edge of the line focus, respectively, in order to achieve steep edges at the margins of the intensity distribution. These conditions were added to the merit function of the ray tracing software and the optimization was carried out. In Tab. 4.4 the coefficients describing the profiles of the lenses are given. The missing five lenses have parameters like lenses 2 to 6 except for the sign of the coefficient A_1 being negative which is due to the symmetry of the system. The second lenses are illuminated in the central parts only since the divergence of the radiation after the collimation asphere is very small. Therefore, it is possible to decrease their widths without any influence on the optical performance. This leads to smaller vertex heights of the lenses which is beneficial to their fabrication. The widths of the lenses of the second array were set to $360\mu m$ whereas the pitch of $600\mu m$ remained. An additional offset term has to be added in the declaration of the surfaces in order

Table 4.4: Coefficients of polynomial surfaces. Normalization radius $R_{norm}=100\text{mm}$.

Lens number	A_1	A_2	Offset in μm
1	0	1080	22.50
2	1.4426	1080	22.02
3	2.8845	1080	20.57
4	4.3249	1080	18.24
5	5.7613	1080	15.73
6	7.2043	1080	13.20

to equalize the vertices of all lenses which is necessary because of the definition of the surface in *ZEMAX*[®].⁹⁴

Prototyping of the cMLA A direct writing method has to be used since the single microlenses have a non-symmetric shape. The cMLA consists of microlenses with a maximum sag height of $22.5\mu\text{m}$ (see Tab. 4.4, offset of lens 1) permitting the use of laser lithography as fabrication method. The developed software tools (Sec. 3.4.2) were used to generate the data for the fabrication of the cMLA. In Fig. 4.4 a plot of the fabricated structure is given. Relatively large deviations of the fabricated structure to the designed one was observed which led to bigger curvatures and consequently shorter focal lengths of the lenses of the cMLA. These are due to diffraction effects of the writing beam which have a strong impact when writing structures with comparatively large vertex heights. Additionally, a systematic mismatch between the intensity calibration used in the data preparation and the one used during fabrication was observed after the processing which was due to an unrecognized misalignment of the machine. Unfortunately a second fabrication run with optimized parameters was not possible.

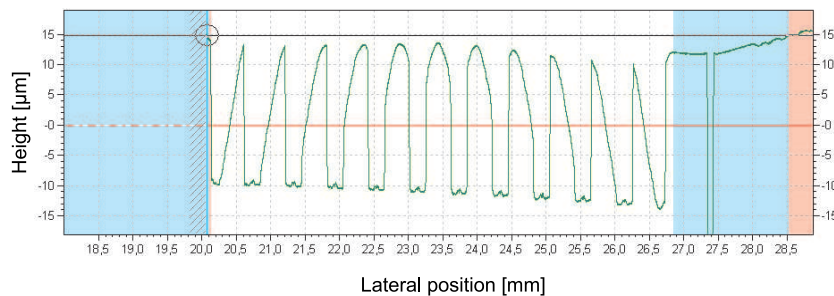


Figure 4.4: Height profile of the cMLA measured with a tactile surface profiler. The center parts of the lenses are used only since the divergence of the input beam is limited. Therefore, larger dead zones between the lenses could be allowed. This leads to smaller vertex heights and consequently easier fabrication by laser lithography.

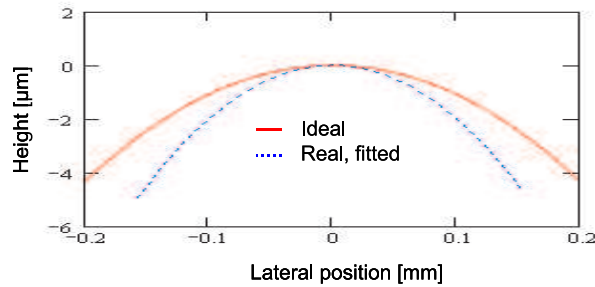


Figure 4.5: Ideal and parabolically fitted height profile of the lens in the center of the cMLA.

In Fig. 4.5 a plot of the ideal and a fitted surface profile of the center lens (no decenter required) is given. The fabricated lenses have a focal length of about 5mm instead of the design value of 10.4mm. Geometrical optical aspects have been considered for the definition of the length of the line focus so far. The interaction of the single beamlets in the plane where they are superimposed was neglected up to this point. In order to examine the wave optical interference effects, the design as well as the measured values were used as input to a wave optical simulation of the fly's eye condenser using the software tool *Virtual LabTM 3.1*.⁹⁵ Figure 4.6 shows the wave optical simulation results of the different types of fly's eye condensers. A top hat intensity distribution can be generated which is modulated by equidistantly sharp intensity peaks caused by the periodic structure of the rMLA [Fig. 4.6(a)] when using the classical system containing the rMLA. Almost the same far field distribution can be obtained when using the ideal cMLA as second lens array. The system without the Fourier lens leads to the same result though using fewer components [Fig. 4.6(b)]. The simulation of the fly's eye condenser using the fabricated cMLA indicates that no sharp top hat intensity distribution can be created which is due to the mismatched focal lengths of the second arrays. Broadened shoulders appear at the margins of the line focus with twofold reasons [Fig. 4.6(c)]. Firstly, the second lenses do not realize a plane phase distribution which is necessary for obtaining a top hat envelope of the intensity distribution according to Eq. (2.32). Secondly, the deflection angle of each beamlet depends on the focal length of the second lenses and their decenter. Larger deflection angles result caused by the shorter focal lengths of the lenses of the prototyped array. Consequently, the bundles transmitted by each channel will not superimpose accurately at the requested working plane which leads to washed out margins of the line focus.

Experimental results A prototype of a line focus generator including the laser diode mounted on an actively cooled heat sink was built up (Fig. 4.7). The far field intensity distribution was captured using a beam profiler camera system (*Coherent[®] LaserCamTM IIID¹³⁷*) and is given in Fig. 4.8. The grating interferences leading to the equidistant intensity peaks as well as the limited slope angle of the envelope of the intensity distribution at the margins can be observed and are in good agreement with the simulated distribution.

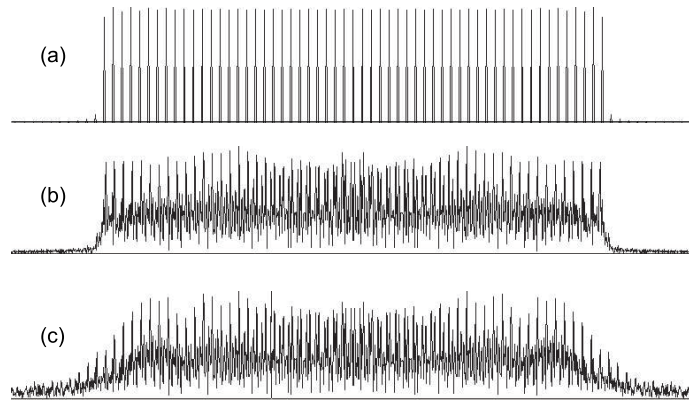


Figure 4.6: Calculated far field intensity distributions. (a) Using a classical setup consisting of a regular tandem array and a Fourier lens. Peak distance is approximately $85\mu\text{m}$ and line length 4.8mm. (b) Using a setup containing a tandem array which consists of a regular and a chirped array with design parameters. (c) Using a setup containing a tandem array which consists of a regular and a chirped array with measured parameters.

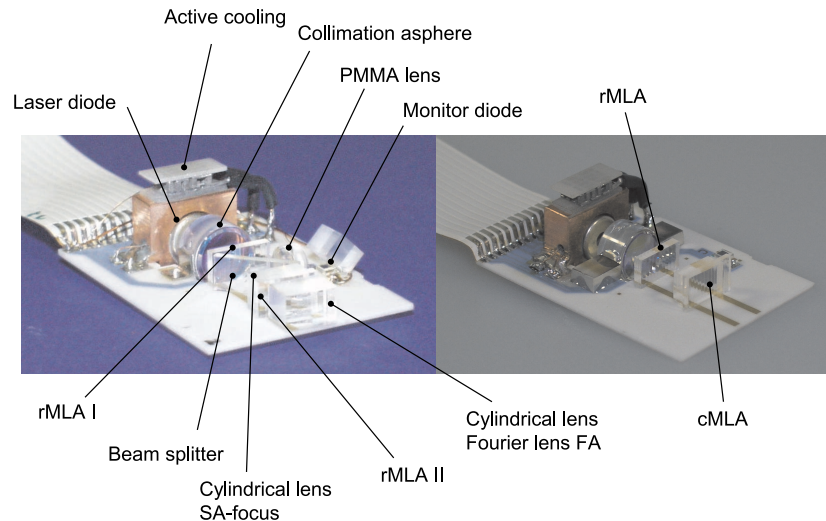


Figure 4.7: Photograph of assembled beam shaping optical systems including a laser diode mounted on an actively cooled heat sink. *Left:* classical system consisting of two identical cylindrical rMLAs and a Fourier lens. *Right:* System using a cMLA of channel-wise decentered cylindrical microlenses as second array for the elimination of the Fourier lens.

Combined integration A design combining the use of cMLAs for the selection of the best suited cell and the reduction of the number of components was elaborated as a third system (Fig. 4.9). This beam shaping optics summarizes the presented design proposals of the use of cMLAs for improved integration. Firstly, an anamorphic telescope is used in the SA of a laser diode in order to compensate varying divergences due to fabrication tolerances (Sec. 4.1.1). Secondly, the above explained cMLA of channel-wise decentered cylindrical microlenses is used for the elimination of the Fourier lens.

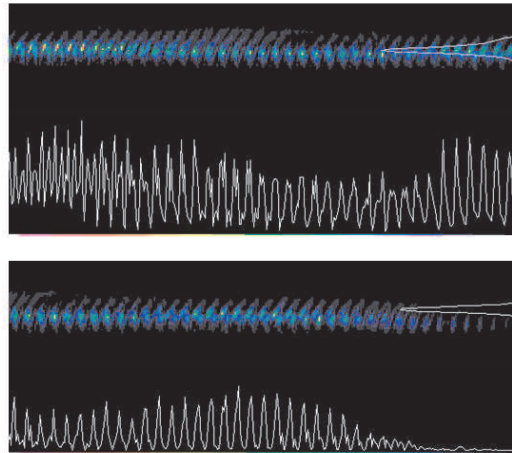


Figure 4.8: Measured far field intensity distribution using the fabricated cMLA. A complete picture of the entire line could not be capture due to the small entrance aperture of the camera. *Top*: Center of line focus. *Bottom*: Margin of line focus. Peak distance is approximately $85\mu\text{m}$.

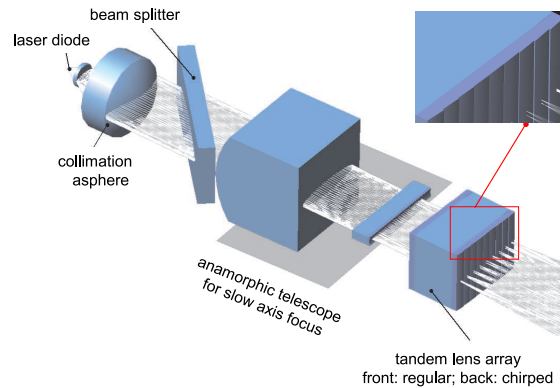


Figure 4.9: Rendered drawing of a beam homogenizing setup based on a fly's eye condenser using regular and chirped cylindrical MLAs. Additionally, a cylindrical lens telescope with adjustable magnification in the SA of the laser diode is implemented for tuning the divergence of the Gaussian beam in direction of the SA (Sec. 4.1.1).

Conclusions The use of cMLAs for the selection of the best suited cell is the most trivial field of application. The array design is especially simple since the channels of the array do not interact in any not even a geometrical way. The cells are formed as an array and placed on a common substrate for the economy of the handling and fabrication only. However, they are of important practical relevance since they allow to e.g. compensate ubiquitous component tolerances in a very easy and cost efficient manner. Usually, the lenses require small space compared to the size of their carrier which is limited in miniaturization due to handling and assembly reasons. Therefore, it is possible to place more lens elements on a substrate without a significant increase of its size. A system for the elimination of a Fourier lens in a fly's eye homogenizer was presented as a further step ahead in the complexity of the design of a cMLA. Here, geometrical considerations of the system influence the cMLA while the actual design of each cell can be done without taking notice of the other channels.

4.2 cMLA for optimization of optical performance

Two examples for the use of cMLAs for the optimization of the optical function of an optical system are presented in this section. The first is an artificial apposition compound eye camera where the chirped array is used to eliminate aberrations occurring under oblique incidence. Here, the optical layout of the array is done by a completely analytical derivation of the describing functions and reflow of photoresist is used as fabrication technique. Due to the limitations of this fabrication method, ellipsoidal microlenses are employed which can be considered as the most complex surface geometry for a lens manufactured by this technique. The second example is a planar integrated free-space optical interconnect which uses off-axis lens segments as cells of the cMLA. The array is designed to eliminate spherical aberrations introduced by macroscopic imaging components. Laser lithography as a direct writing fabrication method was chosen for the generation of the master structure due to the required asymmetric shape of the microlenses. The lens parameters in this example were obtained using the combined numerical/analytical approach based on significant numerically optimized cells of the array and fitted functions. The two example applications combine different ways for both, the computation of the lens parameters and the fabrication technique used.

4.2.1 cMLA of ellipsoidal microlenses

Each optical channel of an artificial apposition compound eye objective uses a single lens of positive power for the imaging. The individual lenses of the array are dedicated to varying field angles (Sec. 2.2). Off-axis aberrations occur in case of spherical lenses when used under oblique incidence. This leads to a decreased resolution with increasing field angle and consequently limits the FOV of the camera to about 25° when using lenses with a f-number of approximately 2.3 as in state-of-the-art systems. Therefore, the fields of application of this novel type of an image acquiring optical device are quite restricted. Thus, the goal of the design of an adequate cMLA for the artificial apposition compound eye camera is the elimination of the off-axis aberrations in order to improve the resolution versus the field. Since the resolution of the camera is in indirect proportion to the acceptance angle of the channels, the versatility of the device upgrades in two aspects: Firstly, the FOV can be enhanced which is necessary to make the system compliant to specifications of industrial application scenarios. Secondly, more channels can be used by increasing the FOV leading to an improved resolution in terms of number of pixels while the angular resolution of each channel remains constant.

Correction of astigmatism and field curvature Classical camera lenses transmit the entire FOV through a single aperture. In contrast, in an apposition compound eye each channel has to image a very small part of the entire FOV only. This enables the efficient compensation of the off-axis aberrations by a single optical surface. The basic idea is to use an adapted anamorphic lens having two different radii of curvature and thus two focal lengths in perpendicular directions to compensate the effects of astigmatism and field curvature for

a specific angle of incidence. Each lens will have a slightly different appearance since it is dedicated to a different chief ray angle. Consequently, a cMLA of adapted anamorphic microlenses results. The positions of the tangential and sagittal focus can be determined using the Gullstrand's equations [Eqs. (2.4) and (2.5)]. Here, the tangential and the sagittal BFLs $s'_{t,i,j}$ and $s'_{s,i,j}$ can be calculated as a function of the chief ray angle $\sigma_{i,j}$. The indices i, j indicate the channel coordinates within the considered array. Astigmatism for a specific angle of incidence is eliminated if the BFLs for tangential and sagittal rays coincide. By demanding

$$s'_{t,i,j} = s'_{s,i,j} = \frac{s'_0}{\cos \sigma'_{i,j}}, \quad (4.3)$$

the tangential and sagittal image planes are fixed at the position of the Gaussian image plane (see Figs. 2.2 and 2.3). Since $s'_{t,i,j}$ and $s'_{s,i,j}$ are measured along the direction of the chief ray, their projection onto the optical axis has to be taken into account to find the position of the tangential and sagittal image planes and their distances to the Gaussian image plane. The latter is determined by the paraxial back focal length s'_0 . A planarized moiré image results for the compound eye imaging system.^{138–140} Inserting the Gullstrand's equations into Eq. (4.3), the tangential and sagittal radii of curvature of the lens for correction of astigmatism and field curvature can be calculated by

$$R_{t,i,j} = s'_0 \left(\frac{n' \cos \sigma'_{i,j} - n \cos \sigma_{i,j}}{n' \cos^3 \sigma'_{i,j}} \right) \quad \text{and} \quad (4.4)$$

$$R_{s,i,j} = s'_0 \left(1 - \frac{n \cos \sigma_{i,j}}{n' \cos \sigma'_{i,j}} \right). \quad (4.5)$$

Here, infinitely distant objects are assumed. Figure 4.10 provides a visualization of the nomenclature used in the Gullstrand's equations.

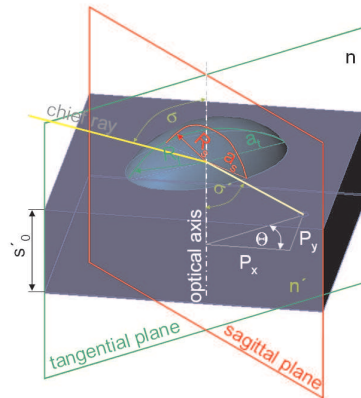


Figure 4.10: Geometrical parameters of an ellipsoidal lens for explanation of the notation in Gullstrand's equations. n, n' — index of refraction in object and image space, respectively; σ, σ' — chief ray angle in object and image space, respectively; s'_0 — paraxial back focal length; R_t — radius of curvature in tangential plane; R_s — radius of curvature in sagittal plane; a_t — axis of ellipsoidal at rim of lens laying in the tangential plane; a_s — axis of ellipsoidal at rim of lens laying in the sagittal plane.

In Fig. 4.11 a plot of the calculated optimum tangential and sagittal radii of curvature as a function of the chief ray angle is given for a spherical lens with a paraxial focal length of $145\mu\text{m}$. Additionally, the same lens was implemented as “Biconic” surface in the ray tracing software *ZEMAX*[®] and optimized for the same angles of incidence for validation of the analytical results.⁹⁴ The obtained radii are marked as circles and boxes in Fig. 4.11.

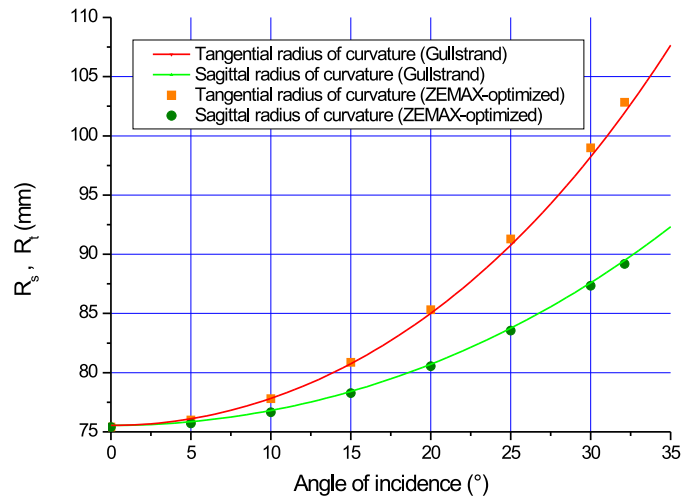


Figure 4.11: Optimum tangential and sagittal radii of curvature under oblique incidence calculated by Gullstrand’s equations (lines) and using ray tracing optimization (boxes and circles, respectively). Paraxial focal length is $145\mu\text{m}$, NA is 0.23.

Significant deviations between numerically optimized and analytic values can be observed for large chief ray angles only. These deviations result from aberrations other than 3^{rd} order astigmatism to which the Gullstrand’s equations are limited. In contrast, numerical optimization routines account for all influences on the spot size like coma and spherical aberrations and lead to slightly different results.

Yet another access to understand how anamorphic lenses accomplish the correction of astigmatism and field curvature due to the oblique incidence can be obtained by a detailed look at the resulting image positions for the tangential and the sagittal ray fans as a function of the chief ray angle. In Fig. 4.12 a plot of the tangential and sagittal BFLs for a spherical and an adapted anamorphic lens are given as a function of the lateral spot position in the image plane. The well-known image shells result which touch each other and the paraxial image plane under perpendicular incidence (point A) in case of the spherical lens. The tangential and sagittal image shells of the anamorphic lens are separated under perpendicular incidence since the lens has different radii of curvature in different planes. However, when used under the designed angle of incidence both shells intersect (= correction of astigmatism) which can be chosen to happen in the paraxial image plane (= correction of field curvature at the artificial apposition eye objective)(point B).

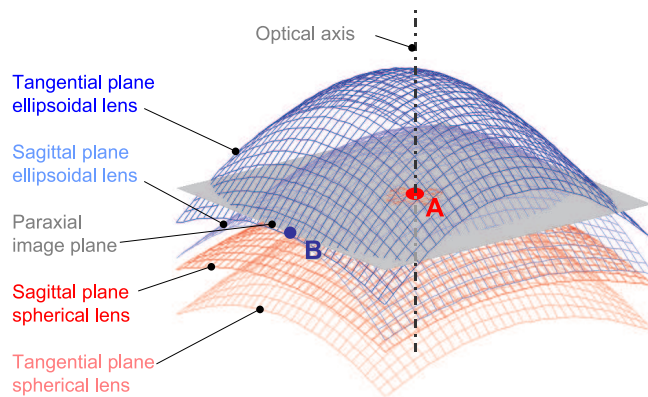


Figure 4.12: Simulation results of the tangential and sagittal BFLs for a spherical and an anamorphic microlens as a function of the lateral spot position resulting in the tangential and sagittal image shells. A - Tangential and sagittal image shells and paraxial image plane touch each other on the optical axis for a spherical lens illuminated under perpendicular incidence. B - The tangential, sagittal, and paraxial image positions coincide for the design angle in case of an adapted anamorphic lens. Radius of curvature of the spherical lens $R=74.5\mu\text{m}$, tangential and sagittal radii of curvature of the anamorphic lens $R_t=103.3\mu\text{m}$ and $R_s=89.6\mu\text{m}$, angle of incidence 32.2° , material *Ormocer*[®].

Ellipsoidal microlenses by melting of photoresist Diffraction limited imaging performance is requested for all channels of the artificial apposition compound eye camera in order to achieve small acceptance angles. Therefore, a fabrication technique for the cMLA has to be chosen which is capable of producing smooth and well defined surfaces. Reflow of photoresist is a well established technology for the fabrication of high quality spherical surfaces. In addition, the process can be used to produce the required anamorphic microlenses. These ellipsoidal lenses are one attractive type of anamorphic lenses because of having two separate paraxial radii of curvature and their ability of being produced by the reflow technology if the rim of the resist cylinder has an ellipsoidal shape.¹⁴¹ In Fig. 4.13 the surface deviation of an ellipsoidal lens and a torus segment having the same paraxial radii of curvature is plotted. The peak to valley deviation for the given values of radii of curvature - which are typical for the considered microlenses - are less than $\lambda/14$ and thus can be neglected. Therefore, ellipsoidal lenses are an appropriate approach to the desired anamorphic lenses. The resulting

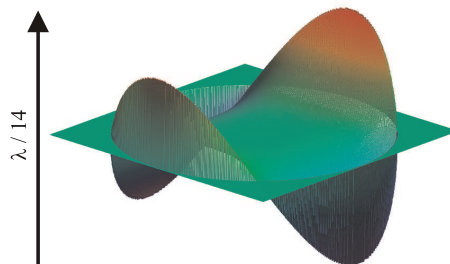


Figure 4.13: Surface deviation between torus segment and ellipsoidal lens with identical principal radii of curvature $R_t = 485.7\mu\text{m}$ and $R_s = 609.6\mu\text{m}$, lens height $20.2\mu\text{m}$ and conical constants in the tangential and sagittal plane, respectively, for representation of the ellipsoidal lens $k_t = -0.096$ and $k_s = 0.134$. For the representation of the torus segment $k_s = k_t = 0$ is set.

minimum surface after the melting process of a resist cylinder with an ellipsoidal rim cannot be modeled analytically. However, a numerical modeling can be derived when the surface is approximated by a portion of a rotationally symmetric ellipsoid.¹⁴¹ To verify this assumption, a surface generated by numerical iterative surface minimization with the constraints of volume conservation and the conservation of the resist boundary¹⁴² was compared with the results of the numerical parametric model for the same starting parameters of the resist cylinder. Figure 4.14(c) shows the height difference between the expected ideal ellipsoidal lens and the computer iterated surface. Both surfaces match very well with a maximum peak to valley deviation of $\lambda/7$. The deviations occurring along the rim of the lens are due to the effect of coarse sampling during simulation. In the reflow fabrication technique, the resulting shape

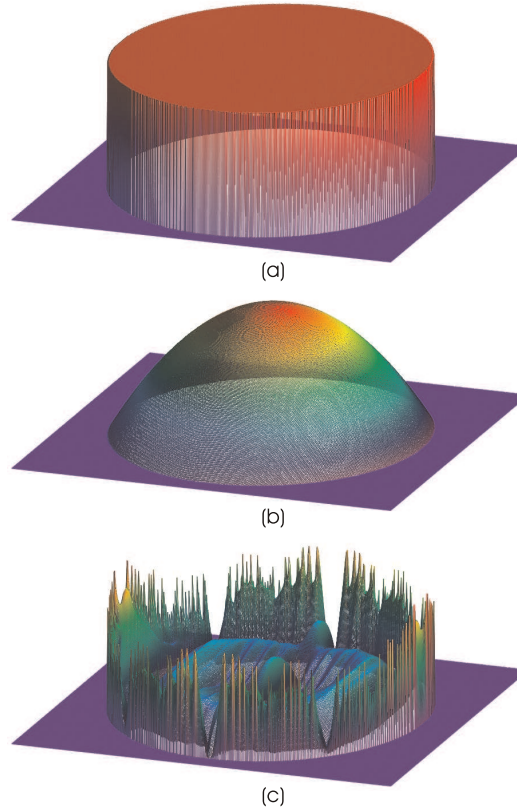


Figure 4.14: (a) Resist cylinder on an ellipsoidal basis to be melted, height: $10.18\mu\text{m}$, lens bases: $a_t = 138.9\mu\text{m}$, $a_s = 155.6\mu\text{m}$; (b) Computer simulated surface by iterative melting of the elliptical resist cylinder, lens height: $20.3\mu\text{m}$; (c) Surface deviation (peak to valley) of ideal ellipsoidal lens and iterated surface is maximum $\lambda/7$ and thus diffraction limited.

of the structure depends on the geometry of the rim and the height of the cylinder to be melted. Therefore, the dependence of the radii of curvature on the major and minor axes a_t and a_s of the ellipsoidal base is requested for mask generation. The principal curvatures of the ellipsoidal lens in the tangential and sagittal plane, respectively, are given by

$$R_{t/s} = \frac{h_L}{2} + \frac{a_{t/s}^2}{2h_L}, \quad (4.6)$$

where h_L is the vertex height of the lens. Equation (4.6) gives the context between the radii of curvature in the tangential and sagittal plane and the major and minor axes of the rim of the lens. The calculation of the rim data necessary for creating the mask for structuring the photoresist is possible since the radii of curvature are given by Eqs. (4.4) and (4.5). The major and minor axes of each cell must follow

$$\frac{R_{t_{i,j}}}{R_{s_{i,j}}} = \frac{a_{t_{i,j}}^2 + h_L^2}{a_{s_{i,j}}^2 + h_L^2}, \quad (4.7)$$

in order to ensure astigmatic correction. Additionally, one has to ensure that the relation

$$\frac{R_{t/s_{i,j}}}{R_{t/s_{ref}}} = \frac{a_{t/s_{i,j}}^2 + h_L^2}{a_{t/s_{ref}}^2 + h_L^2}, \quad (4.8)$$

is valid for all cells of the array in order to make sure that all spots are located at the same image plane. A constant vertex height h_L is assumed for all cells of the array. This assumption has to be checked after the fabrication and is given in the following paragraph. $R_{t_{ref}}$ and $R_{s_{ref}}$ are the radii of curvature of the reference cell which in the proposed design complies to the cell with index (0,0). Since it is a spherical lens (perpendicular incidence) the radii of curvature are equal ($R_{t_{ref}}=R_{s_{ref}}=R$). Thus, the rim of this lens is a circle leading to $a_{t_{ref}}=a_{s_{ref}}=r_{ref}$ as the radius of the lens aperture. Using Eqs. (4.7) and (4.8) the major and minor axes of each cell of the array can be calculated by

$$a_{t_{i,j}} = \sqrt{r_{ref}^2 \frac{R_{t_{i,j}}}{R_{t_{ref}}} + h_L^2 \left(\frac{R_{t_{i,j}}}{R_{t_{ref}}} - 1 \right)} \quad \text{and} \quad (4.9)$$

$$a_{s_{i,j}} = \sqrt{\left[r_{ref}^2 + h_L^2 \left(1 - \frac{R_{t_{ref}}}{R_{s_{ref}}} \right) \right] \frac{R_{s_{i,j}}}{R_{t_{ref}}} + h_L^2 \left(\frac{R_{s_{i,j}}}{R_{s_{ref}}} - 1 \right)}. \quad (4.10)$$

Since the radii of curvature of all lenses are already known using Eqs. (4.4) and (4.5), the shape of the ellipsoidal rims of the cells can be calculated for a given aperture radius r_{ref} of the spherical reference lens located in the cell of index (0,0).

Derivation of the analytical functions In order to describe an ellipsoidal lens completely, five parameters and thus five describing functions are necessary: the two radii of curvature (tangential and sagittal plane), the coordinates of the vertex position (x and y), and the orientation angle of the main axes with respect to the reference cell. The first two result from the conditions for the correction of astigmatism and field curvature and are given by Eqs. (4.4) and (4.5). These depend on the chief ray angle $\sigma_{i,j}$ which is transferred by a cell with index (i,j) of the artificial apposition compound eye objective (Fig. 2.3). One quarter of an entire symmetric FOV is considered only in the prototyped design. The other cells necessary for capturing the full FOV are simply mirrored images of the considered quarter. Therefore,

the reference cell has the index (0,0) and corresponds to the cell assigned to the chief ray angle of 0° which coincides with the optical axis of the entire objective. In order to obtain an undistorted image

$$\frac{\tan \sigma_{max_x}}{\tan \sigma_{max_y}} = \frac{(N_x - 1) a_x}{(N_y - 1) a_y}, \tag{4.11}$$

must be valid, where N_x and N_y are the number of channels in the x- and the y-direction and a_x/a_y is the distance of adjacent resolvable points in the object plane in x- and y-direction (Figs. 4.15 and 4.16). Quadratic object pixels are considered in the designed prototype.

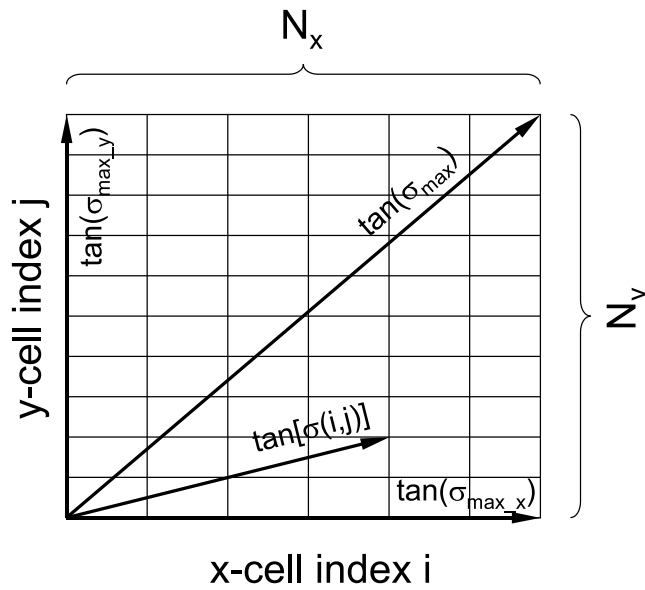


Figure 4.15: Sketch of the segmented object plane according to the number of channels of the camera for the explanation of the field angles.

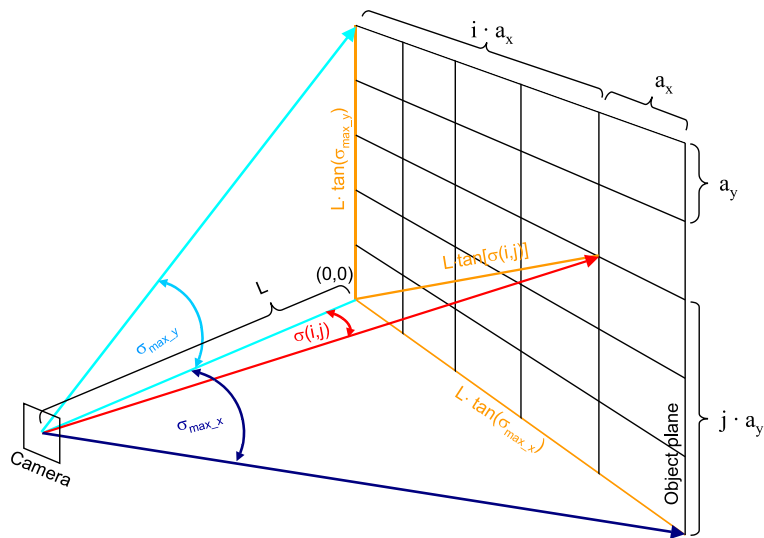


Figure 4.16: Sketch for the explanation of the field angles in the object space.

Therefore, a_x equals a_y . Usually the field angles are defined in terms of the maximum angle across the diagonal and the aspect ratio of the horizontal (x) and vertical (y) size of the image. Consequently, the maximum field angle is

$$\tan \sigma_{max} = \sqrt{\tan^2 \sigma_{max_x} + \tan^2 \sigma_{max_y}}, \quad (4.12)$$

and the maximum horizontal and vertical field angles can be written as

$$\tan \sigma_{max_x/y} = \tan \sigma_{max} \cdot \left[1 + \left(\frac{N_{y/x} - 1}{N_{x/y} - 1} \right)^2 \right]^{-1/2}. \quad (4.13)$$

On the other hand, the maximum horizontal and vertical field angles can be calculated by

$$\tan \sigma_{max_x/y} = \frac{a_{x/y}}{L} (N_{x/y} - 1), \quad (4.14)$$

with L as the distance from to object to the camera. The chief ray angle of the cell with index (i,j) is given by

$$\tan \sigma_{i,j} = \frac{1}{L} \sqrt{(a_x i)^2 + (a_y j)^2}. \quad (4.15)$$

Combining Eqs. (4.13) and (4.14) for both, the maximum horizontal and vertical field into Eq. (4.15) yields

$$\tan \sigma_{i,j} = \tan \sigma_{max} \sqrt{\frac{i^2}{\left[1 + \left(\frac{N_y - 1}{N_x - 1} \right)^2 \right] (N_x - 1)^2} + \frac{j^2}{\left[1 + \left(\frac{N_x - 1}{N_y - 1} \right)^2 \right] (N_y - 1)^2}}. \quad (4.16)$$

A rotational symmetric field with $N_x = N_y = N$ is assumed in the prototype. Therefore, Eq.(4.16) reduces to

$$\tan \sigma_{i,j} = \frac{\tan \sigma_{max}}{\sqrt{2}(N - 1)} \sqrt{i^2 + j^2}. \quad (4.17)$$

The chief ray angle $\sigma'_{i,j}$ behind the lens within the substrate material with index n' is given by Snell's law

$$n \cdot \sin \sigma_{i,j} = n' \cdot \sin \sigma'_{i,j}. \quad (4.18)$$

The position where the chief ray hits the detector plane must coincide with the center of the assigned photo receptor. Therefore

$$\tan \sigma'_{i,j} = \frac{P_{i,j}}{f \cdot n'}, \quad (4.19)$$

must be valid with $P_{i,j}$ as the decenter of the receptor center with respect to the lens vertex of cell (i,j) and f is the paraxial focal length in air which is constant for all cells in order to

achieve a plane image. Inserting Eq. (4.18) into Eq. (4.19) yields

$$P_{i,j} = n' \cdot f \cdot \tan \left[\arcsin \left(\frac{n}{n'} \cdot \sin \sigma_{i,j} \right) \right], \quad (4.20)$$

which gives the amount of displacement as a function of the object space chief ray angle $\sigma_{i,j}$. The calculation of the orientation angle can be done by simple vector analysis. When considering an anamorphic lens where the normals of the planes containing the radii of curvature are collinear to the Cartesian coordinate system, the normal of the tangential plane \vec{n} can be written as

$$\vec{n} = \begin{pmatrix} n_x \\ 0 \end{pmatrix}. \quad (4.21)$$

The chief ray angle of a certain cell is determined by the displacement of the pinhole center with respect to the lens vertex and the orientation angle only. Therefore, it is possible to arrange the lens vertices on a regular grid and allow the pinhole positions to be chirped or vice versa. The lens vertices are arranged on a regular grid with the pitch p in x- and y-direction in this prototype. Thus, the displacement vectors of the vertices of the lenses with respect to the reference cell located at the origin are given by

$$\vec{p}_{i,j} = p \begin{pmatrix} i \\ j \end{pmatrix}. \quad (4.22)$$

The angle between the normal and the displacement vector can be calculated by

$$\cos \Theta_{i,j} = \frac{\vec{n} \cdot \vec{p}_{i,j}}{|\vec{n}| |\vec{p}_{i,j}|}, \quad (4.23)$$

which can be simplified to

$$\cos \Theta_{i,j} = \left[1 + \left(\frac{j}{i} \right)^2 \right]^{-1/2}. \quad (4.24)$$

Each cell has to be rotated by the angle $\Theta_{i,j}$ in order to place the optical axis of the objective within the tangential plane of each anamorphic microlens. The horizontal and vertical components of the displacement vector must follow

$$\tan \Theta_{i,j} = \frac{P_{y_{i,j}}}{P_{x_{i,j}}}, \quad (4.25)$$

since the displacement vector has to be located in the tangential plane of each lens. The amount of displacement can be calculated by

$$P_{i,j} = \sqrt{P_{x_{i,j}}^2 + P_{y_{i,j}}^2}. \quad (4.26)$$

The x- and y-components of the displacement can be written as

$$P_{x_{i,j}} = P_{i,j} (1 + \tan^2 \Theta_{i,j})^{-1/2} \quad \text{and} \quad (4.27)$$

$$P_{y_{i,j}} = P_{i,j} (1 + \tan^{-2} \Theta_{i,j})^{-1/2}, \quad (4.28)$$

by combining Eqs. (4.25) and (4.26). In conclusion, three [Eqs. (4.24), (4.27), and (4.28)] out of the five functions (see begin of this section) required for the description of the array are depending on geometrical aspects and define the position of the microlenses. These considerations enable a distortion free imaging. This 3rd order aberration is especially noticeable and disturbing when imaging large FOV like in classical single aperture fish eye objectives. Distortion can easily be eliminated in artificial apposition compound eye cameras by the adaptation of the center positions of the lenses with respect to the assigned pixels. The two other functions allow for the calculation of the radii of curvature of the anamorphic ellipsoidal lenses [Eqs. (4.4) and (4.5)]. They result from the correction of astigmatism and field curvature and originate from geometric-optical aspects. All parameters of the entire array can be calculated with the number of channels in x- and y-direction N_x and N_y , the paraxial focal length f , the pitch of the regular array of lenses or the photo receptors p , the radius of the aperture of the reference cell r_{ref} , and the maximum field angle σ_{max} as parameters.

Prototyping The parameters of the cMLA were chosen in order to meet the specifications of a large-pitch CMOS imager¹⁴³ according to the parameters listed in Tab. 4.5 for the fabrication of a first prototype. Two systems having the same number of channels, paraxial focal length, and FOV were built for comparison. The first objective consists of identical spherical lenses consequently utilizing a rMLA which was optimized for perpendicular incidence. The second one uses the cMLA with ellipsoidal lenses for a channel-wise correction of astigmatism and field curvature. Both prototypes are capturing a quadrant of a symmetrical FOV with a maximum extension of 64°, since the other three quadrants are simply mirrored images of the considered area (Fig. 4.17). The objectives have 130x130 channels with a designed paraxial focal length of 145μm. The reference cell of the cMLA has the cell index (0,0) and is used under perpendicular incidence. Thus, this lens has a spherical shape with a radius of curvature of 75.5μm. The lens vertices of the cMLA are arranged on a fixed grid with a pitch p_0 of 69.5μm. As a consequence of the fixed pitch of the lenses and of the assigned pixels which is given by the CMOS imager layout, distortion is intended to be uncorrected in this first prototype and will consequently be present in the recorded images. Distortion correction will be included in future prototypes which is simply accomplished by a channel-wise adapted lens displacement as explained above. The aperture diameter $2r_{ref}$ of the reference lens was set to 59μm in order to achieve a high fill factor and to ensure that the outermost ellipsoidal lenses do not overlap. The parameters for all lenses and the data for the e-beam writing of the required mask were calculated using the developed software (Sec. 3.4.1) based on the given input specifications. The master structures were fabricated by reflow of photoresist and subsequently replicated onto the glass substrates by means of UV-replication performed in

Table 4.5: Parameters of fabricated artificial apposition compound eye objectives.

Feature	spherical lenses	ellipsoidal lenses
Array type	regular	chirped
Number of rows	130	130
Number of columns	130	130
Number of channels	16,900	16,900
pixel pitch	$68.0\mu\text{m}$	$68.0\mu\text{m}$
pixel size	$21.4 \times 21.4\mu\text{m}^2$	$21.4 \times 21.4\mu\text{m}^2$
lens pitch	$69.5\mu\text{m}$	$69.5\mu\text{m}$
lens diameter spherical lenses	$68.0\mu\text{m}$	$59.0\mu\text{m}$
maximum major axis	—	$34.0\mu\text{m}$
paraxial focal length	$145\mu\text{m}$	$145\mu\text{m}$
max. FOV	32.15°	32.15°

a specially adapted *SUSS* mask aligner.¹⁴⁴ Pinholes with diameters of $3\mu\text{m}$ were structured into an opaque Titanium layer of about 100nm thickness on the back side of the substrate before the replication process. These pinholes are located in the paraxial focal plane of the microlenses and are required for confining the photo sensitive area of the pixels since the uncovered pixels have a size of $21.4 \times 21.4\mu\text{m}^2$.¹⁴⁵ The use of the uncovered pixels would lead to very large acceptance angles of the channels and thus to a low angular resolution according to Eq. (2.3). However, the acceptance angles of adjacent channels will overlap even when using the pinholes. Consequently, there are more channels present in the array than necessary for a correct sampling of the image. Therefore, the number of resolvable line pairs over the entire FOV will be much smaller than half the number of channels which corresponds to the Nyquist criterion.

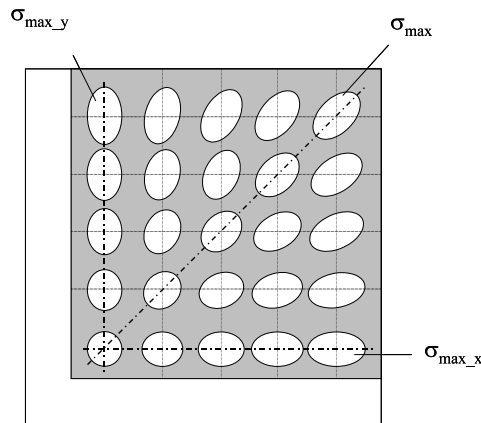


Figure 4.17: Schematic drawing of a camera chip capturing a quadrant of the full FOV. The left and bottom margins serve as docking areas for the gripping tool during assembly. The channel in the lower left corner has a perpendicular viewing direction with respect to the objective plane and consequently applies to a circular lens. The ellipticity of the corresponding lens is increased with increasing viewing angle of the channel up to $\sigma_{\max} = 32.15^\circ$ on the diagonal.

In Fig. 4.18 a sketch of the mask layout containing 25 camera objectives is given in different magnifications reaching from the complete 4-inch wafer to single ellipsoidal lenses. A wafer after the replication process but not yet diced to single objectives is pictured in Fig. 4.19. Figure 4.20(a) displays a diced artificial apposition compound eye camera objective, a 1-Euro cent coin, and a classical single aperture objective for size comparison. A completely assembled camera system, where the objective chip is mounted on the CMOS imager placed on a printed circuit board, is shown in Fig. 4.20(b).

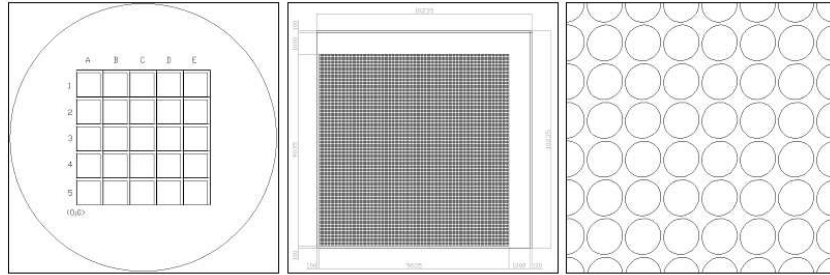


Figure 4.18: Mask layout of (a) Complete wafer with 25 camera objectives. (b) Single camera objective. (c) Detail of a region of a single camera objective showing the ellipsoidal shapes of the individual lenses.

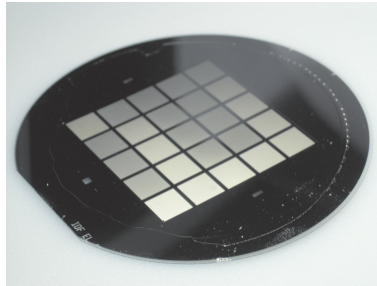
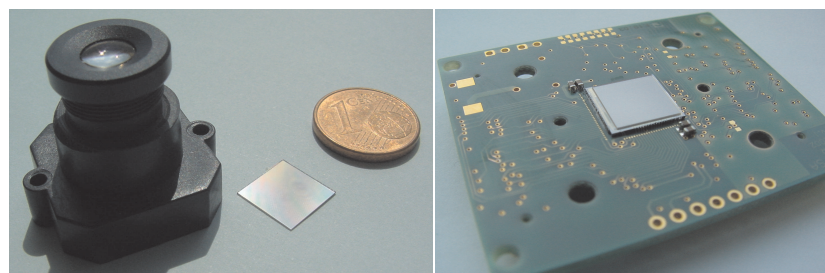


Figure 4.19: Photograph of a fabricated 4-inch wafer carrying 25 camera objectives before dicing into single objective chips.



(a)

(b)

Figure 4.20: Diced and assembled artificial apposition compound eye camera objectives. (a) Comparison to 1-Euro cent and a classical single aperture objective with the same magnification and approximate length of 20mm. (b) Attached to CMOS sensor array (courtesy of Centre Swiss d'Electronique et de Microtechnique SA (CSEM) Neuchâtel, Switzerland).

Evaluation of ellipsoidal lenses In Fig. 4.21 the analytically and the numerically calculated (*ZEMAX*[®]) as well as the measured values of the tangential and sagittal radii of curvature of the anamorphic lenses are plotted versus the chief ray angle they are designed for. For measuring the lens radii of curvature a white light interferometer (*MicroMap 512*) was used. The measurements were crosschecked with a mechanical profilometer (*Taylor Hobson Form Talysurf Series 2 PGI+¹⁴⁶*) confirming the results. The radii of curvature of the fabricated lenses are about 4% smaller than the design values which is caused by a slightly too small resist volume before the melting due to a undersized resist thickness. The measured radii of curvature of the lenses match the design values extremely well besides this off-set. The vertex heights of various microlenses of the array were measured and are plotted in Fig.

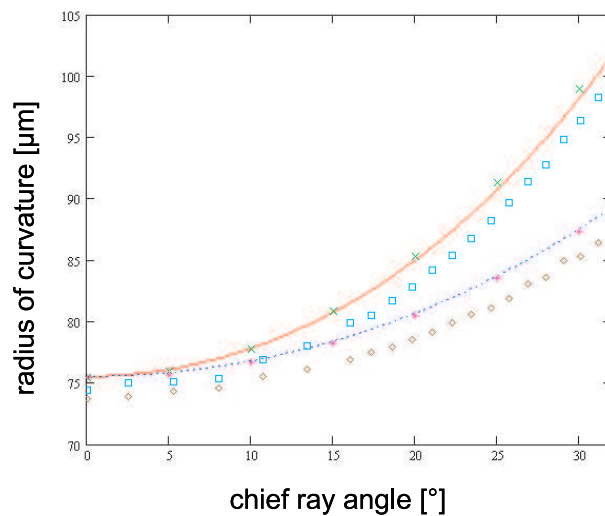


Figure 4.21: Tangential and sagittal radii of curvature as a function of the chief ray angle; *line*: tangential radius, analytically; *cross*: tangential radius, raytracing software; *boxes*: tangential radius, measured; *dotted line*: sagittal radius, analytically; *plus*: sagittal radius, raytracing software; *diamonds*: sagittal radius, measured

4.22. The assumption of constant vertex height for all cells of the array in the derivation of the describing functions of the array was testified [see Eq. (4.8)]. The measured values are in good agreement to the design value of about $5.7\mu m$.

Experimental verification of aberration correction under oblique incidence of selected single lenses

The PSFs in the focal plane of selected microlenses of the cMLA were measured when illuminated under different angles of incidence in order to verify the correction of astigmatism and field curvature under oblique incidence. A setup as drawn in Fig. 4.23 was used for the measurements. The expanded and collimated beam of a Helium-Neon laser was used for the illumination of the wafer containing the microlenses. The examined wafer had no metal layer at the backside of the artificial apposition compound eye objective. The specimen was placed on a goniometer for adjusting the angle of incidence. The resulting intensity distribution was imaged onto a CCD camera using a well-corrected microscope objective lens thus adding as small as possible aberrations. The measured intensity distribu-

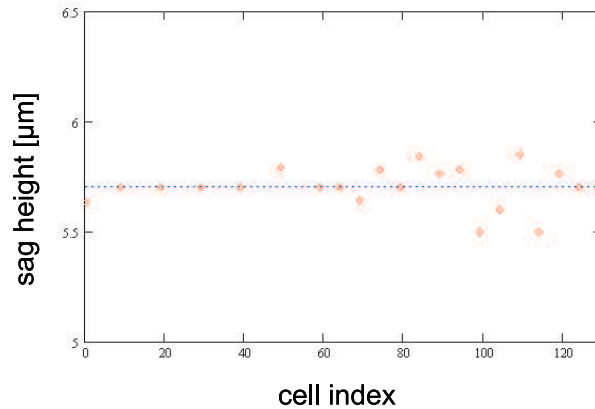


Figure 4.22: Vertex height of the microlenses as a function of the position within the array. The dotted line marks the theoretical value.

tions in the focal plane of the corresponding microlens are given in Fig. 4.24. A circular and almost diffraction limited spot is obtained when using the spherical lens [cell with index (0,0) in the array] under perpendicular incidence. The diffraction limited spot diameter of $3.5\mu m$ according to Eq. (2.2) is indicated by the circle. Astigmatism and field curvature lead to a blurred spot under oblique incidence with an angle of 32° . A large PSF results in case of the ellipsoidal lens when used under perpendicular incidence [cell with index (129,129) designed for 32° angle of incidence] due to the anamorphic structure. The tangential and sagittal focus coincide at the paraxial focal plane of the spherical lens and consequently a small spot with a diameter of about $3.6\mu m$ results when used under oblique incidence with an angle of 32° attesting almost diffraction limited performance.

Experimental verification of aberration correction under oblique incidence of the entire cMLA Images of target objects can be captured with an assembled artificial apposition compound eye camera system containing the adapted cMLA as an alternative test for verifying the correction of the off-axis aberrations. The aberration correction leads to small

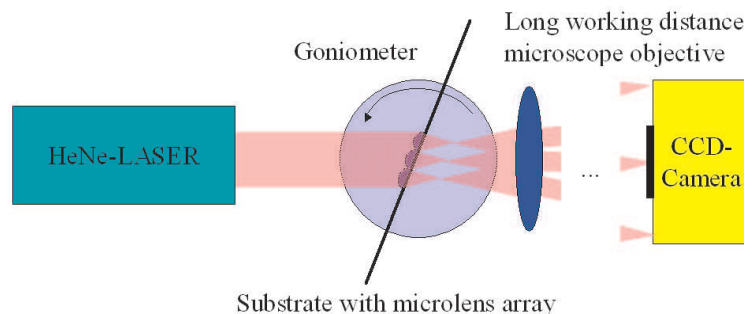


Figure 4.23: Experimental setup for the focus evaluation under oblique incidence. The rotation axis is aligned with the vertex of the microlens under test. The resolution of the measurement was determined by imaging Ronchi rulings to $0.18\mu m/\text{Pixel}$ of the CCD-chip.

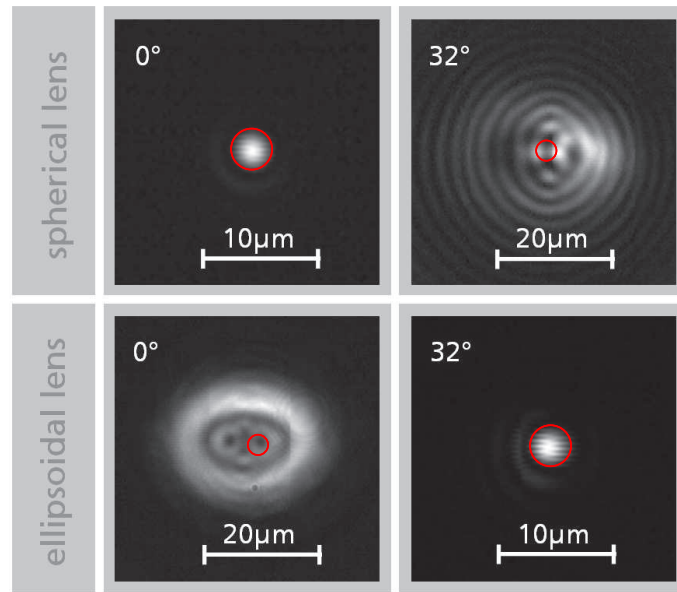


Figure 4.24: Recorded energy distributions in the image plane of the spherical lens (cell index: 0,0) of *top, left*: spherical lens under perpendicular incidence; *top, right*: same spherical lens under oblique incidence of 32° ; *bottom, left*: ellipsoidal lens (cell index: 129,129; design chief ray angle = 32°) under perpendicular incidence; *bottom, right*: same ellipsoidal lens under oblique incidence of 32° .

PSFs and consequently to a constant resolution of the camera over the entire FOV. Different representative test patterns were captured by the camera for this test. This was performed with the system using the adapted cMLA and the other based on a rMLA for comparison. Figure 4.25 and the three left columns of Fig. 4.26 show original circular and bar test targets, respectively and the corresponding images taken by compound eye objectives applying chirped or regular lens arrays. As to be expected, the resolution in the center of the FOV (lower left corner of the image, since a quarter of the entire FOV is imaged only) is independent of the use of regular or chirped lens arrays. However, with increasing viewing angle the resolution is decreased when using the simple rMLA while the resolution remains constant when applying the adapted cMLA where each channel is individually optimized for its viewing direction. As mentioned above, in this first prototype the pixels and the microlenses are positioned on regular arrays with constant pitch. Consequently, distortion is left uncorrected and still present in the captured images.

In conclusion, the designed and prototyped artificial apposition compound eye objective demonstrates the powerful use of cMLAs for the optimization of the optical function by the correction of aberrations. In this special example the utilization of a cMLA allows the enhancement of the FOV of the objectives from approximately 25° to 64° and consequently the improvement of the resolution of the camera in terms of optical channels. The use of a cMLA is elementary to raise the ultra-thin camera system from academic proof-of-principle prototypes to real world application scenarios in automotive industry, machine vision, or optical navigation to name a few only.

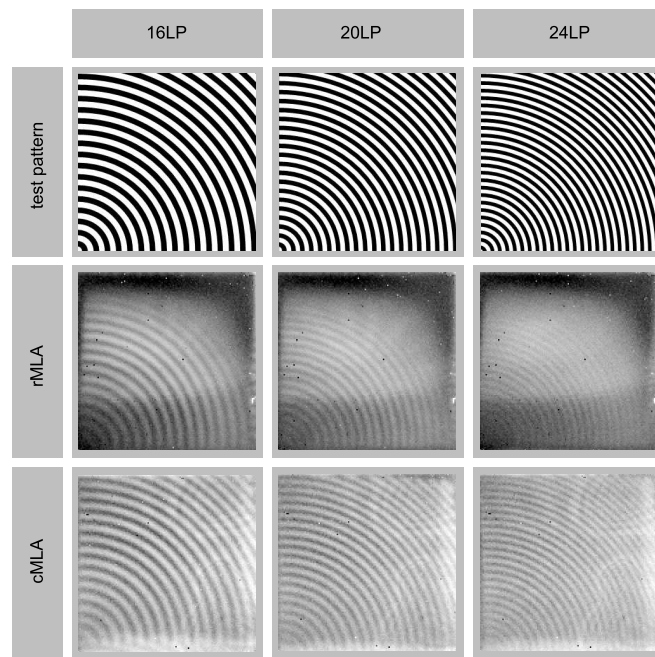


Figure 4.25: Circular symmetric test patterns of different spatial frequency (LP stands for line pairs over the FOV) centered on the center of FOV and captured images of those by using a cMLA for channel-wise aberration correction under oblique incidence and by using a regular lens array for comparison.

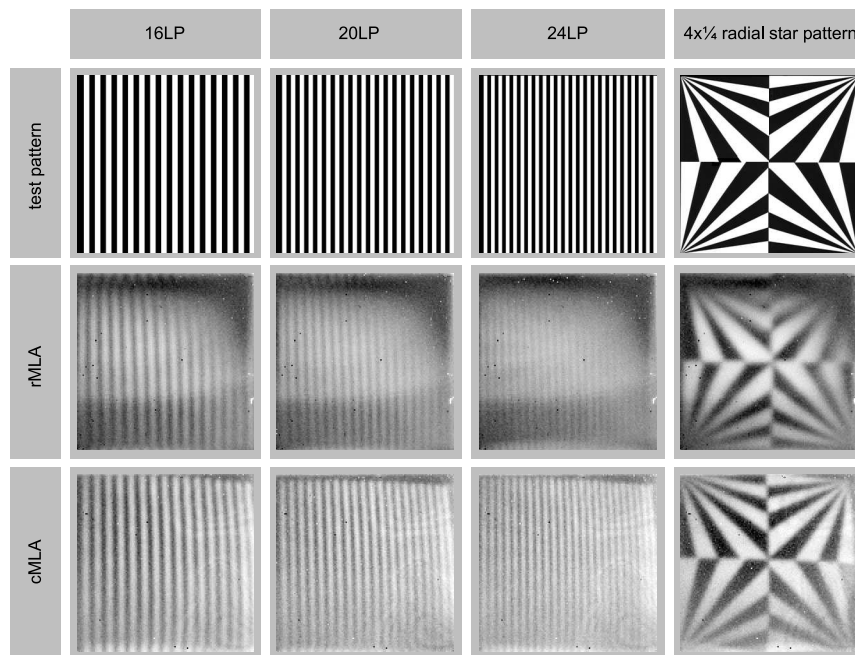


Figure 4.26: Bar targets of different spatial frequencies and captured images of those by using a cMLA for channel-wise aberration correction under oblique incidence and by using a regular lens array for comparison. Additionally, a specially adopted 4x1/4 radial star test pattern demonstrates the obtainable resolution in the four image corners as a function of the angle of incidence by the different radii of vanishing contrast of the radial star patterns.

4.2.2 cMLA of off-axis lens segments

A planar integrated free-space optical interconnect was designed, fabricated, and characterized as a second example for the use of cMLAs for the optimization of the optical performance. In contrast to the ultra-thin camera system of the previous section, laser lithography was used as fabrication technology for the cMLA since non-rotational symmetric microlenses were required. Further on, the parameters of the lenses were not calculated using analytical functions due to the complexity of the optical design task. Instead, the combination of numerical optimization at discrete sample points and fitted functions was used since the large number of different channels (660) would end up in a very time consuming optimization in case of a complete numerical treatment of the array.

Planar integrated free-space optical interconnect Optical interconnects are utilized for data communication between input and output devices for many channels in parallel and have manifold applications in the field of telecommunication. Both in- and output devices are usually arranged in arrays and may e.g. consist of singlemode fibers as input sources and detectors as outputs, respectively. Here, the small input and output components are not densely packed (so called dilute) but are placed on a regular grid leading to gaps between the electro-optical elements which are black or simply not required for achieving the optical functionality. Free-space optical interconnects perform an imaging of the input array onto the output array.⁵⁷ The quality of the imaging must be sufficiently good over the whole array in order to achieve a low loss and low crosstalk connection for all channels. Usually the pitches of the in- and output arrays are equal. Therefore, a magnification of unity is required which implicates a symmetrical optics design. Due to the use of dilute arrays, a hybrid imaging concept based on a 4F-setup is especially advantageous for the design of an interconnect (Sec. 2.3). A further improvement of the integration can be achieved if a planar integrated free-space optical system is used.^{147–149} Here, the optical beam path is folded into a monolithically integrated rugged substrate which allows for a wafer level fabrication and a mechanically stable system.³³

In a 4F-hybrid imaging setup (Fig. 2.4), the collimated beams of the different channels hit the first lens L1 of the conventional imaging system at different heights. In case of using very simple imaging systems, like single spherical elements, the optical bundles will suffer from different levels of spherical aberration introduced by the macroscopic lens. Besides using more complex well-corrected optics for the conventional stage of the hybrid imaging system the aberrations can easily be compensated channel-wise by implementing individually adapted microlenses. The use of an array with individually adapted cells in a hybrid imaging setup was already shown in Ref. 33. However, this was done using a different hybrid imaging configuration (2F/2F instead of a 4F setup). In addition, it was based on diffractive optical elements leading to low transmission efficiencies and was designed using analytical functions. The design presented here is based on refractive microlenses and a single off-the-shelf spherical

mirror for the conventional part of the hybrid imaging system. This provides the opportunity of building very cost effective free-space interconnects with optimized optical performance and high transmission efficiencies.

Optical system design The basic design concept is a conventional hybrid imaging system in a 4F configuration (Fig. 2.4) which is folded into a single glass substrate. For folding the beam path, the lenses L1 and L2 need to be replaced by curved mirrors. Additionally, a folding mirror placed in the plane of the common focal points is required in the center of the system. A further simplification results from substituting the two curved mirrors by one reflection-coated standard off-the-shelf spherical lens. In this case, half of the object plane can be used because the whole system is symmetric to the optical axis of the spherical mirror (Fig. 4.27). In- and output microlens arrays can be expected to be identical except for their orientation due to the symmetry of the system.

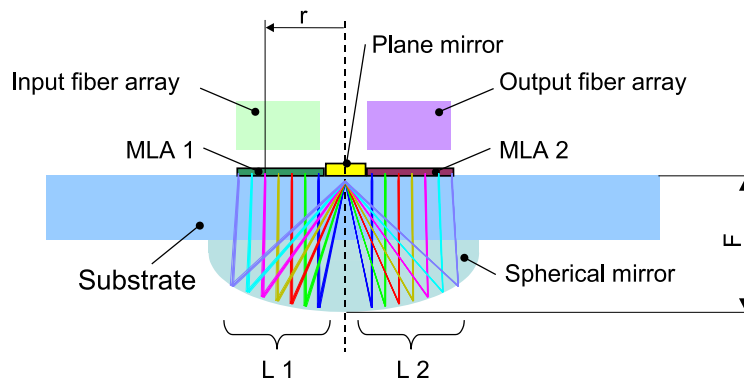


Figure 4.27: Schematic of the setup of the planar integrated free-space optical interconnect based on a 4F hybrid imaging setup.

As a consequence of the system's symmetry, the microlens' parameters are a function of the radial distance r which is measured from the microlens' centers to the optical axis of the system. Consequently, after the determination of the describing functions the parameters for all cells can easily be obtained as they only depend on the radial distance r .

The design was performed for singlemode fibers *Corning*[®] *SMF-28*TM with a mode field diameter of $10.5\mu\text{m}$ at $1.55\mu\text{m}$ wavelength as in- and output devices using numerical optimization functions provided by the commercial design software *ZEMAX*[®]. Here, several different configurations for different radial distances r reaching from 1mm to 4mm distance to the optical axis were analyzed.

In a first design step, the optimization was performed on geometrical and Gaussian beam propagation considerations for achieving maximum coupling between the in- and output fibers. From the geometrical optics point of view, constraints on the telecentricity of the system (chief rays in parallel to the optical axis of the system) as well as on the lateral position of the chief ray - which has to coincide with the fiber location - were implemented. Since the system is symmetric to the optical axis of the spherical mirror, the focal points of the differ-

ent channels have to coincide on the plane folding mirror. When using a regular microlens array, this requirement cannot be fulfilled as a consequence of the spherical aberration of the mirror [Fig. 4.28(a)] and the symmetry of the system is broken. As a consequence, a tilted and off-set bundle at the end face of the fiber leads to a decreased coupling efficiency [see Eq. (2.18)]. An effective way to compensate this effect of spherical aberration caused by the spherical mirror is to tilt the bundle with respect to the optical axis of the system. This can be accomplished by means of decentering the microlens with respect to the optical axis of the fiber [Fig. 4.28(b)]. In Fig. 4.28(c) a plot of the optical path difference (OPD) normalized to the wavelength $\lambda=1.55\mu\text{m}$ as a function of the distance r to the optical axis of the spherical mirror is given which is typical for spherical aberrations. In the simulation, the mirror was illuminated by a point source located at infinite distance on the optical axis of the mirror. The tilt angle and in consequence the decenter has to be adapted channel-wise. The amount of decenter depends on the radial distance r of a given channel with respect to the optical axis of the spherical mirror since the amount of spherical aberrations depends on the ray height on the spherical mirror. This leads in consequence to a cMLA configuration. The

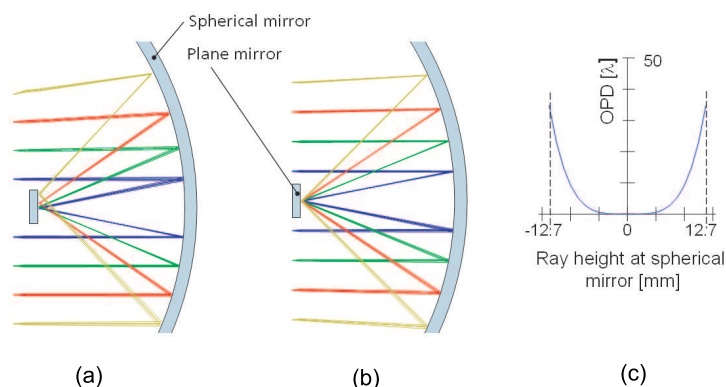


Figure 4.28: (a) Mismatch of the beam positions at the plane folding mirror and at the output fibers caused by the spherical aberrations introduced by the spherical mirror. (b) Aberration compensation using a cMLA. (c) Optical path difference vs. ray height of the spherical mirror. ($\lambda=1.55\mu\text{m}$).

beam waist of every single channel after hitting the spherical mirror the first time has to be located at the plane folding mirror which is again due to the symmetry of the system. The focal lengths of the microlenses have to be adapted for each channel as a consequence of the varying propagation distances.

The calculation of the Gaussian propagation parameters like waist radius and waist location in the design software is based on Fresnel diffraction in a completely analytical manner [Eqs. (2.8), (2.11), and (2.10)]. Using the associated operands in the optimization routines leads to a reasonably good starting system for the final optimization with the advantage of short calculation times. For final optimization, the propagation of the wave field through the system was modeled using the physical optics propagation tool within *ZEMAX*[®]. Here, the wave field is described as a set of complex amplitude values at discrete sampling points.⁹⁴ The pro-

propagation through free space is modeled by the angular spectrum of plane waves method^{80,150} or employing Fresnel diffraction. Based upon the Fresnel number Z of the beam

$$Z = \frac{A^2}{\lambda f}, \quad (4.29)$$

the software automatically decides which method has to be used for the propagation between the surfaces. Here, A denotes the radius of a single microlens, λ the wavelength, and f its focal length. For the interaction of the beam with optical surfaces the wave field is transformed into a set of rays. This set is traced through the optical boundary and subsequently transformed back into a wave field. Therefore, the software takes into account the refractive properties of the optical elements and is not limited by scalar diffraction theory with its approximation of infinite thin elements.

Finally, the coupling efficiency is optimized using Eq. (2.12) as part of the merit function which accounts for the field overlap of the propagated wave field with the mode field guided by the output singlemode fiber. The optimization was carried out for seven equidistantly spaced channels at radial locations r of 1mm up to 4mm distance to the optical axis. A small pitch of the fibers and the microlenses was chosen in order to achieve a compact device with a large number of channels. Consequently, off-axis lens segments were used which can be fabricated by laser lithography. This direct writing technique enables additionally the use of aspherical surfaces for aberration correction. Therefore, the lens shape was allowed to be anamorphic (different radii of curvature in two perpendicular directions) and to have non-zero conical constants, again possibly different in two perpendicular directions. In combination with the decenter of the lenses with respect to the optical axis of the fiber, five parameters are needed for a complete description of a single microlens. The optimization results for the seven equidistantly spaced channels are shown in Fig. 4.29 marked with diamonds.

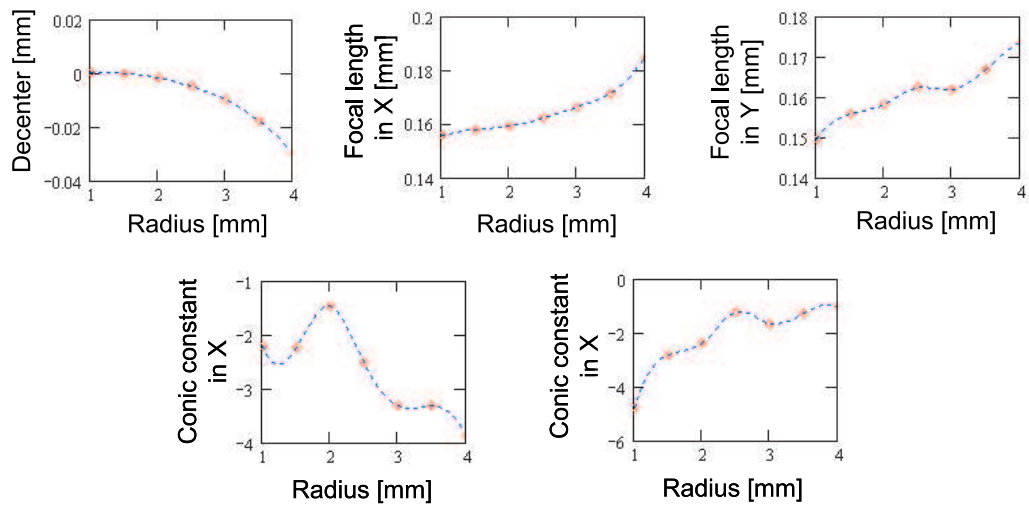


Figure 4.29: Optimized mathematical functions (dashed line) for the five parameters needed for the description of a single lens of the chirped MLA. Diamonds mark the optimized results for the seven calculated channels.

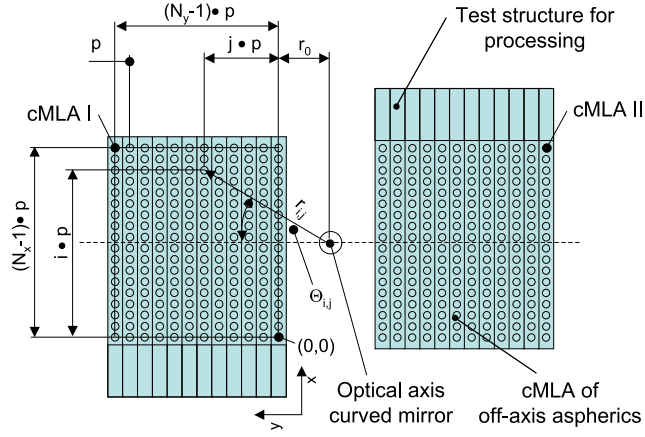


Figure 4.30: Schematic top view of the system and parameters needed for the calculation of the radial distance $r_{i,j}$ of each cell of the MLA.

Cubic splines were used as fitted functions depending on the radial distance r only for the calculation of the lens parameters for cells with radial distances which differ from the seven optimized channels. The radial distance r of the center of the cell to the symmetry axis has to be computed in a first step. Using regular arrays of constant pitch p in the x - and the y -direction the radial distance $r_{i,j}$ of the cell with index (i, j) is given by

$$r_{i,j} = \left\{ \left[\left(i - \frac{N_x - 1}{2} \right) \cdot p - \frac{p}{2} \right]^2 + (j \cdot p + r_0)^2 \right\}^{1/2}, \quad (4.30)$$

where r_0 is the distance from the first row of the array to the symmetry center in y -direction, N_x and N_y the number of channels in x - and y -direction, respectively (Fig. 4.30). The term $(N_x - 1)/2$ arises from the declaration of the cell with index $(0, 0)$ located in the lower left corner of the array.

Each lens of the array has to be rotated such that its plane containing the y -radius of curvature coincides with the tangential plane of the overall imaging system for each channel. From simple geometrical considerations the rotation angle can be calculated by

$$\Theta_{i,j} = \arccos \left[1 + \left(\frac{i - \frac{N_x - 1}{2} - \frac{1}{2}}{j + \frac{r_0}{p}} \right)^2 \right]^{1/2}. \quad (4.31)$$

For the prototype an array with 30 channels in the x - and 22 channels in the y -direction and a pitch p of $125\mu m$ was chosen, which fits to commercially available fiber arrays. The distance r_0 of the first row to the symmetry center was set to 1mm. In Fig. 4.31 the angle of rotation $\Theta_{i,j}$ and the radial distance $r_{i,j}$ of all cells of the array are plotted.

After the calculation of the radial distance $r_{i,j}$ for each cell, the parameters of the lenses can be calculated using the fitted functions. From simple geometrical considerations the decenter of the cells can be split into portions in the x - and the y -direction ($P_{x,i,j}$ and $P_{y,i,j}$) according to

$$P_{x_{i,j}} = P_{i,j} \cdot (1 + \tan^{-2} \Theta_{i,j})^{-1/2} \text{ and} \quad (4.32)$$

$$P_{y_{i,j}} = P_{i,j} \cdot (1 + \tan^2 \Theta_{i,j})^{-1/2}, \quad (4.33)$$

with $\Theta_{i,j}$ as the angle of rotation of the cell with index (i,j) and $P_{i,j}$ the amount of decenter. The required lens parameters for all cells are plotted in Fig. 4.32.

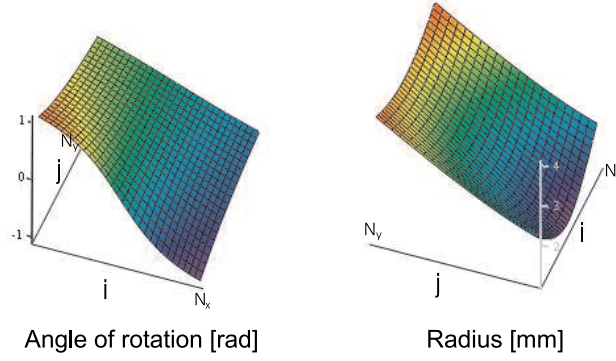


Figure 4.31: Angle of rotation Θ and radial distance r for all cells of the MLA. i - index of cell in x-direction, j - index of cell in y-direction, N_x - number of cells in x-direction, N_y - number of cells in y-direction. The position of the z-axis marks the cell with index (0,0).

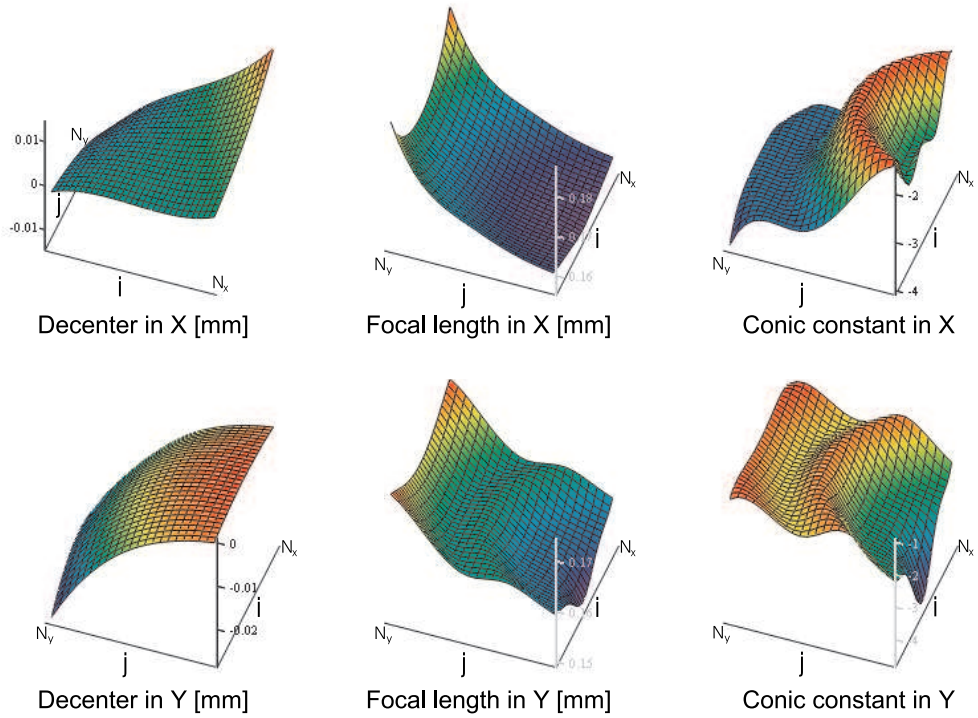


Figure 4.32: Decenter, focal lengths and conical constants for all lenses of the chirped MLA. i - index of cell in x-direction, j - index of cell in y-direction, N_x - number of cells in x-direction, N_y - number of cells in y-direction. The position of the z-axis marks the cell with index (0,0).

A macro for importing the lens parameters to *ZEMAX*[®] and calculating the coupling efficiency η_a for each single channel was used in order to verify the results for the shape of the single lenses. Figure 4.33 shows a plot of the theoretical coupling efficiencies, which are close to 100% for all channels.

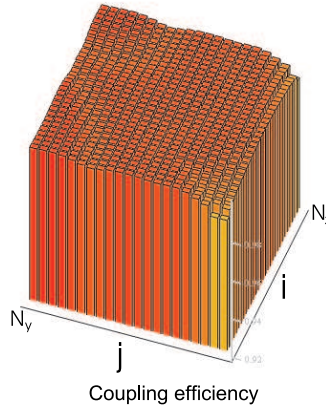


Figure 4.33: Calculated coupling efficiency for all channels of the system. i - index of cell in x-direction, j - index of cell in y-direction, N_x - number of cells in x-direction, N_y - number of cells in y-direction. The position of the z-axis marks the cell with index $(0, 0)$. The plotted scale reaches from 0.92 to 1.

The major advantage of using fitted functions is the possibility to calculate the parameters of the cMLA with a huge number of channels quickly whenever a sufficiently complete analytical description of the system is not possible. The optimization of the seven channels used as grid values took about 20 minutes. The calculation of the complete array using the fitted functions was carried out in seconds and the channel-wise verification of the complete array took about 10 minutes on a standard PC. When optimizing each channel by the numerical optimizer it would take about 32 hours. This time issue becomes even more relevant when dealing with larger arrays.

Prototyping of the cMLA The master structure of the two cMLAs was fabricated using laser lithography. The proposed writing scheme with refined height discretization was used due to the required large sag heights of $26.5\mu m$ (Sec. 3.4.2). A direct measurement of the lenses is troublesome due to the chirp of the lenses and the problems in locating the intended cells during the measurement. Therefore, a blazed grating with a depth of $15\mu m$ and a period of $62.5\mu m$ (half of lens pitch) as a simple test structure was added which can be accessed and measured easily with a profilometer (Fig. 4.30). When measuring the height profile, the influence of the steps of the coarse structure is marginal and a good overlay of the coarse and the fine structure leading to a continuous profile can be observed (Fig. 4.34). The rms-deviation of the surface is in the range of 120nm which is larger than the surface roughness achieved by reflow. However, since the cMLA will be used for aberration correction in a hybrid imaging free space optical interconnect for telecommunication applications working at a wavelength of $1.55\mu m$, nearly diffraction limited performance can be expected. The limiting

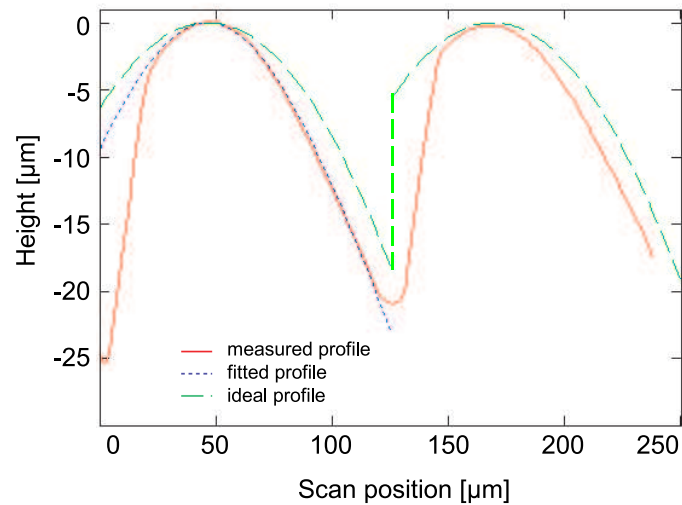


Figure 4.34: Comparison of the fitted, ideal, and measured profile for two adjacent lenses of the cMLA of off-axis lens segments.

factor for the surface roughness is the control of the laser intensity which has a tolerance of about 5%. The peak to valley deviation of the structure of about $4\mu m$ is more critical for the performance within the system. This is caused by the diffraction of the writing beam. The beam is auto-focused on top of the photoresist during the writing and diffracts while propagating. The Rayleigh length of about $7\mu m$ of the writing beam is much smaller than the resist height of about $30\mu m$. Therefore, the radiation dose deposited in the resist differs from the upper to the lower region. In consequence, a nonlinear dependence between the light intensity and the profile height results which has not been taken into account. The diffraction of the writing beam is of minor influence when writing diffractive elements since the structure heights are of the same magnitude as the Rayleigh length. This influence of diffraction can be reduced by readjusting the axial focus position during the writing not using the auto-focus function of the laser writer. Another reason for the deviation of the fabricated profile is a systematic mismatch between the intensity calibration used in the data preparation and the one used during fabrication due to an unrecognized misalignment of the machine. Taking both influences into account, the large peak to valley deviation can be dramatically reduced leading to well determined surface profiles. Another very important but not yet completely analyzed effect is the non-linear response of the used photoresist when structure heights larger than several microns are required. The optimization of fabricating high quality elements with large sag heights is under ongoing development and will result in reduced deviation of the fabricated profile compared to the designed one.

Experimental results In a subsequent UV-replication step after the fabrication of the master structure, the cMLAs were generated in *Ormocer*[®] material on *Schott Borofloat*[®] 33 wafers.^{5,144,151} Plane aluminum folding mirrors were deposited through a simple rectangular mask resulting in reflecting stripes of 1.3mm width before replicating the arrays onto the

wafers. The master structures of the cMLA were aligned with respect to the mirror stripe on the wafer to be centered between the in- and output arrays. Precise alignment is not necessary since the spots of each channel have a diameter of about $120\mu\text{m}$ only and hit the mirror at the same location [see Fig. 4.28(b)]. The alignment of the entire interconnect was done actively. Due to the lack of two dimensional fiber arrays with acceptable pitch tolerance, a single line silicon v-groove fiber array with $500\mu\text{m}$ pitch accommodating the in- and output fiber was used. Thus, within the test setup it was possible only to take measurements along the symmetry axis of the cMLA in the y-direction (dashed line in Fig. 4.30) as all other channels do not meet the exact pitch of the fiber array due to the tilted channels in relation to the symmetry axis. However, due to the fixed arrangement of the in- and output fibers, pointing errors caused by insufficient lens profiles cannot be compensated by lateral adjustment unlike using single fibers. Since the location of the in- and output devices in a real setup will be fixed as well, this kind of test setup is more realistic besides being much more critical. The aluminum coated spherical mirror, the wafer containing the cMLAs and the plane mirror, and the fiber array were mechanically connected to manipulation drives providing all required degrees of freedom for adjusting the components to each other (Fig. 4.35). By iterative optimization of all translational and rotational degrees of freedom the optimum alignment for high coupling efficiencies was adjusted.

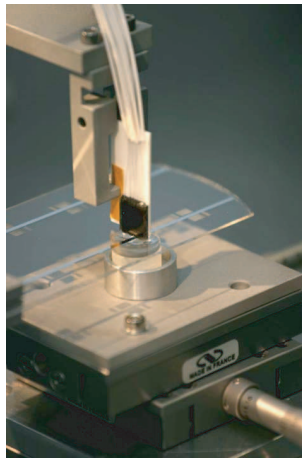


Figure 4.35: Detail of the assembled setup for lab verification.

The fiber array contained *SMF-28TM* singlemode fibers. The losses for coupling within the system along the center line in the y-direction at the wavelength $\lambda = 1.55\mu\text{m}$ were 15 to 17dB, including about 2dB Fresnel losses at the air glass interfaces and the losses at the three aluminum mirrors within the system. Though the losses are relatively large, competing systems based on diffractive optical elements have theoretically best performance values at the same level.³³ Fabrication tolerances are another source of losses besides insufficient alignment. In Fig. 4.34 a plot of the designed and measured height profile of two lenses of the array is

given [lenses with index (14,21) and (14,22)], which corresponds to the microlenses located on the center line in the x-direction and outermost in the y-direction of the left hand side cMLA (Fig. 4.30). The consequences of the large peak to valley deviation of almost $4\mu\text{m}$ are threefold. Firstly, a pointing error of the input beam results as a consequence of the too short focal lengths of the fabricated microlenses. The result is a lateral displacement of the field at the corresponding focusing microlens in cMLA2 and consequently a lateral and angular displacement of the focus with respect to the output fiber. Secondly, the waist of the Gaussian beam does not coincide axially with the end face of the output fiber and finally, aberrations are added to the beam.

The deviation of the fabricated to the ideal profile is even more obvious when looking at the grating test structure (Fig. 4.36). The development of the resist was carried out until the desired height of the sawtooth structure met the nominal value of $15\mu\text{m}$. The slope angle of the grating is steeper than intended and further on the angle of the slope is getting smaller at the bottom of the grating, nearly meeting the intended slope angle. The reason is an overexposure of the upper region of the photo resist due to the diffraction of the writing beam as explained beforehand. In consequence, a nonlinear context between the exposure intensity and the profile height results which has not been taken into account. This results in a variance of the radius of curvature of the microlenses and thus a change of the focal length and the deflection of the beam leading to increased coupling losses.

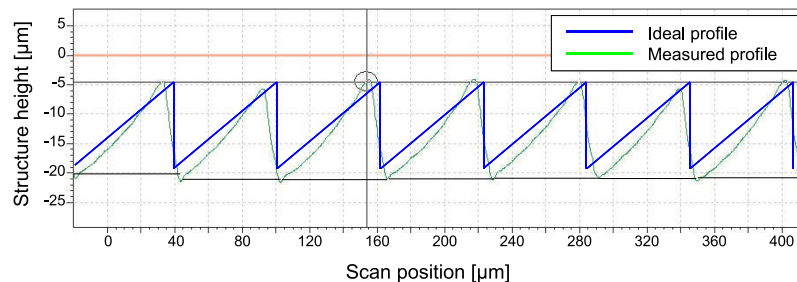


Figure 4.36: Plot of the height profile of the ideal and measured grating structure.

In order to check the consequences of the realized cMLA on the predicted performance of the interconnect, the parameters of the fitted profile were implemented into the *ZEMAX*[®] design file. The resulting coupling efficiency for this re-simulated channel is almost zero. However, the axial distance of the wafer containing the cMLA with respect to the fiber and the spherical mirror are two degrees of freedom when assembling the system which can be used for compensation. The simulation of the influence of the axial distance on the coupling efficiency is shown in Fig. 4.37. With this setup a theoretical maximum efficiency of 1.25dB is possible in case of an axial displacement of the lens of about $200\mu\text{m}$. However, even if the losses are much larger than the theoretical values, no coupling of radiation at all would have been possible between the fibers without using a cMLA due to the large aberrations of the spherical mirror.

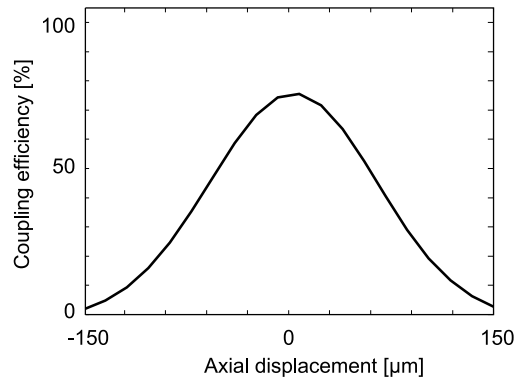


Figure 4.37: Calculated coupling efficiency of the system as a function of the axial displacement.

Table 4.6: Theoretical and measured insertion loss for fiber to fiber interconnections.

Input fiber	Output fiber	Theoretical insertion loss	Measured insertion loss
Singlemode $SMF-28^{TM}$	Singlemode $SMF-28^{TM}$	1.25dB	13...15dB
Singlemode $SMF-28^{TM}$	Multimode $100\mu m$, NA=0.3	0dB	1..3dB

The coupling into singlemode fibers is very sensitive to axial displacements and tilts due to the small mode field diameters. A less critical setup comprises singlemode fibers as input and multimode fibers or detectors as output devices. In the proposed system a single $SMF-28^{TM}$ singlemode fiber as input and a multimode fiber with a core diameter of $100\mu m$ and NA of 0.3 as output device were used each connected to translation stages. In the optimum adjustment insertion losses from 1 to 3dB (Fresnel and reflection losses of 2dB subtracted) for certain channel pairs distributed over the entire cMLA were measured. Here, the peak to valley deviations of the lenses are less critical, since the lateral mismatch and the defocus are widely tolerated by the large core diameter of the multimode fiber. However, the achieved losses are in the same range or slightly better than other designs proposed.^{152,153}

The presented system as an example for the use of a cMLA for the optimization of the optical performance comprises the numerical/analytical derivation of the cell parameters and the fabrication by laser lithography. The measured results for the insertion loss for the fiber to fiber connections do not meet the design values but can still compete with other state-of-the-art approaches.^{33,152} One reason for the coupling losses are due to the fabrication tolerances of the microlenses by laser lithography which can be improved with respect to minimization of the surface deviations especially in case of elements with large sag heights in the range of several ten microns.

5 Collective channel design

Each channel was designed individually in the previous chapter since no interaction between the channels occurred or was considered in the design. The arrayed layouts result from geometrical or fabrication related reasons. The second field of designs based on cMLAs is dedicated to systems where all channels work together in a collective manner. Here, coherent effects are of particular interest. The detailed phenomena taken into account strongly depend on the specific optical system to be designed. As an example for this category of designs, a fly's eye condenser based on cMLAs as beam homogenizer for coherent radiation sources is discussed.

State-of-the-art beam homogenizers are based on rMLAs in a tandem configuration (Sec. 2.4) which allow for the generation of top hat intensity distributions almost independent of the input distribution and with relaxed positioning tolerances. A periodic interference pattern with equidistant sharp intensity peaks results due to the periodic arrangement of the arrays when used under coherent and monochromatic illumination with radiation of a limited angular spectrum. These multiple-beam interference effects limit the homogeneity in the far field distribution. Consequently, breaking the periodicity of the MLA will lead to a non-periodic far field pattern which can yield an improved homogeneity. All the benefits of these systems resulting from the use of refractive microlens arrays such as small wavelength dependency, low scattering, relaxed positioning tolerances, and independence of temporal fluctuations of the input intensity distribution can be preserved.

5.1 Design considerations

The basic setup consists of a lens array followed by a Fourier lens as explained in Sec. 2.4. A tandem array has to be used in order to generate a top hat distribution without modulation but with sharp edges at the margins of the intensity distribution in the focal plane of the Fourier lens. Here, a second microlens is located in the focal plane of the microlenses of the first array having the same focal length as the first. According to Eq. (2.33), the width of the top hat in the focal plane of the Fourier lens is given by the numerical aperture μ of the lenses and the focal length F of the Fourier lens. Consequently, all channels must have the same numerical aperture [see Eq. (2.29)] and thus f-number η [see Eq. (2.28)] for achieving a top hat intensity distribution with sharp edges.

Wave optical considerations A far field intensity distribution with an envelope of a top hat according to Eq. (2.31) can only be achieved if the transmission function of an optical channel equals a sinc-distribution with a flat phase. Any finite extension of the aperture will clip the angular spectrum and due to the convolution of the rect-function with a sinc-function with finite extension some modulation will always be present in the far field [see Eq. (2.33)]. In analogy to the Airy disk diameter as a measure for the spot size for circular apertures, the

spot size d_{spot} for the cylindrical lens with rectangular aperture is defined here as the width between the first zeros around the maximum in the field amplitude. Figure 5.1 illustrates the influence of the clipping on the appearance of the far field distribution. Here, different apertures with widths $w_{norm} \cdot d_{spot}$ which act as spatial frequency filter are placed in the focal plane of the first microlenses where w_{norm} is a positive integer. Strong modulation can be noticed for widths less than $10 \cdot d_{spot}$. The far field distribution is almost stable for bigger values of w_{norm} . However, no perfect top hat without any modulation can be achieved due to the clipping. In consequence, the width of the lenses should be at least 10 times larger than the spot diameter in a proper design to avoid large deviations from the top hat distribution.

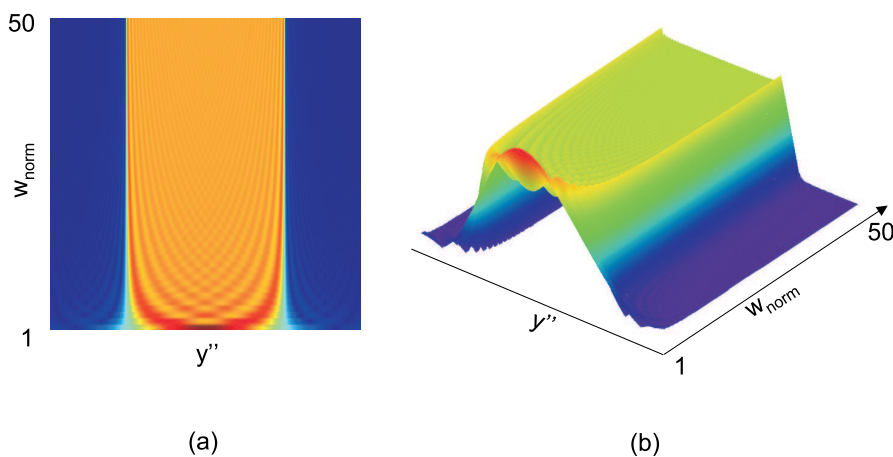


Figure 5.1: Far field intensity distribution in arbitrary units in the focal plane of the Fourier lens as a function of the aperture clipping in the focal plane of the first microlens. w_{norm} - ratio of the aperture width to the diffraction limited spot diameter in the focal plane of the first microlens, y'' - coordinate in focal plane of the Fourier lens.

Geometrical considerations The fill factor of the arrays as the ratio of the area covered with lenses and the total area of the array has to be as close as possible to unity in order to achieve maximum transmission efficiency of the system. Therefore, when chirping the positions of the lenses in order to destroy the periodicity of the array, the apertures have to be chirped as well and consequently the focal lengths of the MLA have to be chirped for achieving constant NA for all lenses. Almost arbitrary chirp functions are possible theoretically with the constraints of maximum fill factor and constant NA for all cells. The practical producibility of the components limits the reasonable solutions since it is mandatory that the second array is located in the focal planes of the first one in order to achieve a top hat. This is due to the fact that the majority of microlens fabrication techniques are bound to planar substrates. Consequently, the most suitable setup results when placing both arrays on planar substrates which enables the use of e.g. reflow of photoresist as fabrication method leading to very smooth and well defined surfaces (Fig. 5.2).

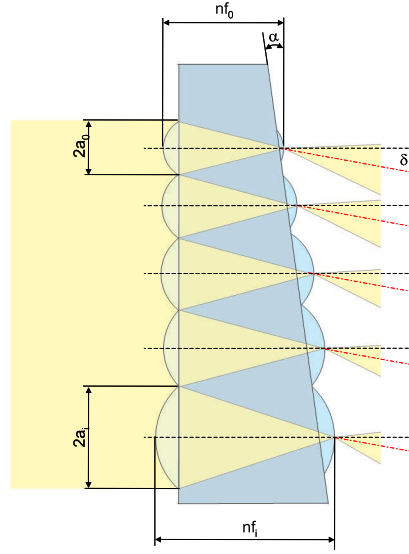


Figure 5.2: Geometry of a tandem cMLA with two plane surfaces in a wedge configuration. $2a_0$ - width of lens with index 0, $2a_i$ - width of lens with index i , f_0 - focal length of lens with index 0, f_i - focal length of lens with index i , n - index of refraction, α - wedge angle, δ - deflection angle.

5.2 Evaluation of homogenization

A quality measure describing the degree of homogenization has to be used in order to compare the quality of homogenization of different optical setups. One important measure is the ratio q of the standard deviation σ_{dev} to the mean value m of the intensity distribution which is sampled at M supporting points referred to as beam uniformity¹⁵⁴

$$q = \frac{\sigma_{dev}}{m}, \quad (5.1)$$

with

$$\sigma_{dev} = \sqrt{\frac{1}{M-1} \sum_i^M (x_i - m)^2} \text{ and} \quad (5.2)$$

$$m = \frac{1}{M} \sum_i^M x_i. \quad (5.3)$$

For a perfect top hat, q equals 0. Otherwise q is larger than 0 and consequently the larger q , the poorer the degree of homogenization. Assuming a periodic intensity distribution with a pulse width b , period p_a and amplitude v according to Fig. 5.3(a), the mean value and standard deviation yield

$$\sigma = v \sqrt{d_q^{-1} - d_q^{-2}} \text{ and} \quad (5.4)$$

$$m = \frac{v}{d_q}, \quad (5.5)$$

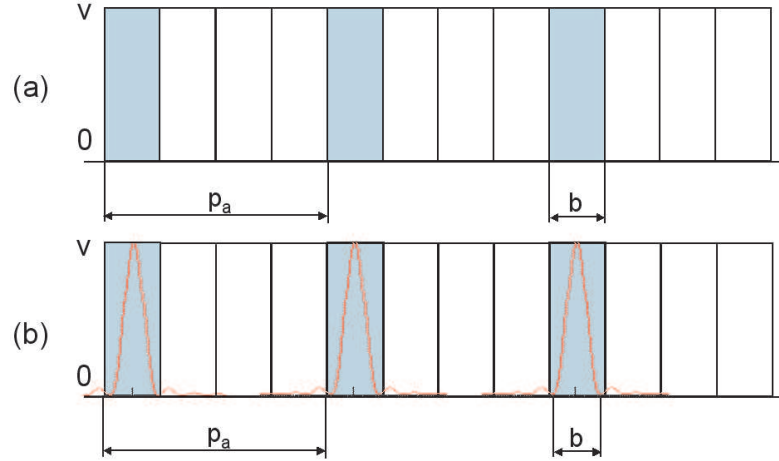


Figure 5.3: Schematic drawing for the explanation of the quality factor q of regular MLAs. (a) Periodic rectangular pulse string. (b) Periodic sinc-pulse string. p_a - period, b - burst width.

with $d_q = p_a/b$. For this distribution the quality factor q_a simplifies to

$$q_a = \sqrt{d_q - 1}. \quad (5.6)$$

The far field intensity distribution is ideally similar to that shown in Fig. 5.3(b) for a fly's eye condenser based on a regular tandem MLA. The distance p_a between adjacent peaks can be calculated using the paraxial grating equation

$$p_a = \frac{F\lambda}{2a}, \quad (5.7)$$

where F is the focal length of the Fourier lens and $2a$ is the pitch of the array. On the other hand, the width b of a peak results from diffraction at the aperture of the entire array [see Eq. (2.23)] and is given by

$$b = \frac{F\lambda}{2a \cdot N}. \quad (5.8)$$

Therefore, the factor d_q equals N being the number of lenses in the array. The difference in the shape of the peaks of the periodic intensity distributions have to be taken into account using a factor k_q leading to the simple equation for the quality factor q for regular arrays

$$q = \sqrt{k_q \cdot N - 1}. \quad (5.9)$$

The defined quality factor q is independent of the pitch and the NA of the microlenses as well as of the focal length F of the Fourier lens. It is only dependent on the number of lenses of the array. Therefore, with increasing number of illuminated lenses the homogeneity deteriorates which is due to the constriction of the peaks. This is contrary to the geometric optical considerations where homogeneity improves with the number of lenses. In Fig. 5.4 the

simulation results are plotted using the wave optical propagation software *Virtual LabTM3.1* and the graph according to Eq. (5.9). Both graphs match perfectly for $k_q=0.66$. This is a confirmation of the accuracy of the simulation and gives confidence that the results for the cMLA are correct, too.

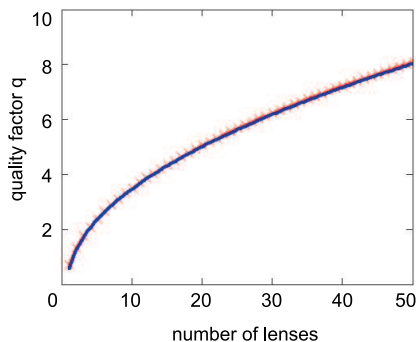


Figure 5.4: Quality factor q as a function of the number of illuminated lenses for a regular array. crosses - numerical simulation, line - analytical function according to Eq. (5.9) $k_q=0.66$.

5.3 Numerical simulation

The far field distribution of regular MLAs can be calculated very easily in a completely analytical manner using Eq. (2.23). This is due to the fact that the Fourier transformation of a comb-function results in another comb-function but of different spacing. In case of a cMLA, the transmission function of the array in general can easily be written in analogy to the transmission function of a regular array [see Eq. 2.22] as

$$u(y') \propto \sum_{i=0}^{N-1} \left\{ \delta \left[y' - \left(a_0 + 2 \sum_o^{i-1} a_o + a_i \right) \right] \otimes \left[\text{sinc} \left(\frac{y'}{\eta\lambda} \right) \cdot \text{rect} \left(\frac{y'}{2a_i} \right) \right] \cdot \exp \left[j \frac{2\pi}{\lambda} (n-1) n (f_i - f_0) \right] \right\}. \quad (5.10)$$

The δ -function of the first term encodes the center positions of the channels. The second term describes the field of a single channel of the tandem MLA according to Eq. (2.30) having a flat phase due to the second microlenses. Since it depends only on the NA or f-number of the lens - which is identical for all lenses of the arrays - the field directly behind the second lens is the same for all channels. The rect-function accounts for the clipping of the field caused by the finite width of the aperture of the second lens. The channel-wise constant piston phase factor results from the different propagation lengths of the channels in media with different indices of refraction (air and wedge material, respectively). The detailed values of the widths $2a_i$ and focal lengths f_i are determined by the parametric chirp functions and hence by the geometry of the array. For calculating the far field distribution, Eq. (5.10) has to be Fourier transformed which is possible numerically only. Equation (5.10) describes a geometry as shown in Fig. 5.5.

Here, the wedge between the two arrays is approximated as a staircase since such a geometry without tilted surfaces can easily be described by scalar diffraction theory. However, the only difference to the setup with two plane surfaces accommodating the arrays is a missing prism term which will lead to a deflection by an angle of δ (Fig. 5.2).

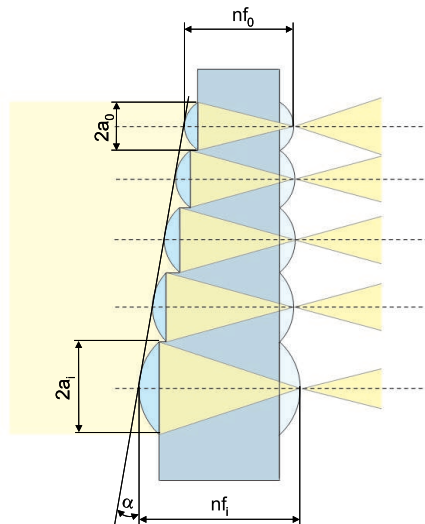


Figure 5.5: Staircase model of a tandem cMLA with constant NA for all channels as approximation to a wedge configuration.

The geometrical parameters for all channels of the array were obtained from a given NA, minimum focal length f_0 , and wedge angle α using Eqs. (5.13) and (5.14) in the first step of the computation of the far field distribution. This was done using the maths software *MathCADTM* 11. The lens parameters were exported as a txt-file which could be imported into the wave optical software *Virtual LabTM* 3.1. According to Eq. (5.10), an array of sinc-functions clipped by the associated aperture sizes and centered at the related lens vertex position was generated. Then the channel-wise constant piston phase was multiplied to the amplitude distribution of the array and finally the Fourier transformation was executed. The tandem cMLA is illuminated in the simulation by a single plane wave of constant amplitude at perpendicular incidence meaning that a perfectly coherent beam without any divergence is assumed.

5.4 Fly's eye condenser with planar substrates

The majority of state-of-the-art microlens manufacturing techniques are limited to planar substrates. Consequently, for a tandem microlens array with non-identical lenslets a wedge configuration results. Here, the cell widths $2a_i$ and focal lengths f_i (Fig. 5.2) of all lenses of the cMLA can be calculated using analytical equations having the wedge angle α , the NA of the lenses, and the minimum focal length f_0 as parameters. From simple geometrical considerations it can be found that the focal length of the lens in air next to the smallest lens

is given by

$$f_1 = f_0 + (a_0 + a_1) \frac{\tan \alpha}{n}, \quad (5.11)$$

with n as the index of refraction of the wedge material, a_0 and a_1 the semi-widths of the smallest and the adjacent lens, respectively. Using Eq. (2.28), the semi-width of the lens with index $i=1$ is

$$a_1 = \frac{f_0 + a_0 \frac{\tan \alpha}{n}}{2\eta - \frac{\tan \alpha}{n}}, \quad (5.12)$$

with η as the f-number of the microlenses [see Eq.(2.28)]. The focal length of the lens with index i can be calculated by

$$f_i = f_0 + \left(a_0 + 2 \sum_{o=1}^{i-1} a_o + a_i \right) \frac{\tan \alpha}{n}, \quad (5.13)$$

and the semi-width of the i -th lens consequently is

$$a_i = \frac{f_0 + \left(\frac{f_0}{2\eta} + 2 \sum_{o=1}^{i-1} a_o \right) \frac{\tan \alpha}{n}}{2\eta - \frac{\tan \alpha}{n}}. \quad (5.14)$$

The focal lengths of all cells can easily be calculated using Eq. (2.28) or (2.29).

5.4.1 Simulation results

The far field distributions were calculated based on the proposed numerical algorithm as a function of the NA of the microlenses, the minimum focal length f_0 , the angle of the wedge α , and the number of illuminated lenses N . In Fig. 5.6 examples of the calculated far field distribution are given for a wedge angle of 0° (regular array) and 7° . In case of the cMLA, a speckle pattern with smaller and non-regular peak distances compared to regular arrays results as a consequence of the multiple beam interference. This leads to an improved homogenization. Figure 5.7 shows a plot of the quality factor q as a function of the wedge angle α and the number of lenses N when using microlenses with a NA=0.03 and a minimum focal length f_0 of

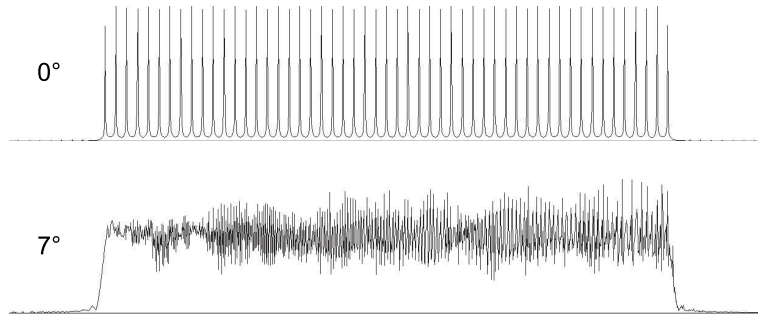


Figure 5.6: Calculated far field intensity distribution of a fly's eye condensers using 50 lenses with NA 0.05 and a minimum focal length of 2.63mm with a wedge angle of 0° (regular MLA) and 7° .

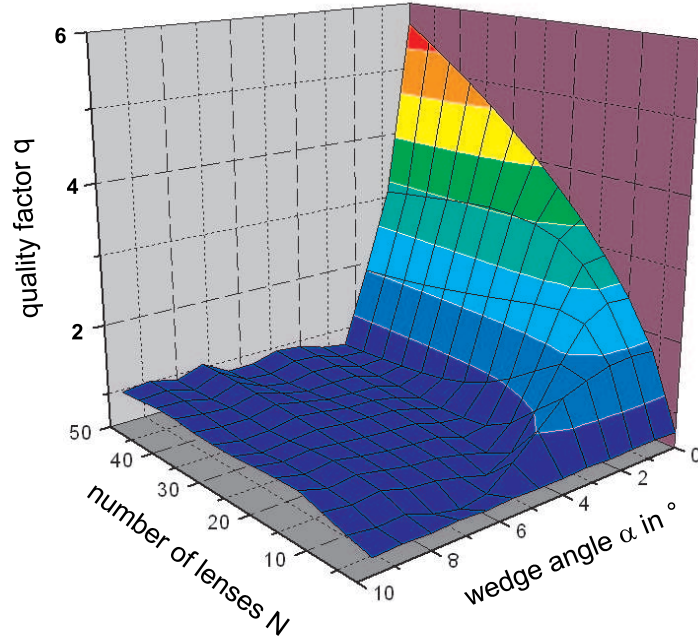


Figure 5.7: Quality factor q as a function of the wedge angle α and the number of illuminated lenses N . minimum focal length $f_0=2.0\text{mm}$, $\text{NA}=0.03$ for all microlenses.

2.63mm. For a wedge angle of 0° , a regular MLA results leading to a curve according to Eq. (5.9). With increased wedge angle the quality factor decreases indicating a better degree of homogenization. The larger the number of illuminated lenses, the smaller the wedge angle can be allowing for a constant degree of homogenization. However, for increasing wedge angle and number of lenses the minimum quality factor drops never significantly below unity meaning that the standard deviation and the mean value of the intensity distributions are about the same. The proposed quality factor q is a global measure of the entire intensity distribution which is not significantly influenced by local hot spots in the distribution. Therefore, it is necessary to have a detailed look at the resulting far field intensity distribution. In Fig. 5.8 different plots of the far field intensity distribution as a function of the wedge angle α are given for different numbers of illuminated lenses. Each line in the diagram is normalized to the maximum intensity value for that specific angle. A regular peak pattern results for a wedge angle of zero. Firstly, the appearance of the patterns becomes more stable when increasing the number of illuminated lenses [Fig. 5.8 from (a) to (h)]. Since the distributions result from multiple beam interference effects, the change in the number of involved beams has a stronger impact when dealing with a small number of beams or lenses, respectively. Secondly, a region with peaks of higher intensity is shifted towards the left side of the distribution when increasing the wedge angle [Fig. 5.9(b)]. This is caused by the shift of the point where the zeroth orders of the lenses interfere constructively. This shift is due to the channel-wise different piston phase caused by the staircase geometry of the tandem cMLA which results in a deflection of the zeroth orders. If this deflection angle exceeds the divergence angle of the

microlenses which is determined by their NA, no peak will appear in the intensity distribution. The staircase geometry acts as a prism for the zeroth orders. Therefore, no hot spots will be present in the intensity distribution for wedge angles larger than the critical angle α_c

$$\alpha_c = \arcsin\left(\frac{\mu}{n-1}\right). \quad (5.15)$$

No channel-wise different piston phases will occur in case of air between the two cMLAs of the tandem array. Consequently, the zeroth orders would always interfere constructively in the center of the distribution. Figure 5.9(a) shows the calculated far field pattern again as a function of the angle between the two arrays but with air in between the lenses. Beginning with a regular array on top resulting in a regular interference pattern, the homogenization of the distribution in general improves with increasing angle. However, since the zeroth orders always coincide in the center of the distribution, a hot spot is always present which is of course undesired. In conclusion, it is not sufficient to look at the quality factor for choosing the appropriate amount of required chirp since localized hot spots caused by the constructive interference of the zeroth orders of the cMLA's channels can still be present. A wedge angle larger than the critical angle α_c has to be applied for avoiding these intensity peaks. Using configurations with even larger wedge angles will of course change the specific speckle pattern but not improve the overall homogeneity (Fig. 5.10). In Fig. 5.11 plots of the far field intensity distribution as a function of the wedge angle α are given for different NAs of the microlenses but with constant minimum focal length $f_0=2.63\text{mm}$ and number of illuminated lenses $N=50$. In case of a small NA, the ratio of the spot size in the focal plane of the first

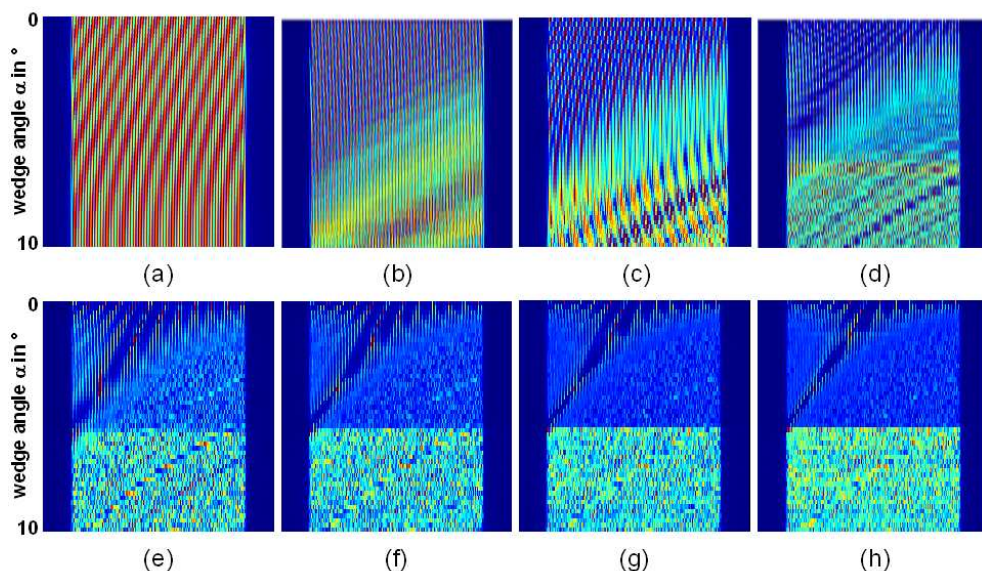


Figure 5.8: Calculated far field distribution as a function of the wedge angle α . Minimum focal length $f_0=2.63\text{mm}$, $\text{NA}=0.05$ for all microlenses, $\lambda=0.55\mu\text{m}$, index of refraction $n=1.52$. Number of illuminated lenses: (a) 2, (b) 4, (c) 6, (d) 10, (e) 20, (f) 30, (g) 40, (h) 50.

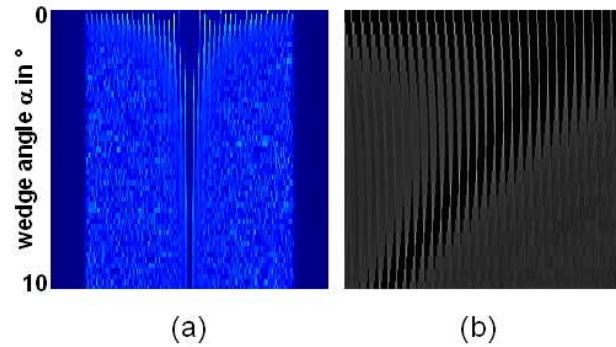


Figure 5.9: Calculated far field distribution as a function of the wedge angle α . Minimum focal length $f_0=2.0\text{mm}$, $\text{NA}=0.05$ for all microlenses, number of illuminated lenses $N=50$. (a) index of refraction $n=1.0$ (air), (b) detail of Fig. 5.8(h) showing the shift of the hot spot and increasing homogeneity of surrounding areas with increasing wedge angle.

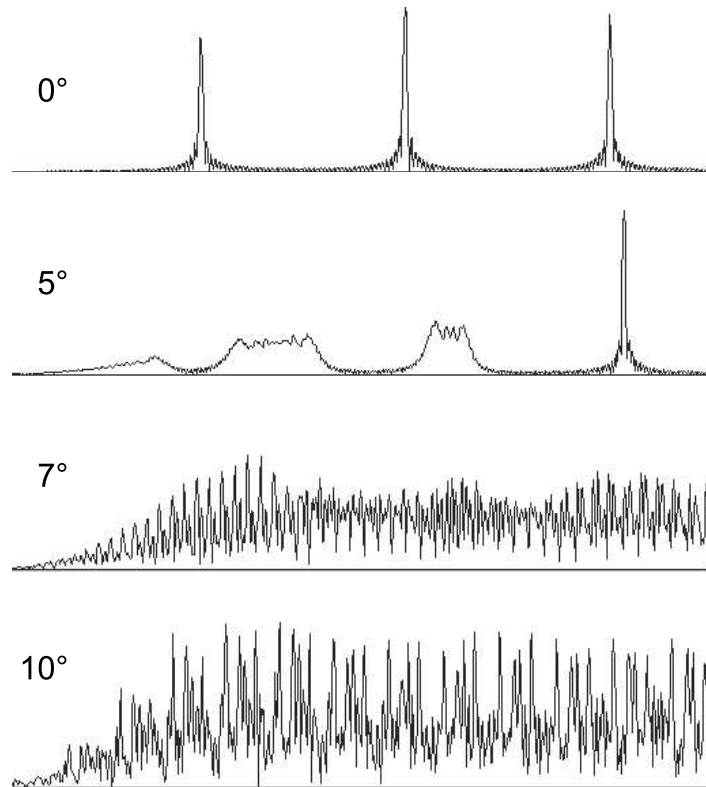


Figure 5.10: Details of the edge of the far field distribution for different wedge angles α . Minimum focal length $f_0=2.63\text{mm}$, $\text{NA}=0.05$, 50 illuminated lenses. In case of a regular MLA (0° wedge angle) equidistantly located peaks result. The hot spot caused by the zeroth orders of the lenses is within the distribution derogating the homogeneity if the wedge angle is smaller than the critical angle of 5.5° . A non-periodic speckle pattern with smaller peak distances results for a wedge angle larger than the critical angle leading to an improved homogeneity. A further increase of the wedge angle influences the speckle pattern but does not significantly improve the homogeneity.

microlens and the width of the lenses becomes too small and the aperture of the second lens clips large fractions of the angular spectrum. Consequently, the far field distribution deviates considerably from the desired top hat as can be seen in Fig. 5.11(a). Here, the spot diameter in the focal plane of the first lens is about $55\mu\text{m}$ while the aperture width of the second lens is $263\mu\text{m}$. According to Eq. (5.15), the critical angle - where the hot spot leaves the far field distribution - increases with increasing lens NA (Fig. 5.11(b) to (e)). The critical angle becomes 10° for a lens NA of 0.09 when a wedge material with index of refraction of 1.52 is used. Consequently, the hot spot will not be shifted enough in the diagrams to be outside the distribution. Due to the different NAs of the configurations plotted in Fig. 5.11, the distribution have different extension which is given by the NA of microlenses and focal length of the Fourier lens [see Eq. (2.33)] but are shown with different magnification in x-direction for better illustration. Furthermore, since the minimum focal length is kept constant, the lens widths of the different configurations increase with increasing NA and consequently according to Eq. (5.7), the distance between adjacent intensity peaks becomes smaller. Therefore, the extent of the modulated region around the hot spot is decreasing with increasing NA. Finally,

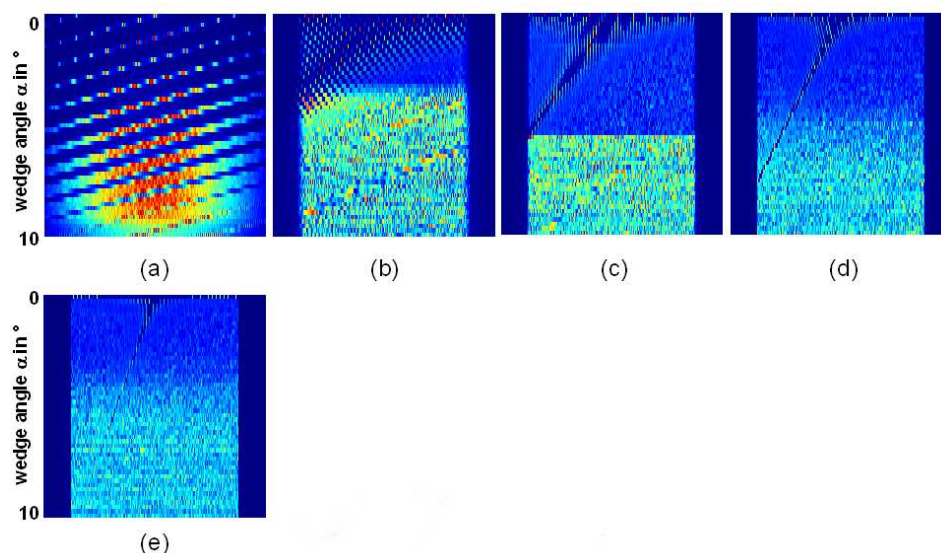


Figure 5.11: Calculated far field distribution as a function of the wedge angle α . Minimum focal length $f_0=2.63\text{mm}$, number of illuminated lenses $N=50$, $\lambda=0.55\mu\text{m}$, index of refraction $n=1.52$. NA: (a) 0.01, (b) 0.03, (c) 0.05, (d) 0.07, (e) 0.10. The diagrams have different magnification in the x-direction for better comparability.

in Fig. 5.12 plots of the far field intensity distribution as a function of the wedge angle are given each using 50 illuminated microlenses with NA of 0.05 but of different minimum focal lengths. The lens widths scale with the minimum focal length according to Eq. (5.7) since the NA is constant. Consequently, the distance of adjacent intensity peaks is smaller for larger minimum focal lengths and the modulated region around the hot spot sharpens. The hot spot leaves the distributions at the same critical angle of 5.5° due to the constant NA for all configurations.

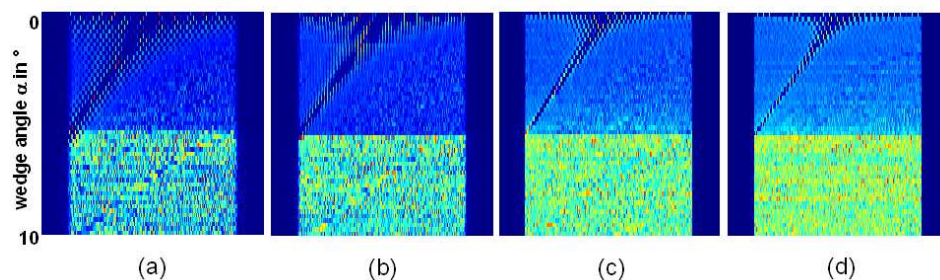


Figure 5.12: Calculated far field distribution as a function of the wedge angle α . NA=0.05, number of illuminated lenses N=50, $\lambda=0.55\mu\text{m}$, index of refraction $n=1.52$, minimum focal length f_0 : (a) 1.32mm, (b) 2.63mm, (c) 6.58mm, (d) 9.87mm.

5.4.2 Practical considerations

The wedge configuration is approximated by a staircase setup in the simulation which is rather difficult to fabricate practically. As already mentioned, a more applicatory solution is to use two planar substrates which are tilted with respect to each other (Fig. 5.2). Depending on the orientation of the wedge, different cMLA designs result. In the simulation the substrate of the second lenses is perpendicular to the optical axis of the setup hence the first array is tilted by the wedge angle α . If the second array is placed in the object focal plane of the Fourier lens, each channel will generate a plane wave after passing the Fourier lens with different orientation angles with respect to the optical axis of the system. Due to the oblique incidence with respect to the surface normal of the first array, a deflection results and consequently the lenses of the second array have to be laterally shifted where the amount of shift depends on the deflection angle ϵ after the first lens and the focal length f_i of each channel. A further deflection results as a consequence of the refraction at the second array. The deflection is constant for all channels and will lead to a lateral offset of the distribution in the focal plane of the Fourier lens. The deflection and hence the lateral shift in the Fourier plane can be avoided if the microlenses of the second array are decentered channel-wise by Λ_i (Fig. 5.13). The amount of decenter is given by

$$\Lambda_i = \tan \delta \cdot f_i, \quad (5.16)$$

where f_i is the focal length of the microlens of the i -th channel and δ is the deflection angle of the wedge (Fig. 5.2). The deflection angle can be calculated by⁵³

$$\delta = \theta + \arcsin \left[(\sin \alpha) (n^2 - \sin^2 \theta)^{1/2} - \sin \theta \cos \alpha \right] - \alpha, \quad (5.17)$$

with θ as the angle of incidence on the first surface which equals the wedge angle α . Another possible arrangement is to orientate the first array perpendicular to the optical axis of the system. Consequently, no deflection after the first array results and the lenses of the second array do not have to be shifted. Now, the deflection occurs when leaving the second array

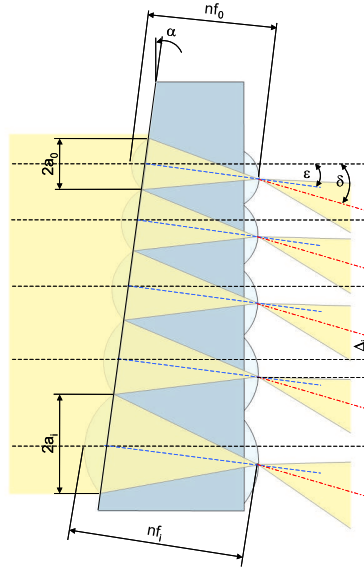


Figure 5.13: Geometry of a tandem cMLA with two plane surfaces in a wedge configuration with compensation of the deflection. $2a_0$ - width of lens with index 0, $2a_i$ - width of lens with index i , f_0 - focal length of lens with index 0, f_i - focal length of lens with index i , n - index of refraction, α - angle between plane surfaces, ϵ - deflection angle after first lens array.

which can be calculated using Eq. (5.17) with $\theta=0^\circ$. Again, the deflection can be compensated by a lateral shift of the lenses of the second array using Eq. (5.16). However, since the second array is tilted, one channel can be placed in the object focal plane of the Fourier lens only. Consequently, all other channels will have a spherical phase in the image focal plane of the Fourier lens due to their defocus which will influence the intensity distribution.

A perfectly coherent illumination with a single plane wave is assumed in the simulation. These conditions will not be fulfilled in a real world scenario and instead the cMLA will be illuminated with a finite angular spectrum and the input radiation will be partly coherent only. These effects will lead to a washing out of the intensity peaks and lead to an improved homogenization even for the regular MLA. However, in the previous considerations a worst case appraisal was examined. The improvement of the homogeneity due to the relaxed illumination conditions are true for the cMLA as well. Consequently, this will lead to a further improvement of the homogeneity compared to the presented values.

A common method for improving the homogeneity in fly's eye condensers is to use additional dynamic elements to change the phase of the incoming radiation such as rotating diffusers which of course make sense only if the considered time frames are sufficiently long enough allowing for time averaging. Additional elements are required since the direct movement of the regular tandem arrays will not help to improve the homogeneity because of the translation independence. When using cMLAs a direct movement of the tandem array perpendicular to the optical axis will change the speckle pattern in the far field and can help to improve the homogeneity when averaging over a certain time interval. The changes in phases in the intensity distribution are even more sensitive to a perpendicular translation in case of the system where

the second array is tilted due to the spherical phases of the interfering waves. However, these consideration have been mentioned only for pointing out further properties and applications of cMLAs without being discussed in detail which will be part of future work.

5.4.3 Experimental results

As a first prototype, a fly’s eye condenser with a wedge angle of 5° using cylindrical microlenses with a NA of 0.05 and a minimum focal length f_0 of 2mm was fabricated. Reflow of photoresist was used as fabrication method for the two cMLAs. The individual arrays were manually aligned to build up the wedge configuration after a subsequent UV-replication. An UV-curing epoxy (*Norland NOA 61*¹⁵⁵) with index of refraction of 1.52 at $0.55\mu\text{m}$ wavelength was used as material in between the two substrates. In Fig. 5.14 a plot of the measured and designed values of the radii of curvature of the lenses of the cMLA is given. The maximum relative deviation between the produced and the designed values is approximately 1%. Figure 5.15 shows a

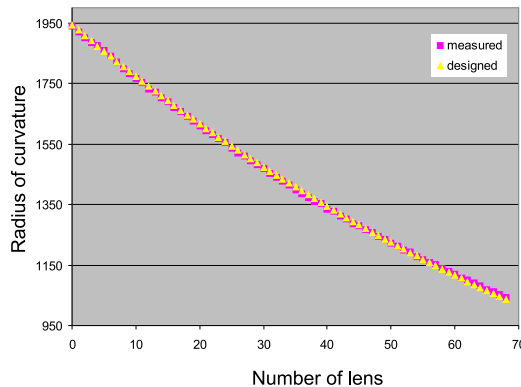


Figure 5.14: Measured and designed radii of curvature for the cylindrical lenses of the cMLA. The maximum deviation is approximately 1%.

photograph of the assembled tandem cMLA fly’s eye condenser. The glass plates on top and at the bottom are used for fixation of the cMLAs and integration into the homogenizing setups. Figure 5.16 shows the captured intensity profile of the resulting line focus when using a collimated beam of a HeNe-laser (wavelength of 633nm) and a Fourier lens with 500mm focal length. The distance of adjacent peaks is about $80\mu\text{m}$. When using a regular array consisting of lenses of the size of the smallest or largest lens of the used cMLA, intensity peaks with distances of $550\mu\text{m}$ or 1.13mm, respectively according to Eq. (5.7) will occur in the focal plane of the Fourier lens. Due to the irregularity of the cMLA, the intensity peaks are closer compared to the regular MLAs by a factor of 7 to 14 showing the improvement of homogenization. Homogenization is not achieved throughout the entire intensity distribution and a hot spot is still observable at the margin of the line (not shown in the picture) which is caused by the wedge angle being smaller than the critical angle α_c of 5.5° [Eq. (5.15)].

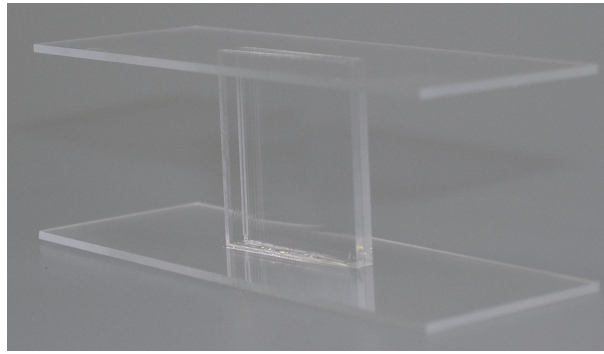


Figure 5.15: Photograph of the prototype of a tandem fly's eye condenser using cMLAs on plane surfaces in a wedge configuration.

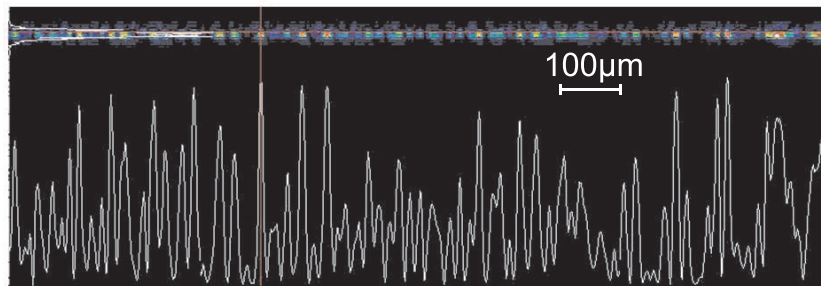


Figure 5.16: Measured intensity distribution of a chirped cylindrical tandem microlens array. Peak distance is approximately $80\mu\text{m}$. The theoretical peak distance of a regular array with a pitch of maximum or minimum lens width of the chirped array is 0.55mm and 1.13mm , respectively. *Top*: Two-dimensional measurement of the intensity distribution of the line focus in false-color representation. *Bottom*: Cross section of the intensity distribution of the line focus in arbitrary intensity units.

5.5 Fly's eye condensers with non-planar substrates

Curved substrates The accommodation of the arrays on plane substrates results only from recent manufacturing limitations. With evolving fabrication techniques, such as laser lithography, it is also possible to use e.g. curved substrates¹¹⁴ (Fig. 5.17). The advantage in using these substrates is that the phase differences accumulated by the single channels during propagation are not linearly depending on the distance to the optical axis as in a wedge configuration. Consequently, there is no point in the distribution where all zeroth orders interfere constructively. Again, the focal lengths f_i and cell widths $2a_i$ are depending on geometrical aspects and can be calculated using analytical equations having the radius of curvature R , the NA of the lenses, and the maximum focal length f_0 as parameters. The plane and curved surfaces form a macroscopic plano-convex cylindrical lens. Its local sag height has to correspond to the focal length $f(x)$ of the microlens placed in the distance x which is measured with respect to the vertex of the macroscopic lens to the vertex of the microlens. From simple geometry of the circle follows

$$f(x) = f_0 - \frac{1}{n} \left(R - \sqrt{R^2 - x^2} \right). \quad (5.18)$$

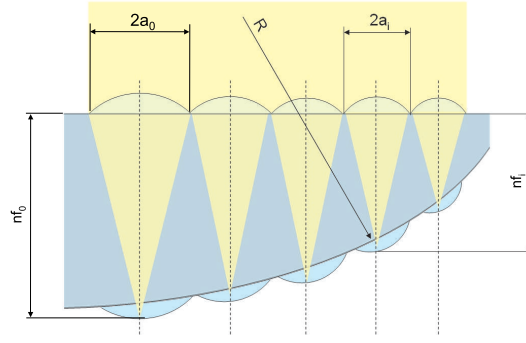


Figure 5.17: Geometry of a tandem cMLA with a plane and a curved surface. $2a_0$ - width of lens with index 0, $2a_i$ - width of lens with index i , f_0 - focal length of lens with index 0, f_i - focal length of lens with index i , n - index of refraction, R - radius of curvature of the macroscopic plano-convex cylindrical lens.

The distance x_i of the lens with index i following the largest microlens located at the vertex of the plano-convex cylindrical lens is given by

$$x_i = a_0 + 2 \sum_{n=1}^{i-1} a_n + a_i. \quad (5.19)$$

Inserting Eq. (5.19) into Eq. (5.18) leads to

$$f_i = f_0 - \frac{1}{n} \left(R - \sqrt{R^2 - \left(a_0 + 2 \sum_{o=1}^{i-1} a_o + a_i \right)^2} \right), \quad (5.20)$$

for the focal length of the i -th lens. The semi-width of the lens with index i can be calculated by

$$a_i = \frac{1}{4\eta^2 n^2 + 1} \left[\frac{f_0}{2\eta} (4\eta^2 n^2 - 1) - 2 \sum_{o=1}^{i-1} a_o - 2\eta n \left(R - \sqrt{R^2 - \frac{f_0^2}{\eta^2} + \frac{f_0 R}{\eta^2 n} + \left(\frac{R}{\eta n} - \frac{2f_0}{\eta} \right) \cdot 2 \sum_{o=1}^{i-1} a_o - \left(2 \sum_{o=1}^{i-1} a_o \right)^2} \right) \right]. \quad (5.21)$$

Using the same interface between the maths and wave optical simulation software, the far field intensity distributions were calculated now as a function of the radius of curvature of the macroscopic plano-convex cylindrical lens. The real structure was again approximated by a staircase setup in the simulation where the vertices of the second microlenses of the tandem array form the curved surface. In Fig. 5.19(a) the resulting far field intensity distributions are plotted for radii of curvature from 100mm down to 10mm. Even for the smallest curvature and hence smallest deviation of the lens parameters, good homogenization without hot spots can be generated. The degree of homogenization cannot be improved with increasing curvature. Contrary to the wedge configuration, the zeroth orders of all channels never coincide and

consequently no hot spots occur in the intensity distribution. The surface profile will be continuous in a real setup rather than being a staircase geometry used in the simulation. As shown above, in a wedge configuration each channel will have an additional but identical prism which leads to a deflection of all bundles leaving the array under the same angle. In a system using curved substrates, each channel will be deflected differently and will not overlap perfectly in focal plane of the Fourier lens. Therefore, the lenses of the second array must be decentered channel-wise in order to compensate the deflection behind the tandem array.

Random staircase Another opportunity is to use a substrate with non-continuously changing thickness (Fig. 5.18). The basic concept is to implement a stochastic phase plate into the setup in order to destroy the symmetry causing the otherwise occurring equidistant intensity peaks.⁶⁸ In contrast to previous proposed approaches, refractive instead of diffractive microlenses are used with the mentioned advantages in diffraction efficiency and stray light suppression. In addition, the setup will use a tandem configuration enabling an intensity distribution with the envelope of a top hat. In such a system, the arrangement of the microlenses is not determined by geometrical boundary conditions and its parameters are randomly chosen. Contrary to common stochastic MLA, the lenses do not impair each other and a constant f-number can be maintained. Therefore, the semi-width of the cell with index i is given by

$$a_i = \frac{f_0 [1 + rnd(\chi)]}{2\eta}, \quad (5.22)$$

where $rnd(\chi)$ stands for a random real number between 0 and χ and f_0 is the smallest focal length of the array. The focal lengths can be calculated using Eq. (2.28) or (2.29). The far field intensity distributions were calculated as a function of χ with values from zero to unity [Fig. 5.19(b)] for a system with minimum focal length $f_0=1\text{mm}$, $\text{NA}=0.05$, and 50 illuminated lenses. A regular array results in case of $\chi = 0$ and the periodic intensity pattern can be observed. Starting from the smallest χ of 0.01 good homogenization can be achieved. No hot spot will occur since there is no correlation between the microlens positions and the relative offset phases of the channels. The occurrence of hot spots in the intensity distribution is caused by constructive interference of all channels of the MLA. This can be avoided by randomly distributed offset phases due to different optical paths lengths. Here, a maximum phase shift of π is sufficient leading to difference in focal lengths of

$$\Delta f = \frac{\lambda}{2n(n-1)}. \quad (5.23)$$

Even if only small structure heights are required, the fabrication of such a substrate is rather difficult and the preferred fabrication method of reflow of photoresist for generating the microlenses cannot be used. Laser lithography is capable of directly writing of the structures on a planar substrate where the lenses will have pedestals of different height. The use of random instead of continuous functions lead to an inhomogeneous and not a chirped array and was

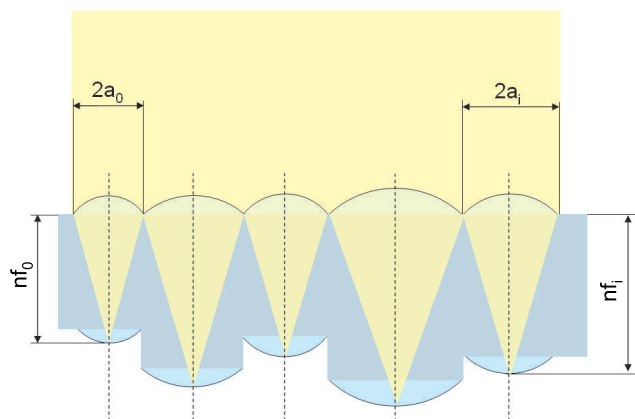


Figure 5.18: Schematic drawing of a tandem cMLA on a random staircase substrate. $2a_0$ - width of lens with index 0, $2a_i$ - width of lens with index i , f_0 - focal length of lens with index 0, f_i - focal length of lens with index i , n - index of refraction.

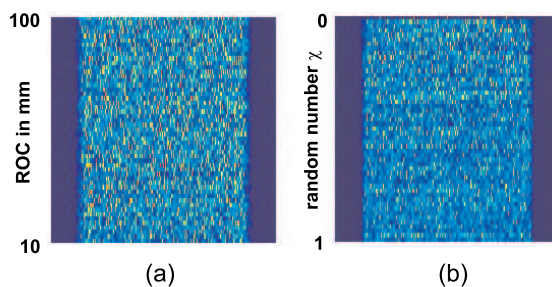


Figure 5.19: Calculated far field distribution of a fly's eye condenser using a tandem lens array on (a) curved surfaces and (b) using a random staircase as substrate. $NA=0.05$, number of illuminated lenses $N=50$, $\lambda=0.55\mu m$, index of refraction $n=1.52$ (a) The far field is plotted as a function of the radius of curvature (ROC) of the plano-convex substrate. (b) The far field is plotted as a function of the maximum random number χ .

mentioned in order to mark a direction of further research on this topic.

In conclusion, cMLAs used in a tandem configuration in fly's eye condenser systems for beam homogenization lead to an improved homogeneity of the intensity distribution in the focal plane of the Fourier lens. Because the array has a non-periodic structure, the equidistant intensity peaks occurring when using classical regular arrays can be avoided. All advantages of these types of homogenizers such as small wavelength dependence, low scattering, relaxed positioning tolerances, steep edges at the margins of the distribution, and independence of temporal fluctuations of the input intensity distribution can be preserved. Wedge configurations where both arrays are placed on plane substrates are of specific interest when taking established fabrication technologies - like reflow of photoresist - into account in order to transfer the designs into industrial applications rapidly. In the design of the wedge-type condensers, the deflection of the zeroth orders has to be respected requiring a minimum wedge angle which depends on the NA of the microlenses and the index of refraction of the wedge material. The orientation of the wedge with respect to the optical axis has to be observed because different

deflections of the beams occur which influence the design of the arrays.

Besides the extensively discussed wedge configurations, other substrate surface geometries can be used which are advantageous as far as homogenization is concerned. However, since their proper fabrication is more complex, this is connected with the improvement of the associated manufacturing techniques. The setup was illuminated by a single plane wave consequently with infinite coherence length in all simulations. Therefore, the results can be considered as a worst case approximation because in the real utilization the illumination might be synthesized by a finite angular spectrum of incident waves being partly coherent only. However, since the use of cMLAs improves the homogenization in the worst case consideration it is more than ever beneficial in case of more relaxed illumination conditions, too.

6 Conclusions and outlook

Several example systems for different applications based on cMLAs were designed, prototyped, and characterized to verify the new design possibilities offered by this type of micro-optical components. According to the proposed classification scheme, example devices for the individual and collective channel designs that lead to an improved degree of integration or enhanced optical performance parameters compared to the use of rMLAs were analyzed. The definition of the parameters of the individual lenses was done using analytical functions, numerical optimization techniques or a combination of the both based on fitted functions. In contrast to other non-regular arrays, these functions describing the cMLA are restricted to continuously differentiable ones. In consequence, common rMLAs are a part of the group of the cMLAs but with constant functions that are independent of the cell position.

The use of numerical optimization techniques is a hands-on approach to find the parameters of the cells. This is especially suitable if the number of lenses is small since otherwise the design process becomes inefficient. Two example systems assigned to the improvement of the degree of integration of a micro-optical system were discussed that verified the benefits of cMLAs. The major advantages in these application examples of using cMLAs are the compensation of fabrication tolerances and the reduction of the number of components of the system that finally leads to reduced fabrication costs without a decline of the optical performance.

In the case of a rather simple theoretical context describing the system, analytical functions can be used as executed by the example of the artificial apposition compound eye objective that uses a cMLA of ellipsoidal lenses for the channel-wise correction of the dominant off-axis-aberrations of astigmatism, field curvature, and distortion. The major advantage of this approach is the extremely short processing time needed for the calculation of the lens parameters of the entire array. This is especially relevant when dealing with arrays having a huge number of channels as for e.g. the ultra-thin camera objective with 16,900 cells. Even in this rather simple optical design task, the investments in finding the describing equations can become exhaustive. However, this approach is very efficient if a family of similar designs has to be developed. With the set of functions provided, the design of an entire cMLA for an ultra-thin camera is done in seconds for the given global objective parameters that are the number of channels in x- and y-direction, the paraxial focal length and the aperture diameter of the lens used at perpendicular incidence, the pitch of the photo receptors, and the diagonal field of view. The prototyped cMLA for the objective was manufactured by reflow of photoresist which requires a lithographic mask that must be chirped as well. Analytical functions were derived to convert the lens parameters into the mask design data that were subsequently imported to the self-written software tool. In conclusion, a solution was developed that generates the final mask layout by the set of global objective parameters which is very time efficient even for large arrays. Simultaneously, the architecture of the software tools is as open as possible and allows the generation of any cMLA that can be fabricated by reflow of photoresist.

Measurements of the imaging quality of the ellipsoidal microlenses verified the diffraction limited performance when used under their design angle. The individual compensation of the off-axis aberrations by using a cMLA with adapted cells enables ultra-thin camera systems with constant angular resolution at a field of view of 64° compared to 25° for systems based on regular arrays. This improvement goes along with an increase of the number of channels of the camera and enables the use of this imaging system for a variety of industrial applications that could not be addressed with conventional arrays. The successful prototyping of the artificial apposition compound eye objective with a large field of view is one the major achievements of this thesis. The further enhancement of the field of view will be explored in the future. Currently, a system with 110° is about to be fabricated.

The third approach of deriving the lens parameters of the microlens array combines the advantages of a flexible and possibly complex optical optimization based on numerical techniques and the fast calculation of arrays with a big number of channels. This can be considered as the most practically relevant solution due to its versatility and effectiveness. After the numerical optimization of a selection of significant cells, fitted functions are used to compute the parameters of all cells of the array. A planar integrated free-space optical interconnect having 660 optical channels was prototyped as an example system using cMLAs of off-axis lens segments. Laser lithography was employed in order to achieve a high fill factor of the microlens arrays and the elimination of aberrations. Versatile software tools were developed to translate the lens design into data readable by the laser exposure machine. An adapted writing and data preparation scheme was used in order to achieve sufficiently good surface roughness of the comparatively high lens elements of maximum $26.5\mu\text{m}$. A pixel-wise representation of the lens surface was used during the data preparation that led to undesirably huge files. This has to be improved in the future to simplify the transition between design and fabrication. Measurements of the prototyped cMLAs exhibited a large peak to valley deviation compared to the design profile of about $4\mu\text{m}$. This was caused by non-linear effects not being considered in the exposure procedure and a misalignment of the writing machine. In consequence, the measured coupling efficiencies when using singlemode fibers in the assembled interconnect are rather huge with 13 to 15dB. However, without using adapted cMLAs no coupling at all could have been established. Fabrication and alignment tolerances are less critical when using multimode fibers that led to coupling efficiencies of 1 to 3dB.

A fly's eye condenser based on a chirped tandem microlens array was examined as an example for a collective channel design where the interaction of all channels of the array has to be considered. Reflow of photoresist was selected as fabrication technique since cylindrical microlenses with a circular profile were required. Due to the limitations of the process, the arrays had to be produced on planar substrates. A configuration resulted where the two arrays are placed on a wedge. It was explained that this configuration acts like a prism structure but only for the zeroth orders of the lenses. These are deflected by an angle that depends on the material and the angle of the wedge and create a hot spot in the intensity distribution. If this deflection angle exceeds the divergence angle of the microlenses that is determined by their

numerical aperture, no hot spot will appear in the intensity distribution. Measurements obtained at first prototypes showed intensity distributions where the distance of adjacent peaks in the intensity distribution were closer by a factor of 7 to 14 compared to systems based on rMLA verifying the improvement of homogenization. Even simpler designs without the appearance of hot spots can be achieved when using fabrication techniques that are not restricted to planar substrates such as laser lithography on curved surfaces. However, beforehand these techniques have to be improved in order to yield commercially relevant micro-optical systems. The proposed fly's eye condenser based on cMLAs is especially interesting for homogenizing applications for short pulses since no additional dynamic elements such as rotating diffusers can be applied.

In summary, it was explained that chirped microlens arrays can be considered as an enhancement of the classical concept of microlens arrays which enables new degrees of freedom in the design of micro-optical systems in many applications. In order to take full advantage of these possibilities, especially the fabrication technologies for refractive elements with large sag heights and aspherical surface profiles have to be improved in the future. Promising candidates are direct writing techniques such as laser lithography and the introduced 2-photon polymerization.

References

- [1] D. Daly, *Microlens Arrays* (Taylor & Francis, London, 2001).
- [2] International Standards Organization, Geneva, Switzerland, *ISO 14880-1:2001 (E/F)* (2001).
- [3] K. Hill, “Aperiodic distributed-parameter waveguides for integrated optics,” *Appl. Opt.* **13**(8), 1853–1856 (1974).
- [4] T. Sales, “Structured microlens arrays for beam shaping,” *Optical Engineering* **42**(11), 3084–3085 (2003).
- [5] B. Stäger, M. Gale, and M. Rossi, “Replicated Micro-Optics for Automotive Applications,” in *Proc. of SPIE, Photonics in the automobile*, **5663**, 238–245 (2004).
- [6] M. Land and D.-E. Nilsson, *Animal Eyes*, Oxford Animal Biology Series (Oxford University Press, Oxford, United Kingdom, 2002).
- [7] G. Lippmann, “Epreuves reversibles donnant la sensation du relief,” *J. de Physique. Theorique et Appliquee* **7**, 821–825 (1908).
- [8] G. Lippmann, “Epreuves reversibles: Photographies integrales,” *Comptes-Rendus Academie des Sciences* **146**, 446–451 (1908).
- [9] H. Ives, “Optical properties of a Lippmann lenticulated sheet,” *J. Opt. Soc. Am.* **21**, 171–176 (1931).
- [10] K. Goetz, “Die optischen Übertragungseigenschaften der Komplexaugen von Drosophila,” *Kybernetik* **2**, 215–221 (1965).
- [11] J. Duparré, P. Dannberg, P. Schreiber, and A. Bräuer, “Micro-optically fabricated artificial apposition compound eye,” in *Proc. of Sensors and Camera Systems for Scientific, Industrial, and Digital Photography Applications V*, **5301**, 25–33 (2004).
- [12] J. Duparré, P. Dannberg, P. Schreiber, A. Bräuer, P. Nussbaum, F. Heitger, and A. Tünnermann, “Ultra-Thin Camera Based on Artificial Apposition Compound Eyes,” in *Proc. of 10th Microopt. Conf.*, ISBN: 3-8274-1603-5, E-2 (Elsevier, 2004).
- [13] A. Snyder, “Physics of Vision in Compound Eyes,” in *Handbook of sensory physiology*, 225–313 (Springer, 1977).
- [14] M. Land, “Compound eyes: old and new optical mechanisms,” *Nature* **287**, 681–686 (1980).

-
- [15] J. Duparré, P. Schreiber, A. Matthes, E. Pshenay-Severin, A. Bräuer, A. Tünnermann, R. Völkel, M. Eisner, and T. Scharf, “Microoptical telescope compound eye,” *Opt. Exp.* **13**(3), 889–903 (2005).
- [16] J. Duparré and F. Wippermann, “Micro-optical artificial compound eyes,” *Bioinspiration and Biomimetics* **1**, R1–R16 (2006).
- [17] W. Hugle, R. Dändliker, and H. Herzig, “Lens array photolithography,” *GB Pat. Appl.* 9224080.3 (1992).
- [18] R. Dändliker, S. Gray, F. Clube, H. Herzig, and R. Völkel, “Non-conventional fabrication methods for photolithography,” *Microelectron. Eng.* **27**, 205–211 (1995).
- [19] M. Kawazu and Y. Ogura, “Application of gradient-index fiber arrays to copying machines,” *Appl. Opt.* **19**(7), 1105–1112 (1980).
- [20] D. Gabor, “Improvements in or relating to optical systems composed of lenticules,” *Pat. UK* 541,753 (1941).
- [21] D. Gabor, “Microscopy by reconstructed wave-fronts,” *Proc. Roy. Soc. A* **197**, 454–487 (1949).
- [22] R. Ng, M. Levoy, M. Brédif, G. Duval, M. Horowitz, and P. Hanrahan, “Light Field Photography with a Hand-held Plenoptic Camera,” *Stanford Tech Report CTSR 2005-02* (2005).
- [23] J. Duparré and R. Völkel, “Novel Optics/Micro-Optics for Miniature Imaging Systems,” in *Proc. of SPIE, Photonics in Multimedia*, **6196**, 619607 (2006).
- [24] H. Machida, J. Nitta, A. Seko, and H. Kobayashi, “High-efficiency fiber grating for producing multiple beams of uniform intensity,” *Appl. Opt.* **23**(2), 330–332 (1984).
- [25] X. Deng, X. Liang, Z. Chen, W. Yu, and R. Ma, “Uniform illumination of large targets using a lens array,” *Appl. Opt.* **25**(3), 377–381 (3).
- [26] N. Streibl, U. Nölscher, J. Jahns, and S. Walker, “Array generation with lenslet arrays,” *Appl. Opt.* **30**, 2793–2742 (1991).
- [27] A. Lohmann, “Array illuminators and complexity theory,” *Opt. Comm.* **89**, 167–172 (1992).
- [28] S. Sinzinger and J. Jahns, *Microoptics* (Wiley–VCH, Weinheim, 1999).
- [29] H. Naumann and G. Schröder, *Bauelemente der Optik - Taschenbuch der technischen Optik*, 6th ed. (Hanser, München, 1992).

- [30] F. Dickey and S. Holswade, *Laser beam shaping: Theory and Techniques* (Marcel Deller, New York, 2000).
- [31] N. Kashima, *Passive optical components for optical fiber transmission* (Artech House, Boston, Massachusetts, USA, 1995).
- [32] R. Göring, F. Wippermann, and K. Kubitz, “Hybrid MOEMS approaches for fiber optic switches and switch matrices,” in *Proc. of SPIE, MOEMS and Miniaturized Systems*, **4178**, 59–66 (2000).
- [33] S. Sinzinger and J. Jahns, “Integrated micro-optical imaging system with a high interconnection capacity fabricated in planar optics,” *Appl. Opt.* **36**(20), 4729–4735 (1997).
- [34] N. Streibl, R. Völkel, J. Schwider, P. Habel, and N. Lindlein, “Parallel optoelectronic interconnections with high packaging density through a light guiding plate using grating couplers and field lenses,” *Opt. Comm.* **99**, 167–171 (1992).
- [35] Y. Li, T. Wang, and R. Linke, “VCSEL-array-based angle-multiplexed optoelectronic crossbar interconnects,” *Appl. Opt.* **35**(8), 1282–1295 (1996).
- [36] Y. Ishihara and K. Tangigaki, “A high photosensitivity IL-CCD image sensor with monolithic resin lens array,” in *Proc. of IEEE, Int. Electron Devices Meeting*, **29**, 497–500 (1983).
- [37] N. Gordon, C. Jones, and D. Purdy, “Application of microlenses to infrared detector arrays,” *Infrared Phys.* **31**(11), 599–604 (1991).
- [38] E. Watson, “Analysis of beam steering with decentered microlens,” *Opt. Eng.* **32**(11), 2665–2670 (1993).
- [39] S. Glöckner, R. Göring, and T. Poßner, “Micro-opto-mechanical beam deflectors,” *Opt. Eng.* **36**(5), 1339–1345 (1997).
- [40] J. Duparré and R. Göring, “Numerical wave optical analysis of microlens array telescopes and comparison with experimental results,” *Appl. Opt.* **42**(19), 3992–4001 (2003).
- [41] R. Shack and B. Platt, “Production und use of a lenticular Hartmann screen,” *J. Opt. Soc. Am.* **61**(5), 656 (1971).
- [42] R. Lane and M. Tallon, “Wave-front reconstruction using a Shack-Hartmann sensor,” *Appl. Opt.* **31**(32) (1992).
- [43] S. Rotich, J. Smith, A. Evans, and A. Brunnschweiler, “Micromachined thin solar cells with a novel light trapping scheme,” *J. Micromech. Microeng.* **8**, 134–137 (1998).
- [44] W. Tomlinson, “Applications of GRIN-rod lenses in optical fiber communication systems,” *Appl. Opt.* **19**(7), 1127–1138 (1980).

- [45] R. E. Wagner and J. Cheng, "Electrically controlled optical switch for multimode fiber applications," *Appl. Opt.* **19**(17), 2921–2925 (1980).
- [46] K. Hamanaka and H. Koshi, "An artificial compound eye using a microlens array and its application to scale-invariant processing," *Opt. Rev.* **3**(4), 264–268 (1996).
- [47] N. Borrelli, *Microoptics Technology: Fabrication and Applications of lens and arrays and devices* (Marcel Dekker, New York, 1999).
- [48] H. Herzig, *Micro-Optics – Elements, systems and applications* (Taylor and Francis, Ltd., London, United Kingdom, 1997).
- [49] T. Saito, "Machining of optics: an introduction," *Appl. Opt.* **14**(8), 1773–1776 (1975).
- [50] C. Blough, M. Rossi, S. Mack, and R. Michaels, "Single-point diamond turning and replication of visible and near-infrared diffractive optical elements," *Appl. Opt.* **36**(20), 4648–4654 (1997).
- [51] J. Duparré, P. Schreiber, P. Dannberg, T. Scharf, P. Pelli, R. Völkel, H.-P. Herzig, and A. Bräuer, "Artificial compound eyes - different concepts and their application to ultra flat image acquisition sensors," in *Proc. of MOEMS and Miniaturized Systems IV*, **5346**, 89–100 (2004).
- [52] J. Duparré, P. Dannberg, P. Schreiber, A. Bräuer, and A. Tünnermann, "Artificial apposition compound eye fabricated by micro-optics technology," *Appl. Opt.* **43**(22), 4303–4310 (2004).
- [53] E. Hecht, *Optics* (Addison-Wesley Publishing Co., Reading, Massachusetts, USA, 1987).
- [54] C. Hofmann, *Die Optische Abbildung*, 1st ed. (Geest und Portig, Leipzig, 1980).
- [55] J. Duparré, "Microoptical Artificial Compound Eyes," Ph.D. thesis, Friedrich-Schiller-Universität Jena (2005).
- [56] A. Gullstrand, "Beitrag zur Theorie des Astigmatismus," *Skand. Arch. Physiol.* **2**, 269–359 (1889).
- [57] H. Hinton, "Architectural considerations for photonic switching networks," *IEEE J. Selected Areas Commun.* **6**, 1209–1226 (1988).
- [58] A. Lohmann, "Image formation of dilute arrays for optical information processing," *Opt. Comm.* **86**, 365–370 (1991).
- [59] F. McCormick, "Free-space Optical Interconnection Techniques and Issues," in *Photonics in Switching II*, J. Midwinter, ed. (Academic Press, Boston, Massachusetts, 1993).

- [60] S. Sinzinger and J. Jahns, "Variations of hybrid imaging concept for optical computing applications," *Optical Computing OSA Technical Digest Series* **10**, 183–185 (1995).
- [61] Y. Liu, B. Robertson, D. Plant, H. Hinton, and W. Robertson, "Design and characterization of a microchannel optical interconnect for optical backplanes," *Appl. Opt.* **36**, 3127–3141 (1997).
- [62] D. Kuchta, J. Crow, P. Pepeljugoski, K. Stawiasz, J. Trehwella, D. Booth, W. Natio-nand, C. DeCusatis, and A. Muszynski, "Low cost 10 gigabit/s optical interconnects for parallel processing," in *Proc. of Massively Parallel Processing, 1998, Las Vegas*, 210–215 (Fifth International Conference, 1998).
- [63] H. Kogelnik and T. Li, "Laser Beams and Resonators," *Appl. Opt.* **5**, 1550–67 (1966).
- [64] J. Hammer and C. Neil, "Observations and theory of high power butt coupling to LiNbO₃-type waveguides," *IEEE J. Quant. Electr.* **18**, 1751–1758 (1982).
- [65] W. Karthe and R. Mueller, *Integrierte Optik*, 1st ed. (Akademische Verlagsgesellschaft Geest und Portig, Leipzig, 1991).
- [66] A. Yariv, "Coupled Mode Theory for Guided-Wave Optics," *IEEE J. Quant. Electr.* **9**, 919–933 (1973).
- [67] W. Joyce and B. DeLoach, "Alignment of Gaussian Beams," *Applied Optics* **23**, 4187–4196 (1984).
- [68] C. Kopp, L. Ravel, and P. Meyrueis, "Efficient beam shaper homogenizer design combining diffractive optical elements, microlens array, and random phase plate," *J. Opt. A: Pure Appl. Opt.* **1**, 398–403 (1999).
- [69] O. Bryngdahl, "Geometrical transformations in optics," *JOSA* **64**, 1092–1099 (1974).
- [70] J. Cederquist and A. Tai, "Computer-generated holograms for geometric transformations," *Appl. Opt.* **23**, 3099–3104 (1984).
- [71] J. Hoffnagle and C. Jefferson, "Design and performance of a refractive optical system that converts a Gaussian to a flattop beam," *Appl. Opt.* **39**(30), 5488–5499 (2000).
- [72] G. Swanson and W. Veldkamp, "Diffractive optical elements for use in infrared systems," *Opt. Eng.* **28**, 605–608 (1989).
- [73] F. Nikolajeff, S. Hard, and B. Curtis, "Diffractive microlenses replicated in fused silica for excimer laser-beam homogenizing," *Appl. Opt.* **36**, 8481–8489 (1997).
- [74] H. Aagedal, M. Schmid, S. Egner, J. Müller-Quade, T. Beth, and F. Wyrowski, "Analytical beam shaping with application to laser-diode arrays," *J. Opt. Soc. Am. A: Pure Appl. Opt.* **14**, 1549–1553 (1997).

- [75] I. Harder, M. Lano, N. Lindlein, and J. Schwider, "Homogenization and beam shaping with microlens arrays," in *Proc. of SPIE, Photon Management*, **5456**, 99–107 (2004).
- [76] N. Lindlein, "Wellen- und strahlenoptische Simulation von Wabenkondensoren," in *Proc. of DGaO* (2004).
- [77] I. Harder, M. Lano, N. Lindlein, and J. Schwider, "Eigenschaften und Grenzen von Homogenisatoren aus Mikrolinsenarrays," in *Proc. of DGaO* (2004).
- [78] A. Büttner and U. D. Zeitner, "Wave optical analysis of light-emitting diode beam shaping using microlens arrays," *Opt. Eng.* **4**, 2393–2401 (2002).
- [79] P. Schreiber, S. Kudaev, P. Dannberg, and U.-D. Zeitner, "Homogeneous LED-illumination using microlens arrays," in *Proc. of SPIE, Nonimaging optics and efficient illumination systems II , San Diego*, **5942**, 59,420K.1–59,420K.9 (2005).
- [80] J. Goodman, *Introduction to Fourier Optics* (McGraw–Hill, New York, 1968).
- [81] M. Born and E. Wolf, *Principles of optics*, 7th ed. (Cambridge University Press, Cambridge, United Kingdom, 1999).
- [82] F. Wippermann, J. Duparré, P. Schreiber, and P. Dannberg, "Design and fabrication of a chirped array of refractive ellipsoidal micro-lenses for an apposition eye camera objective," in *Proc. of Optical Design and Engineering II*, **5962**, 59622C (2005).
- [83] J. Duparré, F. Wippermann, P. Dannberg, and A. Reimann, "Chirped arrays of refractive ellipsoidal microlenses for aberration correction under oblique incidence," *Opt. Exp.* **13**(26), 10,539–10,551 (2005).
- [84] D. Pastor, J. Capmany, D. Ortega, V. Tatay, and J. Marti, "Design of Apodized Linearly Chirped Fiber Gratings for Dispersion Compensation," *J. of Lightw. Techn.* **14**(11), 2581–2588 (1996).
- [85] K. Hill and G. Meltz, "Fiber Bragg Grating Technology," *J. of Lightw. Techn.* **15**(8), 1263–1276 (1997).
- [86] K. Ennser, M. Zervas, and R. Laming, "Optimization of Apodized Linearly Chirped Fiber Gratings for Optical Communications," *IEEE J. of Quant. Electr.* **34**(5), 770–778 (1998).
- [87] P. Schreiber, P. Dannberg, B. Hofer, and E. Beckert, "Chirped microlens arrays for diode laser circularization and beam expansion," in *Proc. of SPIE*, **5876**, 176–183 (2005).
- [88] F. Wippermann, J. Duparré, and P. Schreiber, "Application of chirped microlens arrays for aberration compensation and improved system integration," in *Proc. of SPIE*, **6289**, 628915 (2006).

- [89] F. Wippermann, D. Radtke, M. Amberg, and S. Sinzinger, “Integrated free-space optical interconnect fabricated in planar optics using chirped microlens arrays,” *Opt. Exp.* **14**(22), 10,765–10,778 (2006).
- [90] F. Wippermann, P. Dannberg, A. Bräuer, and S. Sinzinger, “Improved homogenization of fly’s eye condenser setups under coherent illumination using chirped microlens arrays,” in *Proc. of SPIE, MOEMS and Miniaturized Systems VI*, **6466**, 64660R (2007).
- [91] F. Wippermann, U. Zeitner, P. Dannberg, A. Bräuer, and S. Sinzinger, “Beam homogenizers based on chirped microlens arrays,” *Opt. Exp.* **15**(10), 6218–6231 (2007).
- [92] N. Lindlein, F. Simon, and J. Schwider, “Simulation of micro-optical array systems with RAYTRACE,” *Opt. Eng.* **37**(6), 1809–1816 (1998).
- [93] N. Lindlein, “Simulation of micro-optical systems including microlens arrays,” *J. Opt. A: Pure Appl. Opt.* **4**, S1–S9 (2002).
- [94] Zemax Development Corp., Bellevue, Washington, USA, *ZEMAX User’s Manual* (2006).
- [95] Lighttrans GmbH, Jena, Germany, *Virtual Lab 3.1 User’s Manual* (2006).
- [96] M. Laikin, *Lens Design*, 2nd ed. (Marcel Dekker, Monticello, New York, 1995).
- [97] W. Smith, *Modern Optical Engineering: The Design of Optical Systems*, 2nd ed. (McGraw–Hill, New York, 1990).
- [98] I. Bronstein, K. Semandjajew, G. Musiol, and H. Mühlig, *Taschenbuch der Mathematik* (H. Deutsch, Frankfurt, 1995).
- [99] E. Rawson, D. Herriot, and J. McKenna, “Analysis of refractive index distributions in cylindrical, graded-index glass rods (GRIN rods) used as image relays,” *Appl. Opt.* **9**, 753–759 (1970).
- [100] K. Naessens, H. Ottevaere, R. Baets, P. van Daele, and H. Thienpont, “Direct writing of microlenses in polycarbonate with excimer laser ablation,” *Appl. Opt.* **42**(31), 6349–6359 (2003).
- [101] P. Nussbaum, R. Völkel, H. Herzig, M. Eisner, and S. Haselbeck, “Design, fabrication and testing of microlens arrays for sensors and microsystems,” *Pure Appl. Opt.* **6**, 617–636 (1997).
- [102] Z. Popovich, R. Sprague, and G. Conell, “Technique for monolithic fabrication of microlens arrays,” *Appl. Opt.* **27**(7), 1281–1284 (1988).
- [103] D. Daly, R. Stevens, M. Hutley, and N. Davies, “The manufacture of microlenses by melting photoresist,” *J. Meas. Sci. Technol.* **1**, 759–766 (1990).

- [104] M. Hutley, P. Savander, and M. Schrader, "The use of microlenses for making spatially variant optical interconnections," *Pure Appl. Opt.* **1**, 337–346 (1992).
- [105] Z. Liao, V. Diadiuk, J. Walpole, and D. Mull, "Gallium phosphide microlenses by mass transport," *Appl. Phys. Lett.* **55**, 2434–2440 (1989).
- [106] J. Swenson, R. Fields, and M. Abraham, "Enhanced mass-transport smoothing of f/0.7 GaP microlenses by the use of sealed ampoules," *Appl. Phys. Lett.* **66**, 1304–1306 (1995).
- [107] N. Borrelli, D. Morse, R. Bellmann, and W. Morgan, "Photolytic technique for producing microlenses in photosensitive glass," *Appl. Opt.* **24**, 2520 (1985).
- [108] M. Kufner, S. Kufner, M. Frank, J. Moisel, and M. Testorf, "Microlenses in PMMA with high relative aperture: a parameter study," *Pure Appl. Opt.* **2**, 9–19 (1993).
- [109] D. MacFarlane, V. Narayan, J. Tatum, W. Cox, T. Chen, and D. Hayes, "Microjet fabrication of microlens arrays," *IEEE Photon. Technol. Lett.* **6**, 1112–1114 (1994).
- [110] V. Guyenot, "Herstellung von Mikrolinsen durch Klebstofftropfen-Applikation," *Jahresbericht Fraunhofer Institut Angewandte Optik und Feinmechanik* 44–46 (1996).
- [111] M. Gale, G. Lang, J. Raynor, and H. Schuetz, "Fabrication of microoptical elements by laser beam writing in photo resist," in *Proc. of SPIE*, **1506**, 65–70 (1991).
- [112] M. Gale, M. Rossi, R. Kunz, and G. Bona, "Laser writing and replication of continuous-relief Fresnel microlenses," *OSA Technical Digest Series: Diffractive Optics* **11**, 306–309 (1994).
- [113] K. Brenner and J. Jahns, *Microoptics: From Technology to Applications*, 97 of *Springer Series in Optical Sciences*, ISBN 978-0-387-20980-7 ed. (Springer-Verlag, Heidelberg, 2004).
- [114] U.-D. Zeitner and E.-B. Kley, "Advanced lithography for micro-optics," in *Proc. of SPIE*, **6290**, 629,009–1 – 629,009–8 (2006).
- [115] J. Serbin, A. Egbert, A. Ostendorf, B. Chichkov, R. Houbertz, G. Domann, J. Schulz, C. Cronauer, L. Fröhlich, and M. Popall, "Femtosecond laser-induced two-photon polymerization of inorganic organic hybrid materials for applications in photonics," *Opt. Lett.* **28**, 301–303 (2003).
- [116] R. Guo, S. Xiao, X. Zhai, J. Li, A. Xia, and W. Huang, "Micro lens fabrication by means of femtosecond two photon photopolymerization," *Opt. Exp.* **14**(2), 810–816 (2006).
- [117] K. Mersereau, C. Nijander, W. Townsend, R. Crisci, A. Feldblum, and D. Daly, "Design, fabrication and testing of refractive microlens arrays," in *Digest of Top. Meet. on Microlens Arrays at NPL, Teddington*, M. C. Hutley, ed., **2**, 60–64 (1993).

- [118] L. Erdmann and D. Efferenn, "Technique for monolithic fabrication of silicon microlenses with selectable rim angles," *Opt. Eng.* **36**, 1094–1098 (1997).
- [119] A. Schilling, R. Merz, C. Ossmann, and H. Herzig, "Surface profiles of reflow microlenses under the influence of surface tension and gravity," *Opt. Eng.* **39**(8), 2171–2176 (2000).
- [120] S. Haselbeck, H. Schreiber, J. Schwider, and N. Streibl, "Microlenses fabricated by melting a photoresist on a base layer," *Opt. Eng.* **32**(6), 1322–1324 (1993).
- [121] R. Völkel, H. Herzig, P. Nussbaum, and R. Dändliker, "Microlens array imaging system for photolithography," *Opt. Eng.* **35**(11), 3323–3330 (1996).
- [122] M. Eisner, N. Lindlein, and J. Schwider, "Making diffraction limited refractive microlenses of spherical and elliptical form," in *Digest of Top. Meet. on Microlens Arrays at NPL, Teddington*, M. C. Hutley, ed., **13**, 39–41 (1997).
- [123] C. Carey, D. Godwin, P. Poon, D. Daly, D. Selviah, and J. Midwinter, "Astigmatism in ellipsoidal and spherical photoresist microlenses used at oblique incidence," in *Digest of Top. Meet. on Microlens Arrays at NPL, Teddington*, M. C. Hutley, ed., **2**, 65–68 (1993).
- [124] F. Wippermann, D. Radtke, U. Zeitner, J. Duparré, A. Tünnermann, M. Amberg, S. Sinzinger, C. Reinhardt, A. Ovsianikov, and B. Chichkov, "Fabrication technologies for chirped refractive microlens arrays," in *Proc. of SPIE, Optics and Photonics, Current Developments in Lens Design and Optical Engineering VII*, **6288**, 62880O (2006).
- [125] Autodesk, Inc., San Rafael, California, USA, *AutoCAD 14* (1997).
- [126] J. Buchanan, "http://www.buchanan1.net/stream_description.shtml," (1996).
- [127] Fraunhofer IPMS, Dresden, Germany, *SE-Benutzerhandbuch, SE-Layouteditor*, Version 7.1 ed. (2005).
- [128] M. Gale, G. Lang, J. Raynor, H. Schütz, and D. Prongué, "Fabrication of kinoform structures for optical computing," *Appl. Opt.* **31**, 5712–5715 (1992).
- [129] T. Dresel, S. Frank, U. Krackhardt, J. Schwider, N. Streibl, and A. Wehrhahn, "Fabrication of Diffractive Optical Elements by Laser-Lithography," in *Proc. of SPIE*, **1983**, 668 (1993).
- [130] Heidelberg Instruments Mikrotechnik GmbH, Heidelberg, Germany, *DWL 400* (2004).
- [131] micro resist technology GmbH, Berlin, Germany, *Ormocer* (2006).
- [132] M. Popall, J. Kappel, J. Schulz, and H. Wolter, "Ormocers, inorganic-organic polymer materials for applications in micro systems technology," *Microsystem Technologies '94* 271–279 (1994).

- [133] K. Haas and K. Rose, "Hybrid inorganic-organic polymers with nanoscale building blocks: precursors, processing, properties and applications," *Rev. Adv. Mater. Sci.* **5**, 47–52 (2003).
- [134] Micromap Corp., Tucson, Arizona, USA, *Micromap 512* (1999).
- [135] Hitachi, Ltd., Tokyo, Japan, *HL6319/20G ALGaInP Laser Diodes* (2006).
- [136] Thorlabs, Inc., Newton, New Jersey, USA, *Thorlabs Catalog Vol. 17* (2007).
- [137] Coherent, Inc., Santa Clara, California, USA, *LaserCam IIID Instruction Manual* (2005).
- [138] M. Hutley, R. Hunt, R. Stevens, and P. Savander, "The moiré magnifier," *Pure Appl. Opt.* **3**, 133–142 (1994).
- [139] R. Stevens, "Optical inspection of periodic structures using lens arrays and moiré magnification," *Imaging Sci. J.* **47**, 173–179 (1999).
- [140] H. Kamal, R. Völkel, and J. Alda, "Properties of moiré magnifiers," *Opt. Eng.* **37**(11), 3007–3014 (1998).
- [141] N. Lindlein, S. Haselbeck, and J. Schwider, "Simplified Theory for Ellipsoidal Melted Microlenses," in *Digest of Top. Meet. on Microlens Arrays at NPL, Teddington*, **5**, 7–10 (1995).
- [142] L. Wittig and E. Kley, "Approximation of refractive micro optical profiles by minimal surfaces," in *Proc. of Micromachine Technology for Diffractive and Holographic Optics*, S. H. Lee and J. A. Cox, eds., SPIE **3879**, 32–38 (1999).
- [143] P.-F. Rüedi, P. Heim, F. Kaess, E. Grenet, F. Heitger, P.-Y. Burgi, S. Gyger, and P. Nussbaum, "A 128 x 128 Pixel 120-dB Dynamic-Range Vision-Sensor Chip for Image Contrast and Orientation Extraction," *IEEE J. Solid-State Circ.* **38**(12), 2325–2333 (2003).
- [144] P. Dannberg, G. Mann, L. Wagner, and A. Bräuer, "Polymer UV-molding for micro-optical systems and O/E- integration," in *Proc. of SPIE, Micromachining for Micro-Optics*, **4179**, 137–145 (2000).
- [145] J. Duparré, P. Dannberg, P. Schreiber, A. Bräuer, and A. Tünnermann, "Thin compound eye camera," *Appl. Opt.* **44**(15), 2949–2956 (2005).
- [146] Taylor Hobson Ltd., Leicester, United Kingdom, *Form Talysurf Series 2 PGI+* (2003).
- [147] J. Jahns and A. Huang, "Planar integration of free space optical components," *Appl. Opt.* **28**, 1602–1605 (1989).

-
- [148] J. Jahns and B. Acklin, “Integrated planar optical imaging system with high interconnection density,” *Opt. Lett.* **18**, 1594–1596 (1993).
- [149] J. Jahns, “Planar packaging of free space optical interconnections,” in *Proc. of the IEEE*, **82**, 1623–1631 (1994).
- [150] R. Kingslake, R. Shannon, and J. Wyant, *Applied Optics and Optical Engineering*, 11 (Academic Press, New York, USA, 1992).
- [151] Schott, Mainz, Germany, *Borofloat 33* (2006).
- [152] A. Wei, M. Jarczyński, M. Gruber, J. Jahns, and H. Shieh, “Plastic planar-integrated free-space optical interconnector,” in *Proc. of 12th Microoptics Conference (MOC’06), Seoul, Korea* (2006).
- [153] R. Heming, J. Jahns, M. Gruber, L. Wittig, and E. Kley, “Combination of binary and analog lithography to fabricate efficient planar-integrated free-space optical interconnects,” in *Proc. of DGaO*, **106**, 36–37 (2005).
- [154] International Standards Organization, Geneva, Switzerland, *ISO 13694:2000 (E)* (2000).
- [155] Norland Products, Inc, Cranbury, New Jersey, USA, *Norland UV Adhesives* (2004).

A Symbols and abbreviations

a	Semi-width of a cylindrical microlens
A	Radius of a microlens
A_0	Field amplitude of a Gaussian beam
A_{\cap}	Cross section area of a lens
A_R	Cross section area of a cuboid
a_s	Axis of an ellipse at the rim of a lens laying in the sagittal plane of an anamorphic lens
A_S	Area of a sector of a circle
a_t	Axis of an ellipse at the rim of a lens laying in the tangential plane of an anamorphic lens
$a_{x/y}$	Distance of adjacent resolvable points in the object plane in x- and y-direction
b	Burst width of a signal
BFL	Back focal length
b_R	Width of a resist cuboid
CCD	Charge coupled device
$cMLA$	Chirped microlens array
$CMOS$	Complementary Metal Oxide Semiconductor
d	Diameter of a photo receptor
D	Diameter of a lens aperture
d_{Airy}	Extension of a diffraction limited intensity distribution in the focal plane of a lens
d_{fiber}	Lateral displacement between the waist and the facet of a singlemode fiber
d_e	Normalization value for the lateral displacement between two Gaussian bundles
d_{im}	Distance between the image space waist and a lens
d_{ob}	Distance between the object space waist and a lens
d_{PSF}	Extension of an intensity distribution in the focal plane of a lens
d_q	Ratio of the period length p_a to the burst width b of a signal
f	Focal length of a lens
F	Focal length of a Fourier lens
FA	Fast axis of a laser diode
FOV	Field of view
$F(x, y)$	Electrical field distribution
$FWHM$	Full width at half maximum
GB	Gigabyte
h_L	Vertex height of a lens

h_R	Height of a resist cuboid
(i, j)	Cell position index
(i_0, j_0)	Position index of the reference cell
<i>ISO</i>	International Standards Organization
k	Wave number
k_q	Factor for the adaption of the quality factor q
k_s	Conical constant of an anamorphic lens in the sagittal plane
k_t	Conical constant of an anamorphic lens in the tangential plane
L	Distance between the object plane and the ultra-thin camera objective
M	Number of sampling points
m	Mean value
<i>MLA</i>	Microlens array
n	Index of refraction in the object space
n'	Index of refraction in the image space
\vec{n}	Normal vector of the tangential plane of an ellipsoidal lens
N	Number of lenses
N_x	Number of lenses in x-direction
N_y	Number of lenses in y-direction
<i>NA</i>	Numerical aperture
o	Summation index
<i>OPD</i>	Optical path difference
p	Pitch
$\vec{p}_{i,j}$	Position vector of the lens center of the lens with index (i,j)
p_a	Period length of a signal
$P_{i,j}$	Decenter of the cell with index (i,j)
p_{lens}	Pitch of lenses
$p_{pinhole}$	Pitch of pinholes
P_x	Pitch of lenses in x-direction
P_y	Pitch of lenses in y-direction
$P_{x_{i,j}}$	Component of the decenter in x-direction of the cell with index (i,j)
$P_{y_{i,j}}$	Component of the decenter in y-direction of the cell with index (i,j)
<i>PSF</i>	Point spread function
<i>PV</i>	Peak to valley
q	Quality factor
r	Radial distance
R	Radius of curvature
<i>ROC</i>	Radius of curvature
r_0	Distance from the first row of the array to the symmetry center in y-direction

$rMLA$	regular microlens array
$rnd(\chi)$	Random real number between 0 and χ
ROC	Radius of curvature
r_{ref}	Aperture diameter of the reference cell
R_s	Sagittal radius of curvature of an anamorphic lens
R_t	Tangential radius of curvature of an anamorphic lens
s'_0	Paraxial back focal length
s_s	Sagittal object distance
s'_s	Sagittal back focal length
s_t	Tangential object distance
s'_t	Tangential back focal length
SA	Slow axis of a laser diode
$T(y')$	Transmission function
$u(y)$	Electric field distribution
v	Amplitude value
w_{norm}	Ratio of the aperture width to the diffraction limited spot diameter in the focal plane of first microlens of a tandem array
$W(x, y)$	Electrical field distribution
$W_{x/y}$	Width of the unit cell in x/y-direction
x, y, z	Coordinates in the Cartesian space
x_i	Lateral coordinate of the vertex position of a cylindrical microlens
y, y'	Coordinate axes at different propagation distances in a fly's eye condenser setup
y''	Coordinate in the Fourier plane of a tandem array fly's eye condenser
Z	Fresnel number
z'	Axial distance between the waist and the facet of a singlemode fiber
α	Wedge angle
α_c	Critical angle
γ	Cone angle of a focused bundle
γ_{LP}	Number of resolvable line pairs
δ	Deflection angle
Δ	Picht's operator
Δf	Difference in focal lengths
$\Delta\Phi$	Interommatidial angle
$\Delta\varphi$	Acceptance angle
η	F-number (f/#)
η_a	General coupling efficiency
$\eta_{d_{fiber}}$	Coupling efficiency accounting for lateral displacement

η_G	Coupling efficiency of two Gaussian beams or modes, accounting for axial displacement
η_{total}	Coupling efficiency of two Gaussian beams or modes, accounting for axial, lateral, and angular displacements
$\eta_{\phi_{fiber}}$	Coupling efficiency accounting for angular displacement
θ	Angle of incidence
ϑ	Divergence of a Gaussian beam
Θ	Orientation angle
κ	Number of coefficients
λ	Wavelength
Λ	Decenter of a cylindrical lens
μ	Numerical aperture
ν, ν'	Spatial frequency
σ	Chief ray angle in the object space
σ'	Chief ray angle in the image space
σ_{dev}	Standard deviation
σ_{max}	Maximum chief ray angle (diagonal FOV)
σ_{max_x}	Maximum chief ray angle in x-direction (horizontal FOV)
σ_{max_y}	Maximum chief ray angle in y-direction (vertical FOV)
τ_a	Coupling efficiency without tilt or offset
ν_S	Shrinkage factor
φ	Half opening angle
ϕ_e	Normalization value for the angular displacement between two Gaussian bundles
ϕ_{fiber}	Angular displacements between waist and facet of a singlemode fiber
ϕ_{FOV}	Angular extension of the field of view
Φ_l	Parametric function
χ	Real number
$\Psi_0(x, y)$	Surface profile of the unit cell
$\Psi_{i,j}(x, y)$	Surface profile of the cell with index (i,j)
ω_0	Waist of a Gaussian Beam
$\omega_{01,2}$	Waists of Gaussian beams
ω_{im}	Image space waist
ω_{ob}	Object space waist
$\omega_{1,2}$	Beam radii of Gaussian beams
$\omega(z)$	Beam radius of a Gaussian beam

B Acknowledgements

First of all I would like to thank Prof. Stefan Sinzinger for supervising my thesis, the helpful discussions and his impulses on new ideas and directions of my work.

I owe special thanks to Dr. Andreas Bräuer for offering the opportunity to work on my research topics and all his academic and individual support. I consider myself lucky for having the chance to be part of the research team at the department “Microoptical Systems” of the Fraunhofer Institute for Applied Optics and Precision Engineering (IOF), Jena, where I was allowed to expand my knowledge far beyond the scope of my thesis. Besides the scientific and technological expertise of my colleagues that I benefited from, I especially appreciated the always open, fair, and hands-on atmosphere which made work not only challenging and interesting but a real pleasure.

I would like to thank Dr. Peter Schreiber and Dr. Uwe-Detlef Zeitner for the many fruitful discussions and all of their support related to optics design. I specially thank Dr. Jacques Duparré for the many talks on the ultra-thin camera system. My grateful appreciation goes to Dr. Peter Dannberg and all combatants of the “technology task force” (Sylke Kleinle, Antje Oelschläger, Daniela Radtke, Gisela Wagener, Tino Benkenstein, Bernd Höfer, Gilbert Leibelng, Ralf Rosenberger) for their invaluable contributions to bringing the idea of chirped microlens arrays into reality.

I am especially thankful for the advice and support of Dr. Rolf Göring who introduced me to the research field of microoptics years ago and always encouraged me take the next step.

Finally, I would like to thank my family and my friends who always supported me in my plans and ideas and for them being a source of recreation and a lifetime backup. Sláinte and a pint of Guinness to your health.

C Erklärung

Ich versichere, dass ich die vorliegende Arbeit ohne unzulässige Hilfe Dritter und ohne Benutzung anderer als der angegebenen Hilfsmittel angefertigt habe. Die aus anderen Quellen direkt oder indirekt übernommenen Daten und Konzepte sind unter Angabe der Quelle gekennzeichnet.

Bei der Auswahl und Auswertung folgenden Materials haben mir die nachstehend aufgeführten Personen in der jeweils beschriebenen Weise unentgeltlich geholfen:

1. Dr. P. Dannberg und Techniker, Fraunhofer Institut Angewandte Optik und Feinmechanik, Jena, bei der Erzeugung mikrooptischer Strukturen nach von mir vorgegebenen Parametern.
2. Dipl.-Ing. Martin Amberg, TU-Ilmenau, bei der Auslegung des Montageplatzes zur Assemblierung und der Charakterisierung eines optischen Interconnects.

Weitere Personen waren an der inhaltlich-materiellen Erstellung der vorliegenden Arbeit nicht beteiligt. Insbesondere habe ich hierfür nicht die entgeltliche Hilfe von Vermittlungs- bzw. Beratungsdiensten (Promotionsberater oder anderer Personen) in Anspruch genommen. Niemand hat von mir unmittelbar oder mittelbar geldwerte Leistungen für Arbeiten erhalten, die im Zusammenhang mit dem Inhalt der vorgelegten Dissertation stehen.

Die Arbeit wurde bisher weder im In- noch im Ausland in gleicher oder ähnlicher Form einer Prüfungsbehörde vorgelegt.

Ich bin darauf hingewiesen worden, dass die Unrichtigkeit der vorstehenden Erklärung als Täuschungsversuch angesehen wird und den erfolglosen Abbruch des Promotionsverfahrens zu Folge hat.

Jena, 22. August 2007

D Thesen

1. Gechirpte Mikrolinsenarrays (cMLAs) erweitern die bisherigen Klassen von Mikrolinsenarrays und bringen zusätzliche Freiheitsgrade für das Optikdesign, die zur Verbesserung der Integrationsmöglichkeiten, der Optimierung der optischen Parameter oder zu neuartigen Effekten führen.
2. Gechirpte Mikrolinsenarrays bestehen aus ähnlichen, jedoch nicht identischen Linsenelementen, deren Eigenschaften mittels parametrischer Beschreibung definiert sind. Die Zelldefinition kann durch analytische Funktionen, numerische Optimierungsverfahren oder eine Kombination aus beiden gewonnen werden. Bei allen gechirpten Arrays hängen die Funktionen von der Position der jeweiligen Zelle im Array ab.
3. Die einfachste Anwendung von cMLAs besteht in der Unterbringung einer Vielzahl verschiedener Linsen auf einem gemeinsamen Träger und der Auswahl der optimal geeigneten Linse zur Erfüllung der gewünschten optischen Funktion, was z.B. für die Kompensation von Herstellungstoleranzen genutzt werden kann. Dies führt zu einer Reduzierung der Herstellungskosten eines optischen Systems bei optimalen optischen Parametern.
4. Durch Nutzung von cMLAs kann die Zahl der Komponenten eines optischen Systems reduziert werden, was mit der Verringerung der Herstellungskosten einhergeht.
5. Weiterhin können cMLAs für die Verbesserung der optischen Parameter gegenüber Systemen basierend auf regulären Mikrolinsenarrays genutzt werden.
6. Die Verwendung eines cMLA aus kanalweise angepassten Zellen erlaubt die Korrektur von außeraxialen Aberrationen und vergrößert das Gesichtsfeld eines künstlichen Aperturobjektives (ultra-flache Kamera) von 25° auf derzeit 64° . Die Nutzung eines cMLA aus individuell angepassten Linsen ermöglicht erstmals, das bekannte Abbildungsprinzip von akademischen Prinzipprototypen zu Systemen mit optischen Parametern zu überführen, die den Einsatzbedingungen industrieller Anwendungen genügen.
7. Die an der ultra-flachen Kamera auftretenden dominanten Aberrationen Astigmatismus und Bildfeldwölbung können für den jeweiligen Einfallswinkel durch Nutzung einer individuell angepassten anamorphotischen Linse korrigiert werden, was durch den kleinen Feldwinkel von etwa 1° pro Kanal ermöglicht wird. Hierfür können elliptische Linsen genutzt werden, die durch ein angepasstes Verfahren basierend auf Reflow von Fotoresist hergestellt werden können. Die Dimensionierung der Linsen und der für die Herstellung erforderlichen Belichtungsmasken kann vollständig durch analytische Funktionen erfolgen.

8. Die an ihren Hauptstrahlwinkel angepassten elliptischen Linsen erzeugen einen beugungsbegrenzten Spot und ermöglichen im Unterschied zu regulären Arrays eine vom Einfallswinkel unabhängige Auflösung der ultra-flachen Kamera.
9. Aberrationskorrigierende cMLAs ermöglichen einen simplen und mithin preiswerten Aufbau eines optischen Interconnects mit hoher Kanalzahl. Um eine hohe Packungsdichte der optischen Kanäle zu erreichen, ist die Herstellung nichtrotationssymmetrischer Linsenprofile erforderlich, was das Reflowverfahren als Herstellungstechnologie ausscheiden lässt. Stattdessen müssen Direktschreibverfahren genutzt werden, mit denen Off-axis-Linsensegmente mit Strukturhöhen bis etwa $30\mu m$ herstellbar sind.
10. Bei Wabenkondensoren auf Basis von cMLAs zur Homogenisierung kohärenter Strahlung können die periodischen Intensitätsmaxima und -minima in der Brennebene der Fourierlinse, die bei regulären Arrays entstehen, vermieden werden. Dies führt zu einer Verbesserung der Homogenität der Intensitätsverteilung.
11. Für Wabenkondensoren auf Basis regulärer MLAs kann eine einfache Bestimmungsgleichung für einen Homogenitätsqualitätsfaktor abgeleitet werden, der nur von der Zahl der beleuchteten Linsen abhängt. Mit steigender Zahl genutzter Linsen verschlechtert sich die Homogenität der Verteilung infolge der Einschnürung der Intensitätsmaxima. Dies ist bei Nutzung von cMLAs nicht der Fall.
12. Herstellungsbedingt resultiert der technologisch sinnvollste Aufbau eines Wabenkondensors mit cMLAs aus der Unterbringung der Arrays auf planen Substraten was letztlich zu einer Keilstruktur führt, die auf Vorder- und Rückseite die Linsenarrays enthält. Es kommt zur Ausprägung eines Intensitätsmaximums (Hot Spot) in der Fernfeldverteilung, dessen Position vom Keilwinkel und dem Substratmaterial abhängt und der die Homogenität der Verteilung reduziert.
13. Für die Keilaufbauten kann ein kritischer Winkel berechnet werden, welcher von der NA der Linsen und dem Keilmaterial abhängt. Für Keilwinkel größer als der kritische Winkel kann die Ausprägung des Hot Spots vermieden und folglich eine verbesserte Homogenität der Intensitätsverteilung erreicht werden.
14. Bei Nutzung nicht-planer Substrate kann die Bildung von Hot Spots vermieden werden, wobei jedoch Reflow von Fotoresist als favorisierte Herstellungstechnologie nicht genutzt werden kann.

E Lebenslauf

Dipl.-Ing. (FH) Frank C. Wippermann

Geburtsdatum: 27.08.1974
Geburtsort: Heilbad Heiligenstadt

Schul- und Hochschulausbildung

09/1989-06/1993 Gymnasium Heiligenstadt
10/1995-11/1999 Studienrichtung Physikalische Technik an der Fachhochschule Jena
04/1998-09/1998 Praktikumssemester an der University of New Mexico, Albuquerque, New Mexico, USA am Department for Physics and Astronomy
04/1999-11/1999 Diplomarbeit bei der Firma piezosystem jena GmbH, Jena
Thema: "Design und Realisierung eines Mehrkanalfaserschalters für die Nachrichtentechnik"
05/2007 Abschluss des Eignungsfeststellungsverfahrens zur Promotion an der TU-Ilmenau, Fakultät für Maschinenbau

Beruflicher Werdegang

12/1999-01/2001 Entwicklungsingenieur für mikrooptische Systeme für die optische Telekommunikationstechnik bei der Firma piezosystem jena GmbH, Jena
Leitung der Arbeitsgruppe Singlemodeschalter
02/2001-07/2001 Gründung der pyramid optics GmbH, Jena
08/2001-10/2003 Entwicklungsingenieur für mikrooptische Systeme
Schwerpunkt hochpräzise Singlemode Faserschalter bei der pyramid optics GmbH, Jena
seit 12/2003 selbstständige Tätigkeit als freiberuflicher Ingenieur
seit 06/2004 wissenschaftlicher Mitarbeiter am Fraunhofer Institut für Angewandte Optik und Feinmechanik, Jena

F Wissenschaftliche Veröffentlichungen

Referierte Journale

1. J.W. Duparré, F.C. Wippermann, P. Dannberg, A. Reimann, "Chirped arrays of refractive ellipsoidal microlenses for aberration correction under oblique incidence," *Optics Express*, Vol. 13, No. 26, pp. 10539-10551, 2005
2. J.W. Duparré, F.C. Wippermann, "Micro-optical artificial compound eyes," *IoP Bioinspiration and Biomimetics* Vol. 1, No. 1, pp. 1-16, 2006
3. F.C. Wippermann, D. Radtke, M. Amberg, S. Sinzinger, "Integrated free-space optical interconnect fabricated in planar optics using chirped microlens arrays," *Optics Express*, Vol. 14, No. 22, pp. 10765-10778, 2006
4. F.C. Wippermann, U.-D. Zeitner, P. Dannberg, A. Bräuer, S. Sinzinger, "Beam homogenizers based on chirped microlens arrays," *Optics Express*, Vol. 15, No. 10, pp. 6218-6231, 2007

Konferenzbeiträge

5. K. Kubitz, F.C. Wippermann, R. Göring, "Aufbau und Dimensionierung faseroptischer Schalter," 14. Internationale Wissenschaftliche Konferenz Mittweida (IWKM), November 2000
6. R. Göring, F.C. Wippermann, K. Kubitz, "Hybrid MOEMS approaches for fiber optic switches and switch matrices," In Proc. of SPIE, MOEMS and Miniaturized Systems, Vol. 4178 pp. 59-66, 2000
7. R. Göring, F.C. Wippermann, K. Kubitz, P. Dannberg, G. Leibelng, A. Bräuer, "Fiber Optic Switches using Transmittive Microoptical Components," In Proc. of VDE World Microtechnologies Congress (MICRO.tec 2000), Vol.1, pp. 115-119, 2000
8. R. Göring, F.C. Wippermann, K. Kubitz, P. Buecker, B. Goetz, "Integration process optimization of a micro-optical 1xN fiber optic switch," In Proc. of SPIE, Optoelectronic Interconnects VII; Photonics Packaging and Integration II, Vol. 3952, pp. 339-345, 2000
9. R. Göring, F.C. Wippermann, K. Kubitz, "Fast piezoelectrically driven optical 2x2 switch," In Proc. of SPIE, Optoelectronic Integrated Circuits and Packaging V, Vol. 4290, pp. 156-162, 2001
10. C. Lausch, R. Göring, F.C. Wippermann, "Fiber optic switch concept with analog micromirror device," In Proc. of SPIE, MOEMS and Miniaturized Systems III, Vol. 4983, pp. 44-52, 2003

11. F.C. Wippermann, K. Kubitz, T. Harzendorf, R. Göring, "Automatisierte Justage und Montage von mikrooptischen Singlemode-Faserschaltern," In Proc. of ITG Treffen Wernigerode 2003, Photonische Aufbau- und Verbindungstechnik, 2003
12. E. Beckert, R. Eberhardt, F.C. Wippermann, "Ebene Keramiksubstrate für den Aufbau hybrid-optischer multifunktionaler Systeme," In Proc. of 5. GMM/ITG/GI-Workshop "Multi-Nature Systems", Dresden, pp. 69-74, 2005
13. F.C. Wippermann, J.W. Duparré, P. Schreiber, P. Dannberg, "Design and fabrication of a chirped array of refractive ellipsoidal micro-lenses for an apposition eye camera objective," In Proc. of SPIE, Optical Systems Design, Vol. 5962, pp. 59622C, 2005
14. J.C. Duparré, A. Bräuer, F.C. Wippermann, "Mikrooptische Systeme für Bildaufnahmeverfahren - Funktionalität und Prototyping," In Proc. of VDE Mikrosystemtechnikkongress 2005, Freiburg, Okt. 2005
15. J.W. Duparré, F.C. Wippermann, P. Dannberg, P. Schreiber, A. Bräuer, R. Völkel, T. Scharf, "Microoptical artificial compound eyes - from design to experimental verification of two different concepts," In Proc. of SPIE, Optical Systems Design, Vol. 5962, pp. 59622A, 2005
16. E. Beckert, F.C. Wippermann, R. Eberhardt, F. Buchmann, "Multifunctional optoelectronic systems on ceramic platforms," In Proc. of Microsystems Technologies 2005, München, 2005
17. F.C. Wippermann, P. Schreiber, A. Bräuer, B. Berge, "Mechanically assisted liquid lens zoom system for mobile phone cameras," In Proc. of SPIE, Optics & Photonics, Novel Optical Systems Design and Optimization IX, Vol. 6289, pp. 628905T, 2006
18. F.C. Wippermann, J.W. Duparré, P. Schreiber, "Application of chirped microlens arrays for aberration compensation and improved system integration," In Proc. of SPIE, Optics & Photonics, Novel Optical Systems Design and Optimization IX, Vol. 6289, pp. 628915, 2006
19. F.C. Wippermann, D. Radtke, U. Zeitner, J. W. Duparré, A. Tünnermann, M. Amberg, S. Sinzinger, C. Reinhardt, A. Ovsianikov, B. N. Chichkov, "Fabrication technologies for chirped refractive microlens arrays," In Proc. of SPIE, Optics & Photonics, Current Developments in Lens Design and Optical Engineering VII, Vol. 6288, pp. 62880O, 2006
20. F.C. Wippermann, J.W. Duparré, P. Dannberg, A. Bräuer, "Improved integration and performance of multi-channel micro optical systems by chirped microlens arrays," EOS Annual Meeting 2006, Micro-Optics, Diffractive Optics and Optical MEMS, 2006

21. F.C. Wippermann, P. Schreiber, A. Bräuer, P. Craen, "Bifocal liquid lens zoom objective for mobile phone applications," In Proc. of SPIE, Electronic Imaging, Sensors, Cameras and Systems for Scientific/Industrial Applications X, Vol. 6501, pp. 650109, Jan. 2007
22. F.C. Wippermann, P. Dannberg, A. Bräuer, S. Sinzinger, "Improved homogenization of fly's eye condenser setups under coherent illumination using chirped microlens arrays," In Proc. of SPIE, Photonics West, MOEMS and Miniaturized Systems VI, Vol. 6466, pp. 64660R, Jan. 2007
23. F.C. Wippermann, U.D. Zeitner, P. Dannberg, S. Sinzinger, "Fly's eye condenser based on chirped microlens arrays," In Proc. of SPIE, Optics & Photonics, Laser beam shaping VIII, Vol. 6663, 2007 (angenommen)

Zeitschriften/Bücher

24. R. Göring, F.C. Wippermann, K. Kubitz, "Schnelle Schalter für die Faseroptik," Mechatronik F&M 12/2000, pp. 47-49, 2000
25. F.C. Wippermann, J.W. Duparré, P. Dannberg, P. Schreiber, A. Bräuer, "Chirped arrays of micro-lenses by reflow of photoresist," Fraunhofer IOF-Jahresbericht 2005
26. E. Beckert, F.C. Wippermann, R. Eberhardt, F. Buchmann, "Optoelektronik für die Analysetechnik," Fraunhofer IOF-Jahresbericht 2005
27. J.W. Duparré, F.C. Wippermann, P. Dannberg, A. Bräuer, "Improving the resolution-homogeneity of ultra-thin vision system based on artificial compound eyes by using chirped arrays of refractive ellipsoidal microlenses," IOF-Jahresbericht 2005
28. F.C. Wippermann, "Gechirpte Mikrolinsenarrays für ultra-dünne Kameras," Photonic 5/2006, AT-Fachverlag GmbH, Stuttgart, 2006
29. J.W. Duparré, F.C. Wippermann, P. Dannberg, A. Bräuer, "Ultra-dünnes Bilderfassungssystem basierend auf künstlichen Facettenaugen," Jahrbuch 2007 Optik und Feinmechanik, Verlag Schiele und Schön, pp. 101-120, 2007
30. F.C. Wippermann, P. Schreiber, "Gechirpte Arrays refraktiver Mikrolinsen," Photonic 4/2007, AT-Fachverlag GmbH, Stuttgart, 2007

Patentanmeldungen

31. F.C. Wippermann, "Optischer Umschalter,"
DE000010116513B4, 2001
32. T. Harzendorf, F. Wippermann, "Optical commutator,"
WO002002082141A3, 2002
33. R. Göring, T. Harzendorf, K. Kubitz, F.C. Wippermann, "Träger- und Gehäuseanordnung für einen faseroptischen Umschalter,"
DE000010229444A1, 2002
34. F.C. Wippermann, "Optischer Umschalter,"
DE102004027219A1, 2004
35. F.C. Wippermann, "Optischer Multimodeschalter,"
DE102004027222A1, 2004
36. F.C. Wippermann, P. Schreiber, A. Bräuer, "Vorrichtung zur Homogenisierung von Strahlung mit nicht regelmässigen Mikrolinsenarrays,"
DE 10 2006 047 941.6, 2006
37. F.C. Wippermann, P. Schreiber, A. Bräuer, "Verfahren und Bilderfassungssystem zur achromatisierten Bildaufnahme von Objekten,"
DE 10 2007 001 010, 2007
38. J.W. Duparré, F.C. Wippermann, A. Bräuer, "Bildsensor mit nicht-äquidistantem Pixelraster zur Verzeichnungskorrektur," 2007